PHASE STABILITY STUDY OF Pt-Cr AND Ru-Cr BINARY ALLOYS

by

MERIAM MALEBO TIBANE

THESIS

Submitted in fulfilment of the requirements for the degree of

DOCTOR OF PHILOSOPHY

in

Physics

in the

FACULTY OF SCIENCES & AGRICULTURE

(School of Physical & Mineral Sciences)

at the

UNIVERSITY OF LIMPOPO

SUPERVISOR: Prof. P.E. Ngoepe

2011

Declaration

I declare that the thesis hereby submitted to the University of Limpopo, for the degree of Doctor of Philosophy in Physics has not previously been submitted by me for a degree at this or any other university; that it is my work in design and in execution, and that all material contained herein has been duly acknowledged.

Tibane, MM (Mrs) Date

Acknowledgements

My special thanks to my supervisor, Professors P.E. Ngoepe for the enthusiasm, inspiration and thoughtful advices which served to give me a sense of direction during my PhD studies. Thanks for bringing me into the world of research where I learnt about the simulation of materials.

My appreciation to Prof. N.M. Harrison and Dr. B.M. Montanari who shared with me a lot of their expertise and research insight. I would also like to thank Dr. Hasani Chauke for his remarks, ideas and a great help concerning latex. I would like to express my gratitude to MMC members for fruitful discussions and inspiration.

I am deeply grateful to the NRF and South African Gas Turbine Research Program for the financial support they gave towards my studies. To the following institutions, University of Limpopo(SA), Ithemba labs(Gauteng SA), UNISA(SA), Daresbury Laboratory (UK) and Rutherford Appleton Laboratory (UK) thank you for giving me an access to use your facilities, I really appreciate your help.

Special thanks to two dynamic families, Tibane and Mokagane, I am so grateful for giving me a loving environment to develop. To my mom Leah Mokagane thank you very much for your love, care and advices. My husband and kids thank you for the incredible amount of support and patience you had with me.

Above all, I would like to thank God, my major source of strength when I worked on my thesis.

Dedication

This thesis is fully dedicated to my two beloved daughters, **Ncobile** and **Zolile**, my husband **Simanga**, my mother **Ngwanamashita Leah Mokagane**, my late father Amos Mokagane and two brothers **Martin** and **Tshepo**.

Contents

List of Figures

List of Tables

Abstract

Planewave pseudopotential calculations were conducted to predict the energetics and phase stability of Pt-Cr and Ru-Cr binary alloys. Validation of appropriate number of k-points and planewave energy cut-off was carried out for all studied systems. At the composition of A_3B and AB_3 (where A = Cr and B = Pt or Ru) phases, the heats of formation determined for five different structures, $L1_2$, A15, tP16, DO_C and DO'_C are almost of the same magnitude and the relaxed structures show no rotation. We observed that the cubic $L1_2$ Pt_3Cr is the most stable structure in agreement with the experiments. The results for $PtCr_3$ indicate the negative heat of formation for the A15 phase whereas all the remaining studied phases have positive heats of formation. It is clear that the $PtCr_3$ (A15) is the most stable structure. PtCr ($L1_0$) was found to be more stable compared with PtCr (B2) phase. The $L1_2$ Pt_3Cr, A15 $PtCr_3$ and $L1_0$ PtCr phases could be considered as possible coatings to cover the engines which are exposed to aggresive environments. The heats of formation of all studied compositions and phases of Ru-Cr systems are positive, these results suggest that, generally, studied Ru-Cr phases are not stable. The effect of pressure and doping were investigated on A15 $RuCr_3$ structure which was reported to exist at a higher temperature. Elastic constants and moduli were investigated to determine the strength of the PtCr systems. The strength of PtCr $L1_0$ is greater than that of B2 phase. The ratio of shear to bulk modulus (G/B) has been used to predict the ductility or the brittleness of the material. It was found that Pt_3Cr $L1_2$ is the most ductile phase among those considered in this study. The density

of states were calculated to further analyze the stability of systems.

The magnetic properties of Cr were studied using VASP which predicted an anti-ferromagnetic and a non-magnetic ground state for pure Cr. We have investigated the thermal stability at 0 GPa for different phases of Pt_3Cr, $PtCr_3$, PtCr and $RuCr_3$ A15 phase, where we detected the soft modes at X, G, M and R points of the Brillouin zone from the phonon spectra of Pt_3Cr A15 phase. Pt_3Cr $L1_2$ and $PtCr_3$ A15 are predicted as dynamically stable structures. $RuCr_3$ A15 phase was found to be dynamically stable but thermodynamically unstable. Phonon DOS were studied to observe the modes of vibration and atoms that contribute to soft modes. Lastly we investigated the thermal expansion of Pt_3Cr $L1_2$ and A15 phases.

Chapter 1

Introduction

In this chapter we give a brief overview of the previous theoretical and experimental work done on the metallic Pt, Cr, Ru and their binary alloys. The importance and the use of the Pt-Cr and Ru-Cr alloys will be briefly summarized, lastly we state the objectives of the study.

1.1 Overview

Transition metal alloys serve as a good basis for development of modern solid-state theory and have a variety of potential applications in technology. Materials that are solid at high temperatures are in demand for high-temperature structural applications, whereas those having high values of strength-to-weight and stiffness-to-weight are desired for aircraft and space applications. Improving the efficiency of gas turbine and prolonging the service life of turbine hot-section components are constant driving forces for the development of high temperature materials in engine industries. The gas turbine engines are used in today's means of transport, i.e trains, ships, air-

crafts etc. These engines are exposed to environments such as hot corrosion[1] and oxidation that can decreace the engine's operation time. With today's jet engine operating temperatures, thermal barrier coating failure results in melting of the blade. But even without reaching such catastrophic failure, blades suffer from accelerated oxidation depending on the environment and hot corrosion. Coatings can considerably enhance the oxidation and hot corrosion resistance of these components.

We study Pt based superalloys since their higher melting point and good corrosion resistance have the potential to substitute Ni-based superalloys for high temperature components in turbine engines. The platinum family (platinum, palladium, ruthenium, iridium, osmium and rhodium) is one of the most important group of metals. These materials and their alloys display exceptional qualities as they have high corrosion resistance, high resistance to arc erosion and a high melting point. The alloys of this family are very hard, and consequently they have a good mechanical wear ability. When used in proper applications, the platinum metals provide years of successful operation.

In search for the new materials to be used as components in gas turbine engines, considerable interest has been shown in chromium(Cr) and Cr-rich alloys since the late 1950s as Cr has a high melting temperature (1863 °C) and a good oxidation resistance. Its low density (20 % less than that of most Ni-base alloys) and high thermal conductivity (two or four times higher than that of most Ni-base superalloys) are also attractive since they may result in increased efficiency[2, 3, 4]. The presence of a significant amount of Cr

gives the Pt and Ru coatings excellent corrosion resistance combined with good oxidation resistance. Ruthenium is a hard, silvery white metal with a shiny surface and a melting point of 2300 - 2450 °C, a boiling point of about 3900 - 4150 °C, and a density of 12.41 g/cm^3. It is a relatively inert element that does not react with oxygen, most acids or aqua regia (mixture of concentrated nitric acid and 3-4 parts of hydrochloric acid).

Platinum-group metals (PGMs) such as platinum, palladium, rhodium, ruthenium, osmium, and iridium have many outstanding properties. They are widely used in the automotive industry as catalysts. They have very high melting points, for example, Pt, Rh, and Ir melt at 1769, 1966, and 2247 ^{o}C, respectively. Their alloys are thus widely used as crucibles for growing single crystals especially oxides. Platinum is used in industries owing to its wear resistance and as jewellery due to its lack of tarnish. It is used as a coating to chemical attack and as a resistor due to its excellent high-temperature resistance. [5, 6, 7]

1.2 Binary alloys

PtCr and RuCr are additional binaries that have been prioritised in the current study and associated compositions such as $PtCr_3$, Pt_3Cr (A15, $L1_2$, tP16, DO_c and DO'_c), PtCr (B2 and $L1_0$), RuCr (B2 and $L1_0$) and $RuCr_3$, Ru_3Cr(A15, $L1_2$, tP16, DO_c and DO'_c) have been targetted. These binaries were also studied experimentally by Mintek and indeed related equilibrium phase diagrams and solid phases are being determined. Information on studies of Pt-Cr and Ru-Cr binary and ternary alloys is scarce in literature when

compared to Ni-Al and Pt-Al binaries.

1.2.1 PtCr Alloys

Much research has been done on Pt_3Cr ordered alloy with Cu_3Au-type structure. The ground state magnetic properties [8] of Pt_3Cr have been explained from the calculated electronic structure using tight-binding parametrisation scheme. The global trends of the experimental values such as the local magnetic moments have been reproduced satisfactorily by spin-polarized band calculations and the ferrimagnetism in Pt_3Cr has been explained in terms of the hybridisation between 3d states in Cr band and 5d states in Pt band.

Several studies have been done on Pt_3Cr [9, 10] since the A_3B-type intermetallic compounds have attracted considerable interest owing to their diverse mechanical, structural and magnetic properties. Extensive work has been done on Pt-Cr alloys [11] to understand the crystal structure and mechanism of the ordered phase. Jackson et.al [11] performed tensile (using small-scale tensile testing materials) and hardness tests to measure mechanical properties after various heat treatments. The results for tensile tests indicated an increase in tensile strength with no effect on ductility. The electrical sensitivity of several Pt-Cr alloys containing between 5 and 15 at.%Cr has been measured over the temperature range of 1.4 - 300 K [12]

1.2.2 RuCr Alloys

No thermodynamic measurements of RuCr were reported up to 1987 [13]. An enthalpy of formation of Cr_2Ru was calculated using Mediema's model, and a

value of -15 kJ/mol was obtained. Addition of Ru increases the Neel temperature of pure Cr from 311.5 K to a maximum of $\approx 550K$ at $\approx 5at.\%Ru$. A further increase in Ru content to $\approx 15at\%$ lowers the temperature at $\approx 273K$ [14]. Weak ferromagnetism was observed in the regions of 30 and 60 at.%Ru.

1.3 Overview of the Pt,Cr, Ru and their binary alloys

This section gives an overview of the Pt-Cr and Ru-Cr phase diagrams, and lastly the structural aspects of all studied phases of the metallic Pt, Cr and Ru and their binary alloys.

1.4 The Pt-Cr phase diagram

PtCr system was reviewed [15] and their assessed phase diagram [16] in Figure 1.1 is based primarily on extensive experimental study using microscopic, XRD and electron micropobe technique [17, 18]. The phase diagram is dominated by broad homogeneity range of the (Pt) terminal solid solution from 29 to 100at.%. The composition and temperature of the eutectic have been determined by Waterstrat [18].

Recently a calculated phase diagram Fig 1.2 was carried out [19]. The presence of a eutectic reaction on either side of $PtCr_3$ was established [20, 21]. $PtCr_3$ remains cubic over its whole composition range from 50-85 at.% Pt[18, 20, 21, 22, 23, 24, 25]. $L1_2$ Pt_3Cr orders to an $L1_0$ type at composition PtCr, without the tetragonal distortion typical of this structure [18, 23, 24, 25]. Through thin film studies, a tiny distortion was however, shown [26, 27, 28]

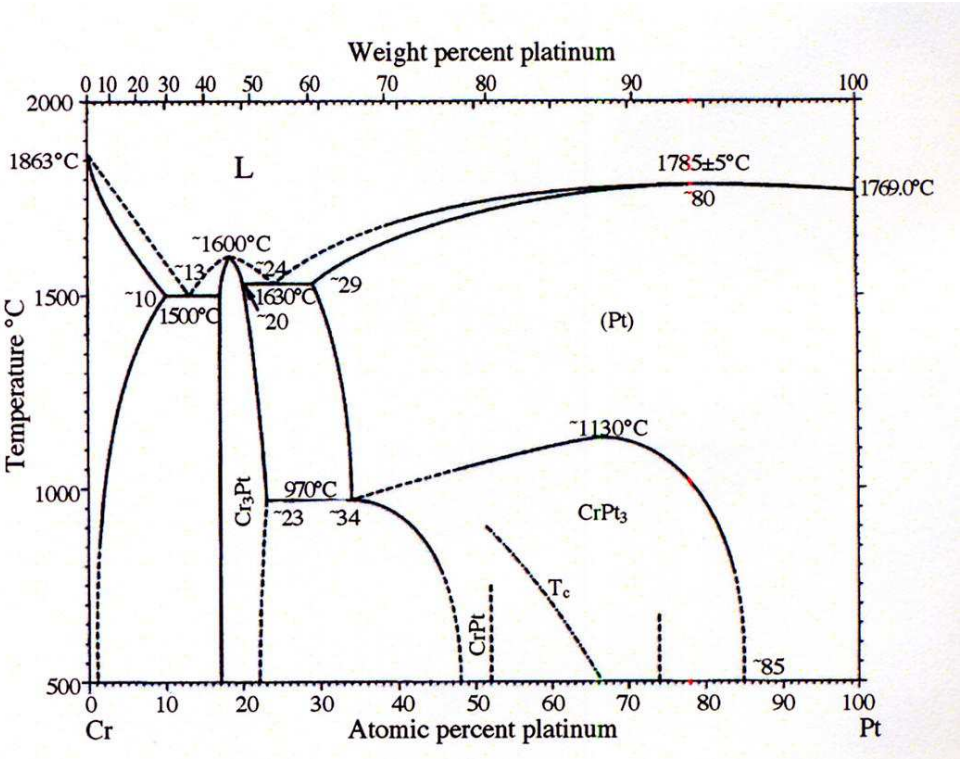

Figure 1.1: Phase diagram of Pt-Cr by Massalski[16]

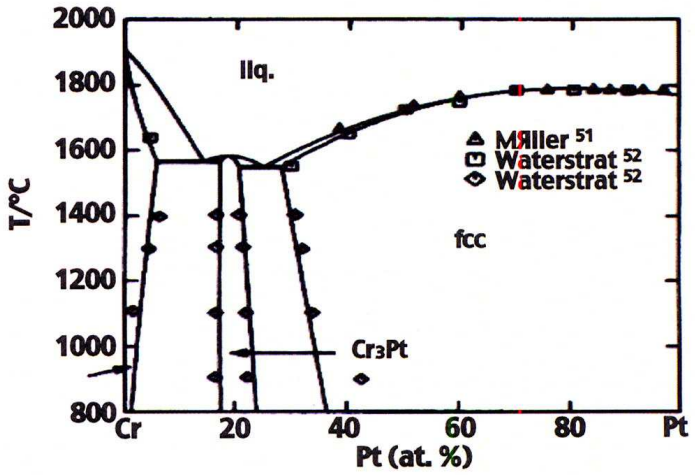

Figure 1.2: Phase diagram of Pt-Cr by Oikawa[19]

as well as a PtCr/Pt_3Cr two-phase region. Using Miedema's model [13], an enthalpy of formation with a value of $\delta H = -36kJ/mol$ (of atoms) was calculated for PtCr.

Small additions of Pt increase the Neel temperature of pure Cr from 311.5 to 440K (at 0.6 at.% Pt) [29], 583K at 2at.% Pt [30], and 460K at 5at.% Pt [31]. Disordered(Pt) is paramagnetic, while Pt_3Cr shows strong spontaneous magnetisation [25]. Pt_3Cr is ferromagnetic [23], with some maximum magnetisation near stoichiometric composition [25], which then decrease with increasing Cr until it changes to antiferromagnetic behaviour at $\approx$ 52at.% Pt [21, 30] to that of the PtCr phase which show no Neel point [24]. The addition of Cr strongly increases the electrical resistivity of Pt [17, 21, 32, 33].

1.5 The phase diagram of Ru-Cr

The commonly accepted binary phase diagram for the Ru-Cr system is shown in Figure 1.3. According to this diagram, the terminal Cr solid solution has a maximum solid solubility of 18.0 % Ru at room temperature and about 26 % Ru at 1600 K. At room temperature, two or multiphase structures exist for alloys with Ru concentrations from 18 to about 59 %. Several researchers proposed different versions of the binary phase diagram for the Ru-Cr system. Savitskii et al. first presented the phase diagram of Ru-Cr, which indicated a eutectic reaction in the composition region between 0 to 24 % Ru [34]. However, a significantly different version was given by Shunk [35] and was confirmed with small changes by Waterstrant in 1981 [36].

The Massalski phase diagram [38] is based on the review of the work on microstructural evolution and mechanical properties of Ru-Cr alloys and is similar to that proposed by Shunk [35]. According to this phase diagram, terminal Cr has a maximum solubility of about 18.0 % Ru at room temperature and about 26 % Ru at 1600 K. However Gu et al work [37] indicated that the alloys containing 6 to 20 % Ru precipitated the $RuCr_3$ phase during heat treatment.

There are two possible explanations for the formation of $RuCr_3$ in this composition region. The first involves inhomogeneity caused during solidification and heat treatment. Since the ingots were remelted at least five times and the microstructure was homogeneous for all tested specimens according to their investigation, this reason is possible but not probable. The second possible explanation is that the solid solution data presented in Figure 2.3

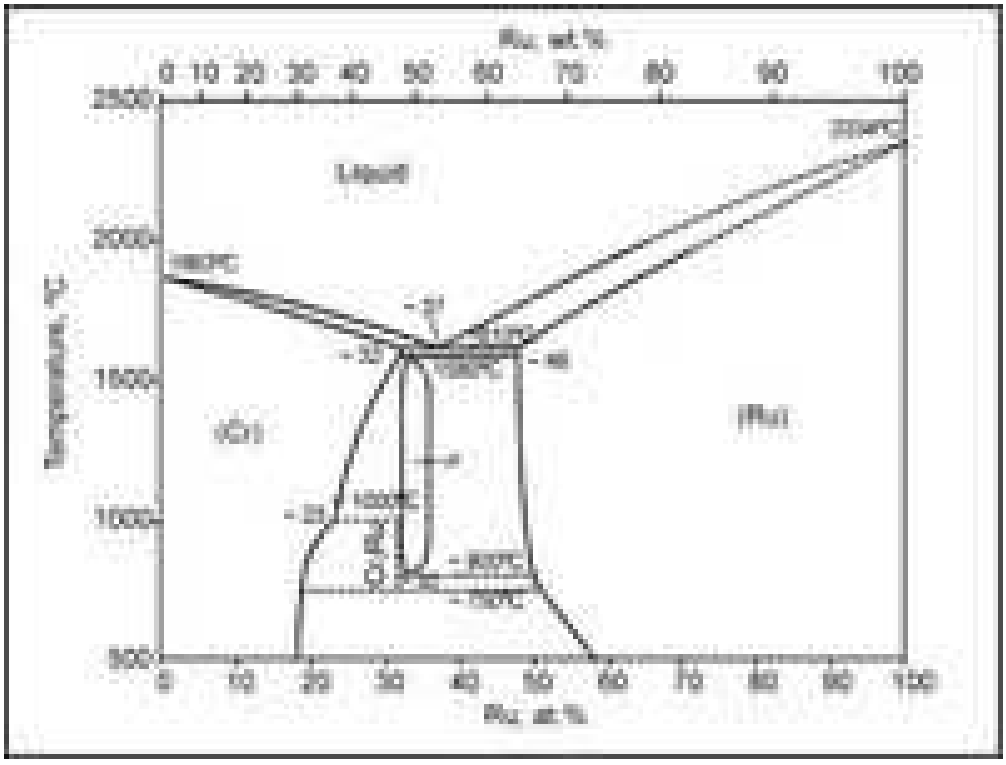

Figure 1.3: phase diagram of Ru-Cr [38]

[38] are in error. Since the precipitates first formed at the grain boundaries and their volume fraction increased with increasing Ru content, Gu et al [37] suggest that there is a eutectic reaction between α chromium and $RuCr_3$ and Ru concentrations ranging from about 3 to approximately 20%.

1.6 Structural aspects of Pt, Cr, Ru and their binary alloys

There are 14 different types of crystal cell structures or lattices that are found in nature. However most metals and many other solids have unit cell

structures described as bcc, fcc or hcp. A key feature that distinguishes metals from non-metals is their bonding; they have electrons that are free to move easily from one atom to the next.

1.6.1 fcc Pt

The fcc structure atoms are located at each of the corners and the centers of all cubic faces. Each of the corner atoms is the corner of another cube so the corner atoms are shared among eight unit cells. Additionally, each of its six face centered atoms is shared with an adjacent atom. Since 12 of its atoms are shared, it is said to have a coordination number of 12. The fcc unit cell consists of a net total of four atoms; eight eigths from corners atoms and six halves of the face atoms.

The atoms in the fcc can pack closer together than they can in the bcc structure. The atoms from one layer nest themselves in the empty space between the atoms of the adjacent layer. Pt is a face centered cubic structure with a space group symmetry Fm-3m and pearson symbol cF4. The experimental lattice parameter of Pt at room temperature is 3.924 Å [39]. The atoms are located at (0 0 0) and the melting point is 1769^0C.

1.6.2 bcc Cr

The bcc unit cell has atoms at each of the eight corners of a cube plus one atom in the center of the cube. Each of the corner atoms is the corner of another cube so the corner atoms are shared among eight unit cells. It is said to have a coordination number of 8. The bcc unit cell consists of a net

total of two atoms; one in the center and eight eights from corners atoms. The bcc arrangement does not allow the atoms to pack together as closely as the fcc or hcp arrangements. The bcc is often the high temperature form of metals that are close-packed at lower temperatures.

The bcc unit cell ha s a packing factor of 0.68. Metals which have a bcc structure are usually harder and less malleable than close-packed metals such as gold. When the metal is deformed, the planes of atoms must slip over each other, and this is more difficult in the bcc structure. It should be noted that there are other important mechanisms for hardening materials, such as introducing impurities or defects which makes slipping more difficult. Cr has a body-centered structure with a space group Pm-3m and pearson symbol cP2, the experimental lattice parameter of Cr is 2.884 . The structure contains two Cr atoms per unit cell located at (0 0 0) and (0.5 0.5 0.5). The melting point of Cr is 1863^0C.

1.6.3 hcp Ru

Another common closed packed structure is the hexagonal close packing. The hexagonal structure of alternating layers is shifted so its atoms are aligned to the gaps of the preceding layer. The atoms from one layer nest themselves in the empty space between the atoms of the adjacent layer just like in the fcc structure. However, instead of being a cubic structure, the pattern is hexagonal. The hcp structure has three layers of atoms. In each, the top and bottom layer, there are six atoms that arrange themselves in the shape of a hexagon and a seventh atom that sits in the middle of the hexagon. The

middle layer has three atoms nestled in the triangular "grooves" of the top and bottom plane.

There are six of these "grooves" surrounding each atom in the hexagonal plane, but only three of them can be filled by atoms. There are six atoms in the hcp unit cell. Each of the 12 atoms in the corners of the top and bottom layers contribute 1/6 atom to the unit cell. The two atoms in the center of the hexagon of both the top and bottom layers each contribute 1/2 atom and each of the three atoms in the middle layer contribute 1 atom. The coordination number of the atoms in this structure is 12. There are six nearest neighbours in the same closed packed layer, three in the layer above and three in the layer below. Ru exhibits the hexagonal closed packed structure with experimental lattice parameter of 2.73 Å. The melting point of Ru is between 2.300^{o}C and 2.450^{o}C.

The hcp and the fcc structures both have a packing of 0.74, consist of closely packed planes of atoms, and have a coordination number of 12. The difference between the fcc and hcp is the stacking sequence. The hcp layers cycle among the two equivalent shifted positions whereas the fcc layers cycle between three positions. The HCP contains only two types of planes with an alternating ABAB arrangement. Atoms of the third plane are in exactly the same position as the atoms in the first plane. However, the fcc structure contains three types of planes with ABCABC arrangement. Atoms in rows A and C are no longer aligned. Cubic lattice structures allow slippage to occur more easily than non-cubic lattices, so hcp are not as ductile as the fcc metals.

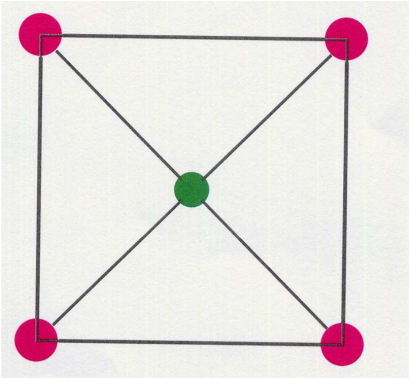

Figure 1.4: PtCr B2 structure, atoms are represented by balls of different colors: pink (Pt) and green (Cr)

1.6.4 B2 PtCr and RuCr

PtCr and RuCr have a CsCl structure as shown in Figure 1.4: the B2 PtCr structure. The unit cell has two atoms of different species i.e Pt and Cr which are located at Cr (0 0 0) and Pt (0.5 0.5 0.5).

1.6.5 $L1_2$ AB_3 and A_3B

Pt_3Cr alloy is known to have the crystal structure of $Cu_3Au(L1_2)$ type with a space group Pm-3m and pearson symbol cP4. Cu_3Au is an ordered alloy that possesses well-understood surface properties for which experimental determination of the band structure has been extensively compared with theoretical calculations. This structure has cubic symmetry, which suggests that the alloys have no uniaxial magneto-crystalline anisotropy. The structure consists of four atoms per unit cell (3Pt, Cr), with Cr and Pt atoms located at 1a(0 0 0) and 3c(0 0.5 0.5) respectively as shown in Table 1.1. The optimized structures of Pt_3Cr $L1_2$ and $PtCr_3$ $L1_2$ are shown in Figures 1.5 and 1.6

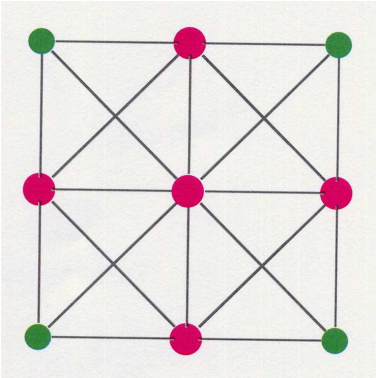

Figure 1.5: Pt_3Cr $L1_2$ structure

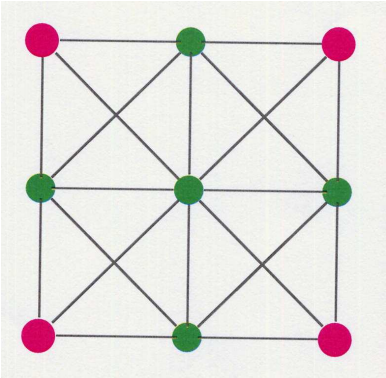

Figure 1.6: $PtCr_3$ $L1_2$ structure

Table 1.1: The atomic positions (Wyckoff notation) in the $L1_2$ Pt_3Cr crystal structure.

Atoms	Positions	x	y	z
Cr	1a	0.0	0.0	0.0
Pt	3c	0.0	0.5	0.5

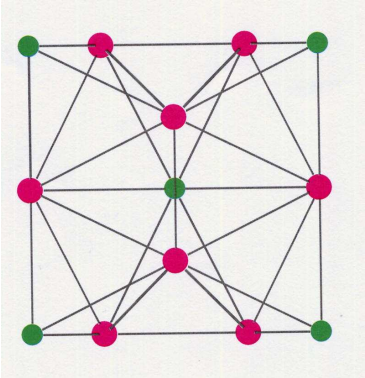

Figure 1.7: Pt_3Cr A15 structure

1.6.6 A15

The A15 compounds crystallize in a structure in which the unit cell has the overall shape of a cube as shown in Figure(s) 1.7 and 1.8 the A15 unit cell of Pt_3Cr and $PtCr_3$ respectively. In Pt_3Cr , the Cr atoms are located at the corners and in the center of the cube, while the Pt atoms are arranged in pairs on the cube faces. A special charectaristic of the A15 crystal structure is that the Pt atoms form mutually orthogonal linear chains that run throughout the crystal lattice.

1.6.7 DO_C

Pt_3Cr takes the tetragonal DO_C structure, which is shown in Figure 1.9. The prototype is U_3Si. The lattice constants are a = 5.225 Å and c = 7.418 Å. The DO_C structure has the same Pearson notation as $DO_C^{'}$, the difference being in the position of the Cr atoms. In DO_C the Cr atom occupies the 4a site, while in the $DO_C^{'}$ the Cr atom is on the 4b site, as shown in Table 1.2 and Figure 1.10.

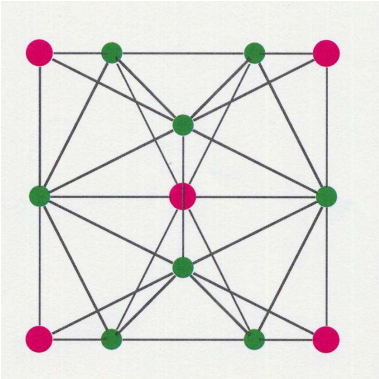

Figure 1.8: $PtCr_3$ A15 structure

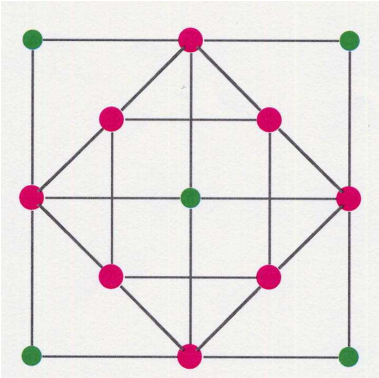

Figure 1.9: Pt_3Cr DO_c Structure

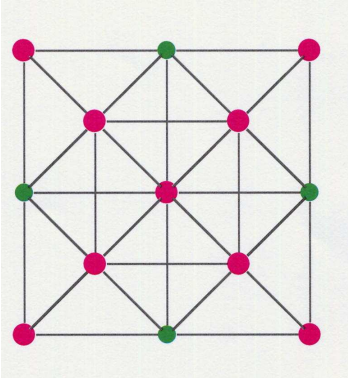

Figure 1.10: Pt_3Cr DO'_c Structure

Table 1.2: The atomic positions (Wyckoff notation) in the DO_C and $DO_C^{'}$ Pt_3Cr crystal structure. The displacement parameter,u is different for DO_C and $DO_C^{'}$ structures.

Atom in DO_C	Atom in $DO_C^{'}$	Positions	x	y	z
Cr	Pt1	4a	0.00	0.00	0.25
Pt1	Cr	4b	0.00	0.50	0.25
Pt2	Pt2	8h	0.25-u	0.75-u	0.00

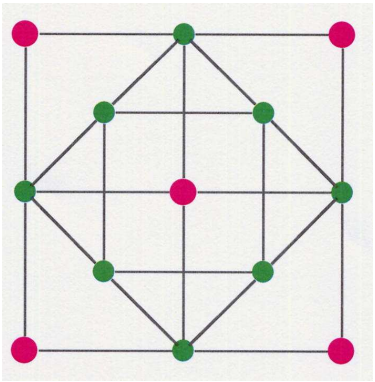

Figure 1.11: $PtCr_3$ DO_c Structure

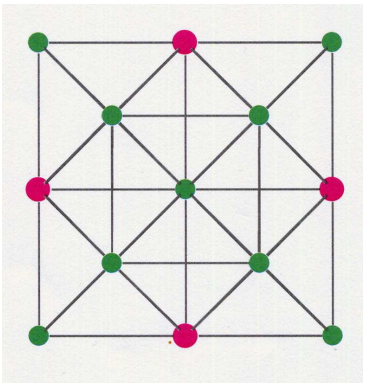

Figure 1.12: $PtCr_3$ $DO_c^{'}$ Structure

Table 1.3: The atomic positions (Wyckoff notation) in the $GaPt_3$ type of the space group P4/mbm (pearson symbol tP16), Pt_3Cr crystal structure.

Atom	Positions	x	y	z
Cr	4f	0.000	0.500	0.258
Pt1	4e	0.000	0.000	0.251
Pt2	4g	0.231	0.731	0.000
Pt3	4h	0.290	0.790	0.500

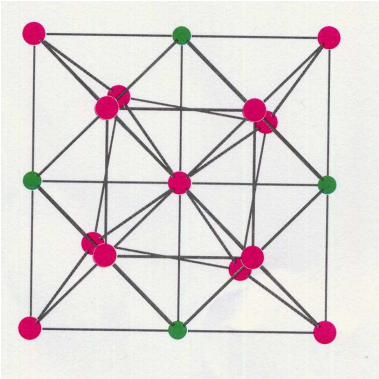

Figure 1.13: Pt_3Cr tP16 Structure

1.6.8 tP16 Pt_3Cr

We will also consider the tetragonal tP16 (Pt_3Ga) structure, which is displayed at low temperatures by the Pt-Ga system. The unit cell is shown in Figure 1.12, where we note 16 atoms per unit cell (4Cr and 12Pt) with Cr on 4f(0, 0.5, 0.258), Pt on 4e(0,0,0.251), Pt on 4g(0.231,0.731,0) and Pt on 4h(0.29,0.29,0.5) sites, as given in table 1.3. The experimental lattice constants are a = 5.459 Å and c = 7.806 Å .

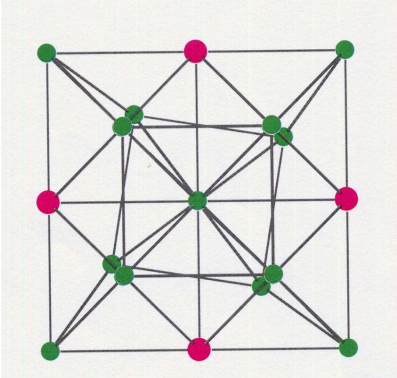

Figure 1.14: $PtCr_3$ tP16 Structure

1.7 Mintek project

At mintek work has been ongoing in building a thermodynamic database for the prediction of the phase equilibria in Pt-based superalloys [40, 41, 42, 43, 44]. This work is based on Pt, Cr, Ru and Al. Pt-Cr-Ru has been studied experimentally in the as-cast condition using scanning electron microscope (SEM) and X-ray diffraction (XRD). The major phases were Ru, Pt and PtCr while the minor phases were Cr_2Ru (σ), Cr_3Ru (A15) and $PtCr_3$ (A15).

In this work we study five phases of $PtCr_3$ (A15 phase included), Pt_3Cr, Ru_3Cr and $RuCr_3$. Again we will look at two phases (B2 and $L1_0$) of Pt-Cr and Ru-Cr, and lastly the Pt,Cr and Ru phases.

1.8 Objectives

In this thesis we investigate the stability of Pt-Cr and Ru-Cr binary alloys. This study focuses on the gas turbine engines that are operating at higher temperature which expose the engine to environments such as oxidation and

hot corrosion that can decrease the operation time. The main objective of the thesis is to search for the potentially useful and undiscovered Pt-Cr and Ru-Cr binary alloys aiming at prolonging the service life of the turbine hot section components, which could ensure the global competitiveness of South Africa.To meet the thesis objectives, we investigate stability of five phases ($L1_2$, A15, tP16, DO_C and DO'_C) of the Pt_3Cr, $PtCr_3$, Ru_3Cr and $RuCr_3$ compositions. In addition we will also perform stability study on two phases ($L1_0$ and B2) of the additional binaries, PtCr and RuCr. We are interested in Pt, Cr and Ru because they display exceptional qualities like high melting point and high corrosion resistance. The alloys formed by these high melting point materials are very hard and they have a good mechanical wear ability. The stability will be predicted based on the heats of formation, elastic constants, density of states, phonon spectra and phonon density of states for Pt-Cr and Ru-Cr binary alloys. We will investigate the magnetic state of metallic Cr, furthermore, we study the effect of doping with Ni in particular the A15 $RuCr_3$ existence at a higher temperature has been reported. The thermal expansion of Pt_3Cr $L1_2$ and A15 phases will be studied in the temperature range of 0 -500 K. After analyzing all the stability results, we will then consider the agreement between different methods of study, and draw a final conclusion about the phase stability of Pt-Cr and Ru-Cr binary alloys.

1.9 Outline

The thesis is partitioned into seven chapters:

In Chapter 1 we give a brief overview of Pt-Cr and Ru-Cr binary alloys. We further outline the background of the previous work and the objectives of the thesis. This chapter review the phase diagram of Pt-Cr and Ru-Cr binary alloys, and describes the structures of the pure metals and different phases of Pt-Cr and Ru-Cr alloys.

Chapter 2 introduces and explains the methods used in the present study, in particular the plane-wave pseudopotential method, as embodied in the CASTEP and VASP codes.

Chapter 3 gives the results and discussions of the structural properties of Pt, Cr, Ru and their binary alloys. This chapter predicts the stability of Pt-Cr and Ru-Cr based on the heats of formation of different phases. The magnetic moments are computed. We investigate the effects of pressure and doping on the heats of formation of A15 $RuCr_3$ structure. The computed results are compared with previous theoretical studies and experimental work. We will study the elastic constants and moduli that will be used to determine the strength of materials

In Chapter 4 we describe and analyze the calculated DOS which give valuable information on the nature and stability of the alloys. This chapter also compares the energy differences between the main peaks of the valence band and conduction band of different materials. We will study the magnetic properties of Cr

Chapter 5 predicts the thermal stability of Pt-Cr and Ru-Cr systems from phonon calculations, and determines the thermal expansion. Chapter 6 presents the conclusions of this thesis and recommendations for future work. This is followed by bibliography.

Chapter 2

Methodology

In this chapter we outline the ab-initio quantum mechanical methods used in this study. The project is based on density functional theory (DFT) which is a formal exact theory that connects the ground state properties to the charge density. Both CASTEP [45] (Cambridge Sequential Total Energy Package) and VASP [46] (Vienna *abinitio* Simulation Package) computational schemes have been employed. CASTEP and VASP employs the plane-wave pseudopotential methods which performs the ab-initio quantum mechanical calculations that explore the properties of crystals and surfaces in materials such as metals, minerals semiconductor, ceramics and zeolites. CASTEP with the ultrasoft pseudopotential(USPP) method [47]and VASP with USPP and projector augmented wave(PAW) [48] methods. We will start by discussing DFT theory which predicts the ground state energy and the phase stability in crystals.

2.1 Density functional theory

Density functional theory is an extremely successful approach for the description of the ground state properties of metals, semiconductor and insulators. Density-functional theory is based on the remarkable theorem by Hohenberg and Kohn [49] who demonstrated that the total energy of a many-electron system in an external potential is a unique functional of the electron density for a given position of atom nuclei. The minimum value of the total energy functional is the ground state energy of the system, and the density that yields this minimum value is the exact ground state density. The electron density is a scalar function defined at each point r in real space, $\rho = \rho(r)$.

In density functional theory, the total energy is expressed as

$$E = E\left[\rho(\mathbf{r}), R_\alpha\right] \tag{2.1}$$

where the electron density ρ and total energy E depend on the type and arrangement of the atomic nuclei, $\mathbf{R}_\alpha$ denotes the positions of the nuclei α in the system. This equation is the key to the atomic-scale understanding of structural, electronic and magnetic properties of matter. While the Hohenberg-Kohn theorem shows it is possible to use the ground state density to calculate properties of the system, it does not provide a way of finding the ground state. A route to this is provided by Kohn-Sham equations [50]. The idea of the Kohn-Sham approach is to reintroduce a special type of wavefunctions (single particle orbitals) into the formalism, to treat kinetic and interaction energy. In this approach the total energy in equation 2.1

is decomposed into three terms Schrödinger equation by first expressing the functional as the sum of three terms, written as

$$E\left[\rho\right] = T_o\left[\rho\right] + U\left[\rho\right] + E_{XC}\left[\rho\right] \tag{2.2}$$

where T_o is the sum of the kinetic energies of all effective electrons moving as independent particles. In DFT the "real" electrons of a system are replaced by "effective electrons" with the same charge, mass and density distribution. However, effective electrons move as independent particles in an effective potential, whereas the motion of a real electron is correlated with those of all electrons. If each effective electron is described by a single particle wave function ψ_i, then the kinetic energy of all effective electrons in the system is given by

$$T_0 = \sum n_i \int \psi_i^*(r) \left[-\frac{\hbar^2}{2m}\nabla^2\right] \psi_i(\mathbf{r})dr \tag{2.3}$$

Where n_i denotes the number of electrons in state i. The second term, U, is the Coulomb energy which is purely classical and contains the electrostatic energy arising from the Coulombic attraction between the electrons and nuclei, the classical repulsion between the electrons, and the repulsion between the nuclei. It can be written as

$$U\left[\rho\right] = U_{en}\left[\rho\right] + U_{ee}\left[\rho\right] + U_{ion-ion}. \tag{2.4}$$

The third term in equation 3.2, E_{XC}, is the exchange correlation energy, which accounts for all remaining compicated electronic contributions to the

total energy. Electrons are fermions that obey Pauli exlusion principle. In real space, the Pauli principle implies that, around each electron with a given spin, all other electrons with the same spin tend to avoid that electron. As a consequence, the average Coulombic repulsion energy of that electron is reduced. This energy gain is called exchange energy. Correlation energy is the additional many-body interaction between electrons of both spins.

The set of wave functions that minimize the Kohn-Sham energy functional is given by the self-consistent solutions of the equation:

$$\left[-\frac{\hbar^2}{2m}\nabla^2 + V_{ion}(\mathbf{r}) + V_H(\mathbf{r}) + V_{XC}(\mathbf{r})\right]\psi_i(\mathbf{r}) = \varepsilon_i\psi_i(\mathbf{r}), \tag{2.5}$$

where ψ_i is the wave function of electronic state i, ε_i is the Kohn-Sham eigenvalue, V_{ion} is the static total electron-ion potential and V_H is the Hartree potential of the electron which is given by

$$V_H(\mathbf{r}) = e^2 \int \frac{\rho(\mathbf{r}')}{|r - r'|} d\mathbf{r}'. \tag{2.6}$$

The exchange-correlation potential, V_{XC}, is given formally by the functional derivative

$$V_{XC}(\mathbf{r}) = \frac{\delta E_{XC}\left[\rho(\mathbf{r})\right]}{\delta\rho(\mathbf{r})}. \tag{2.7}$$

ε_i are Lagrange multipliers, which are effective one-electron eigenvalues. These eigenvalues are used to determine the occupation number n_i by applying the Aufbau principle. The eigenstates are ordered according to increasing eigenvalues. For non-spin polarized systems, each state is occupied by at most two electrons with opposite spins. $\rho(\mathbf{r})$, the electron density, is given by

$$\rho(\mathbf{r}) = 2\sum_i \int |\psi_i(\mathbf{r})|^2. \tag{2.8}$$

Therefore, the Kohn-Sham total-energy functional is written as:

$$E = 2\sum_{occ} \varepsilon_i + U_{ion-ion} - \frac{e^2}{2}\int\int \frac{\rho(\mathbf{r})\rho(\mathbf{r}')}{|\mathbf{r}-\mathbf{r}'|} d\mathbf{r}d\mathbf{r}' + E_{XC}[\rho(\mathbf{r}])) - \int \rho(\mathbf{r})V_{XC}d\mathbf{r}. \tag{2.9}$$

From the above discussion, the exchange-correlation potential can not be obtained explicitly because the exact exchange-correlation energy is not known. The only way to solve the problem is by way of approximate methods, the local density approximation which will be discussed in the next section.

2.1.1 Local Density Approximation

The simplest method of describing the exchange correlation energy of an electronic system is to use the local density approach, which is widely used in total-energy pseudopotential calculations. LDA gives the correct sum rule for the exchange co rrelation hole [51, 52, 53]. In the LDA it is assumed that the exchange-correlation energy depends only on the local electron density around each volume element dr and thus,

$$E_{XC}\left[\rho(\mathbf{r})\right] \approx \int \rho(\mathbf{r})\varepsilon_{XC}\left[\rho(\mathbf{r})\right] d\mathbf{r} \tag{2.10}$$

The basic idea in the LDA is that any atomic arrangement such as crystal, a surface or a molecule there is a certain electron density $\rho(r)$ at each point r in space. There are two assumptions made in LDA

(i) The exchange and correlation effects come predominantly form the intermediate vicinity at a point r and

(ii) these exchange and correlation effects do not depend strongly on the variations of the electron density in the vicinity of r.

If conditions (i) and (ii) are reasonably well fulfilled, then the contribution from volume element dr would be the same as if this volume elements were surrounded by a constant electron density of the same value as within dr. This is an excellent aprroximation for metallic systems, but represents quite a severe simplification in systems with strongly varying electron density.

A system of interacting electrons with a constant density is called a homogenous electron gas. Substantial theoretical efforts have been made to understand and characterize such an ideal system. In particular, the exchange-correlation energy per electron of a gomogenous electron gas, $\varepsilon_{xc}[\rho]$, has been calculated by several approaches such as many-boty pertubation theory [54] and quantum Monte-Carlo methods [55]. As a result, $\varepsilon_{xc}[\rho]$ is quite accurately known for all densities of interest in solid state chemistry. There are different analytical forms with different coefficients in their representattion of the exchange-correlation terms. These coefficients are not adjustable parameters, but rather they are determined through first principle theory. There are two types of exchange-correlation terms, one for the energy and one for the potential. The energy terms are represented as follows

$$\varepsilon_{xc} = \varepsilon_x + \varepsilon_c \tag{2.11}$$

where ε_x is the exchange energy

$$\varepsilon_x = -\frac{3}{2}(\frac{3\rho}{\pi})^{\frac{1}{3}} \tag{2.12}$$

and ε_c is correlation energy

$$\varepsilon_c = -c\left[(1+x^3)ln(1+\frac{1}{x}) + \frac{x}{2} - x^3 - \frac{1}{3}\right]. \tag{2.13}$$

their corresponding potentails are

$$\mu = \frac{\partial(\rho\varepsilon)}{\partial\rho}, \tag{2.14}$$

$$\mu_x = -2(\frac{3\rho}{\pi})^{\frac{1}{3}} \tag{2.15}$$

and

$$\mu_c = -cln(\frac{1}{x}+1) \tag{2.16}$$

respectively. Where c = 0.0225, x = $\frac{r_s}{21}$, $r_s = (\frac{3}{4\pi\rho})^{\frac{1}{3}}$ The two terms are related by

$$\mu_{xc} = \frac{\partial[\rho\varepsilon_{xc}(\rho)}{\partial\rho} \tag{2.17}$$

Using the formulas given above, the exchange-correlation potential for any electron density $\rho(r)$ can be evaluated. Thus al terms of the effective one operator in the Kohn-Sham equations are defined and one can proceed with a computational implementation. The iterative, self-consistent procedure for

solving the Kohn-Sham equations is shown in Figure 2.1 [56]. The electronic methods are also summarized in Figure 2.2 [56].

2.1.2 Generalized Gradient Approximation

Despite the remarkable success of the LDA, it has also limitations. For systems where the density varies slowly, the LDA tends to perform well, and chemical trends are well reproduced. In strong correlated systems were independent particle picture breaks down, the LDA is very inaccurate. For example, the LDA has been applied to high T_c superconductors, but finds several to be metallic, when in reality they are insulating at 0K [57]. LDA finds the wrong ground states in many simpler cases by underestimating bondlengths and lattice constants by roughly 10% [58].

In LDA the weak bonds are too short and the calculated binding energies are typically too large [59]. Beyond the LDA the exchange and correlation in an inhomogeneous system is non-local with respect to electrons it surrounds, and this is referred to as gradient correcton or generalized gradient approximation GGA, which was introduced by Perdew and Wang [60], it was found to overestimate bondlenghts and lattice constants. The GGA exchange correlation energy is written as

$$E_x^{GGA}c(n) = \int drn(r)\varepsilon_{xc}^{GGA}[n(r), \|\bigtriangledown n(r)\| \tag{2.18}$$

where $\varepsilon_x c$ is the exchange correlation energy and n(r) is the gradient term. The GGA has been widely used and have proved to be quite successful in correcting some of the deficiencies of the LDA. The correct magnetic ground

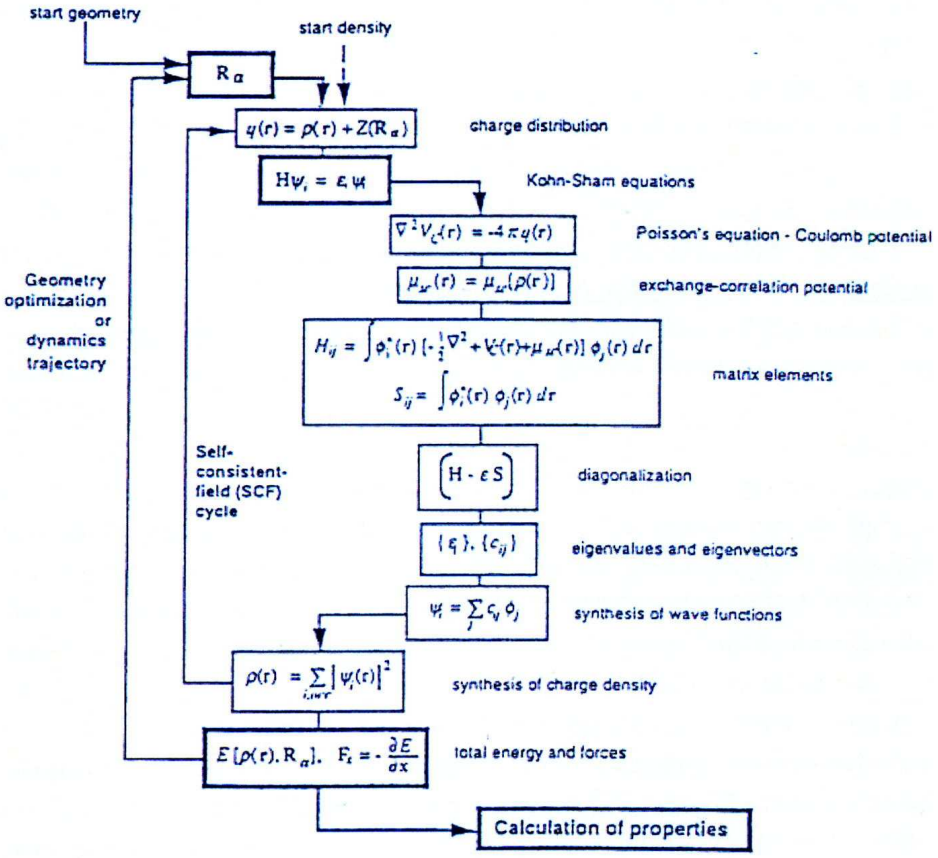

Figure 2.1: Schematic representation of SCF and geometry optimization methods used in DFT

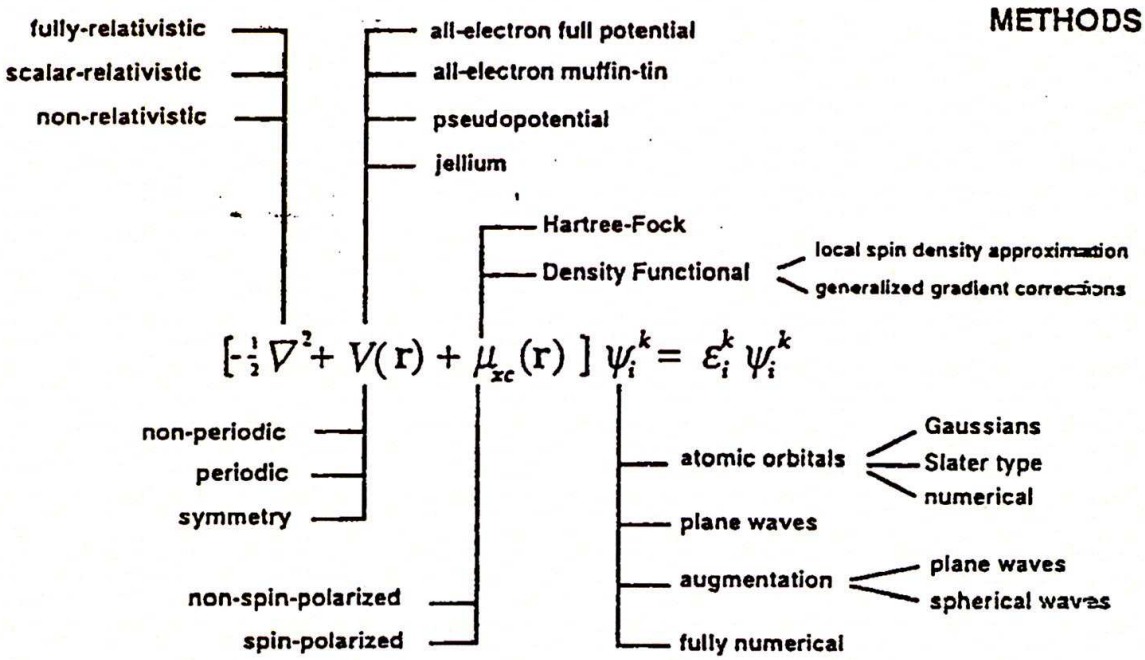

Figure 2.2: Flow chart of electronic structure methods used for solving Kohn-Sham equations

state was predicted for ferromagnetic Fe [61] and antiferromagnetic Cr and Mn [62, 63, 64].

2.2 Plane-wave pseudopotential method

The plane-wave pseudopotential method has become a powerful and reliable tool to study the properties of a broad class of materials. The emphasis on the total energy and the related properties makes plane-wave pseudopotential a technique suited to structural studies based on a quantum-mechanical treatment of the electronic subsystem. The main idea of the method is to simplify the DFT problem by considering only valence electrons. Core electrons are excluded under the assumption that their charge density is not affected by the changes in the chemical environment. This approximation is well understood and gives a number of computational advantages i.e.

(i) The pseudopotential is much weaker in the core region than the true coulomb potential of the nucleus, and it does not have a singularity at the position of the nucleus.

(ii) The resulting pseudo-wave functions are smooth and nodeless in the core region.

(iii) There are fewer electronic states in the solid state calculation.

(iv) Both pseudopotentials and pseudo-wave functions can be efficiently represented using a plane wave basis set. The plane-wave pseudopotential method is applicable to large systems that are subject to 3D periodic boundary conditions.

2.2.1 Plane-wave basis

An infinite plane-wave basis set is used to expand the electronic wave functions of the system. The method is described well by using Bloch's theorem, which state that the electronic wavefunstion at eack k-point can be expanded in terms of a discrete plane-wave basis set i.e.

$$\psi_{\mathbf{k}i}(\mathbf{r}) = exp\left[i\mathbf{k}.\mathbf{r}\right] f_i(\mathbf{r}). \tag{2.19}$$

This expression has a wavelike and cell-periodic part. The function $f_i(\mathbf{r})$ defines the periodicity of the solid and can be expanded using a basis set with a discrete set of plane waves, written as

$$f_i(\mathbf{r}) = \sum_G C_{i,G} exp\left[i\mathbf{G}.\mathbf{r}\right] \tag{2.20}$$

where the G are the reciprocal lattice vectors of the periodic cell. Thus each electronic wave function can be written as a sum of plane waves,

$$\psi_{\mathbf{k}i}(\mathbf{r}) = \sum_G C_{i,k+G} exp\left[i(\mathbf{k}+\mathbf{G}).\mathbf{r}\right] \tag{2.21}$$

where $C_{i,k+G}$ are the coefficients for the plane waves that need to be solved and depend entirely on the specific kinetic energy, $\left(\frac{\hbar^2}{2m}\right)|k+G|^2$.

The convergence of this expansion is controlled by the choice of the kinetic energy cutoff. In practice, the plane wave basis set is limited by including all plane waves whose kinetic energies are less than some particular cutoff energy E_{cut}. Introduction of an energy cut-off to the discrete plane-wave basis set produces a finite basis set. The truncation of the plane-wave basis set at

a finite cut-off energy will lead to an error in the computed total enenrgy. However it is possible to reduce the magnitude of the error by increasing the value of the cut-off energy. In principle, the cut-off energy should be increased until the calculated total energy has converged.

The plane-waves are used as a basis set for the electronic wave functions, and substitution of equation 2.21 into equation 2.5 (Kohn-Sham equation) and the integration over r gives the following secular equation

$$\sum_{G'} \left[\frac{\hbar^2}{2m} |\mathbf{k}+\mathbf{G}|^2 \delta_{GG'} + V_{ion}(\mathbf{G}-\mathbf{G}') + V_H(\mathbf{G}-\mathbf{G}') \right] C_{i,k+G'} = \varepsilon_i C_{i,k+G} \tag{2.22}$$

We see that the first contribution, the kinetic energy, is diagonal, whereas the various potential contributions are given by their Fourier transforms. This may be written in terms of the Hamiltonian matrix elements $\mathrm{H}_{k+G,k+G'}$ as

$$\sum_{G'} H_{k+G,k+G'} C_{i,k+G'} = \varepsilon_i C_{i,k+G'}. \tag{2.23}$$

The solutions of the Kohn-Sham equation are obtained by diagonalizing the Hamiltonian matrix elements $\mathrm{H}_{k+G,k+G'}$. The size of these matrix elements is determined by the choice of energy cut-off ($\frac{\hbar^2}{2m}|\mathbf{k}+\mathbf{G}|^2$, and will be large for systems that contain both valence and core electrons.

Although Bloch's theorem states that the electronic wave funstions can be expanded using a discrete set of plane-waves, a plane-wave basis set is usually very poorly suited to expanding electronic wave functions because a very large number of plane- waves are needed to expand the tightly bound

core orbitals and to follow the rapid oscillation of the wave functions of the valence electrons in the core region. An extremely large plane-wave basis set would be required to perform all-electron cal culation, and a vast amount of computational time would be required to calculate the electronic wave functions. This problem can be overcome by the use of pseudopotential approximation [65, 66, 67].

2.2.2 The pseudopotential method

The physical properties of solids are dependent on the valence electrons to a much great extent than on the core electrons.In the pseudopotential method, the core electrons and the strong attractive coulomb potential inside the ionic core are replaced by a weaker pseudopotential that describes all the salient features of a valence electron moving through a crystal, including relativistic effects [66, 68]. Thus the original solid is now replaced by pseudo-valence electron and pseudo-ion cores. These pseudoelectrons experience exactly the same potential outside the core region as the original electrons but have a much weaker potential inside the core region. Figure 2.3 illustrates the ionic potential (Z/r), the valence wave function (ψ_v), the corresponding pseudopotential (V_{pseudo}), and pseudo-wave function (ψ_{pseudo}) respectively [68].

The valence wave functions oscillate rapidly in the region occupied by the core electrons due to the strong ionic potential in this region. The oscillations mantain the orthogonality between the core and valence wave functions, which is required by the exclusion principle. The pseudopotential is

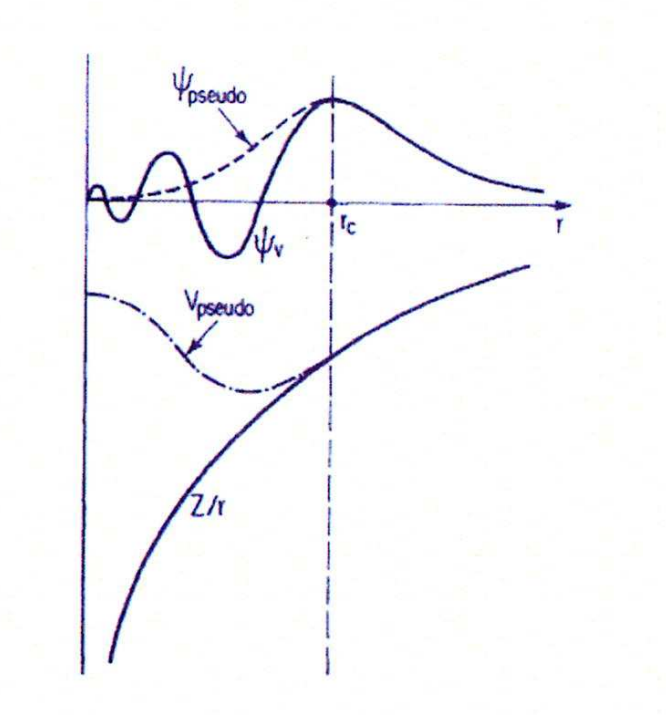

Figure 2.3: Schematic illustration of all-electron potential (solid line) and pseudoelectron potential (dashed line) with the corresponding valence wave function (ψ_v) and pseudo-wave function (ψ_{pseudo}) [68].

constructed ideally, so that its scattering properties or phase shifts for the pseudo wave functions are identical to the scattering properties of the ion and the core electrons for the valence wave functions, but in such a way that the pseudo wave functions have no radial nodes in the core region. In the core region, the total phase shift produced by the ion and the core electrons will be greater by π, for each node that the valence functions had in the core region, than the phase shift produced by the ion and the valence electrons. Outside the core region the two potentials are identical, and the scattering from the two potential is indistinguishable.

The advantage of using the pseudopotential approximation is that it allows the electronic wave function to be expanded using a much smaller number of plane-wave basis states, so that a smaller amount of computational time would be required for convergence of the energies. The pseudopotential has the form

$$V_{NL} = \sum_{lm} |lm\rangle V_l \langle lm| \,, \tag{2.24}$$

where $|lm\rangle$ are the spherical harmonics and V_l is the pseudopotential for angular momentum l. The majority of the pseudopotential currently used in the electronic structure is generated from all electron atomic calculations.

A pseudopotential that uses the same potential for all the angular momentum components of the wave function is called a local pseudopotential. A local pseudopotential is a function that only depends on the distance dependence of the potential. The norm-conserving pseudopotential (NCP) by Kleinmann and Bylander [69] is an example of a non-local pseudopotential,

using a different potential for each angular momentum component of the wave function. Recently, the ultrasoft pseudopotential (USP) put forward by Vanderbilt has been implemented in plane-wave calculations. In this scheme the pseudo-wave-functions are allowed to be as soft as possible within the core region. They cover a wide range of atoms, including the transition metals. In this thesis we use the ultrasoft pseudopotential by Vanderbilt [70] within the CASTEP program [71, 72] for total energy calculations since they give accurate results for the systems we are interested in.

2.2.3 Brillouin zone sampling

Many calculations in crystals involve the averaging over the Brillouin zone [73] of a periodic functions of wave vector. Such calculations are often long and complicated. and in principle require knowledge of the value of the function at each k point in the Brillouin zone. Electronic states are allowed only at a set of k points determined by the boundary conditions that apply to bulk solid. Due to the Bloch theorem, the infinite number of electrons in the solid is accounted for by an infinite number of k points. and only a finite number of electronic states are occupied at each k point. The occupied states at each k point contribute to the electronic potential in the bulk solid so that, in principle, an infinite number of calculations are needed to compute this potential. All required functions of k, in particular the potential are continous so the integral over the infinite number of k-points can be replaced by a sum over a finite, often small number.

Density functional theory approximate the **k**-space integrals with a finite

sampling of **k**-points. Special **k**-point schemes have been developed to use the fewest possible **k**-points for a given accuracy, thereby reducing the computational cost. The most commonly used scheme is that of Monkhorst and Pack [74]. Other sampling scheme are those given by Chadi and Cohen [75], Joannopoulos and Cohen [76]. Monkhorst proposed a scheme where the k are distributed homogeneously in the Brilloin zone according to

$$k = x_1\mathbf{b_1} + x_2\mathbf{b_2} + x_3\mathbf{b_3} \tag{2.25}$$

where b_1, b_2,b_3, are the reciprocal lattice vectors, and

$$x_i = \frac{l}{n_i} \tag{2.26}$$

where $l = 1$, ..., n_i, where n_i are the folding parameters. MP-This essentially means that the sampling k-points are distributed homogeneously in the brilloinn zone , with rows or columns of k-points running parallel to the reciprocal lattice vectors that span the Brilloiun zone. In this work, for CASTEP calculations we will use the Monkhorst and Pack sampling scheme to generate efficient and accurate sets of special points in the BZ. In VASP we used Methfesset-Paxton [77] sampling method for the Brilloiun-zone integration in metals which converged with the number of sampling points, without the loss of precision of normal broadening techniques. The scheme can be applied to simple cubic tight-band as well at to band structures of simple and transition metals. The method promises general applicability in the fiels of total-enegy calculations and many-body physics.

The number of **k**-points necessary for a calculation depends entirely on the

system as the treatment of metals, semiconductors and insulators is different. Metallic systems require an order of magnitude more k-points than semiconductor and insulating systems. Dense **k**-space meshes to define the Fermi surface precisely. If the **k**-points sampling does not give a well converged total energy, then a much denser set of **k**-points must be used to reduce the errors and ensure the required convergence.Therefore,choosing a sufficiently dense mesh of summation is crucial for the convergence of the results, and is therefore one of the major objectives when performing convergence tests.

2.2.4 Smearing

In solid-state one-electron and many-body calculations, integrals fo periodic functions over the Brillouin zone are routinely made in the evaluation of the densities of states, charge densities etc. In metals the Fermi surface (FS) of the system is no longer a sharp feauture in the BZ, and the number of electronic wavevectors(k-points) needed to sample the Brillouin zone is significantly reduced. Instead of having to hedge in the FS with thousands of k-points, less than a hundred are always sufficient: enough of them will fall near enough to the FS to take into account its essential contribution to the free energy. Smearing schemes aim at reducing the number of sampling k-points needed to treat metals at 0K.

In these schemes, the smearing width depends on a fictitious temperature, which we will call a smearing temperature. We will denoted it σ to distinguish it from the physical temperature (T). Both of these quantities are related to an energy scale, thanks to the Boltzmann constant. The smearing energies

which are useful for k-point convergence properties are in the 0.2 to 1 eV range, and correspond to temperatures above 2000 K. In this work we used the coldsmearing and Methfessel-Paxton smearing for CASTEP and VASP calculations respectively.

2.2.5 Periodic boundary conditions

Computer simulation programs predicts the properties of a system in bulk. In this study we are not interested in surface effects. Our simulations track only a small number of particles in order not to slow dowm the computation. As a result most of the atoms are near the edge of the sample, that is near its surface. To eliminate surface effect from the computation we use a trick called periodic boundary conditions(PBC). When using PBC, particles are enclosed in a box, and the cubical simulation box is replicated to infinity by rigid translation in all the three cartesian directions, completely filling the space.

If one of our particles is located at position **r** in the box, we assume that this particle really represents an infinite set of particles located at

$$\mathbf{r} + 1a + m\mathbf{b} + n\mathbf{c} \tag{2.27}$$

Where l,m,n are integer numbers and **a,b,c** are the vectors corresponding to the edges of the box. Each particle i in the box should be thought as interacting not only with other particles j in the box, but also with their images in nearby boxes. That is, interactions can "go through" box boundaries. It is clear that

(i) surface effects have been eliminated from the surface, and

(ii) the position of the box boundary has no effect(i.e. a translation of a box with respect to the particles leaves the forces unchanged).

2.2.6 CASTEP

CASTEP is premier density functional theory quantum mechanical code to simulate the properties of solids, interfaces, and the surfaces for a wide range of materials classes including ceramics, semiconductors and metals. CASTEP employs plane-wave techniques to deal with materials with weak pseudopotentials. First principle calculations allow researchers to investigate the nature and the origin of the electronic, optical and structural properties of a system without the need for any experimental input, with the ecxeption of the atomic number of mass of the constituent atoms.

CASTEP is well suited to research problems in solid state physics, materials science, chemistry and chemical engineering. In these areas, researchers can employ computer simulations to perform virtual experiments, which can lead to tremendous results. This method can calculate forces acting on atoms and stress on the unit cell. CASTEP relies on a plane-wave basis, pseudopotentials and the use of density functional theory to describe the valence electrons in a model. Other ingredients include fast Fourier transforms and minimization of the total energy rather than matrix diagonalization.

2.2.7 VASP

VASP is a package for performing ab-initio quantum mechanical molecular dynamics(MD) using pseudopotentials and plane-wave basis set. The approach implemented in VASP is based on a finite-temperature LDA and an exact evaluation of the instanteneous electronic ground state at each MD-step using efficient matrix diagonalization schemes and an efficient Pulay mixing. The interaction between ions and electrons is described using Vanderbilt pseudopotentials(USPP) or the projector augmented wave(PAW). Both techniques allow a considerable reduction of the necessary number of plane-waves per atom for transition metals and first row elements.

The projector-Augmented wave implemented in VASP reconstructs the full all-electron density and avoids the necessity of nonlinear core-corrections.VASP uses efficient matrix diagonalisation schemes and an efficient Pulay/Broyden charge density mixing, these techniques avoid all problems occuring in the original Car-Parinello method, which is based on the simultaneous integration of electronic and ionic equations of motion.

The plane-wave basis set in VASP offers two main advantages:

(i) Control of basis-set convergence, which is crucial for the accuracy of calculations is almost trivial, in particular for the prediction of forces, stresses and pressures. Very large local basis sets are required to match the accuracy of a well convergeg plane-wave calculations.

(ii) The calculations of the forces acting on the atoms and ofthe stresses on the unit cell using Hellmann-Feyman theorem [78] is straightforward.

VASP uses a rather "traditional" and "old fashioned" self-consistency cycle to calcualate the electronic ground-state. The combination of this schemes with efficient numerical methods leads to an efficient, robust and fast scheme for evaluating the self-consistent solution of the Kohn-Sham functional.

2.2.8 Heats of formation

For the study of the relative stability of binary alloys, it is convenient to consider the heats of formation which is calculated as follows:

$$\Delta H_f = E_{A_xB_y} - xE_A - yE_B \tag{2.28}$$

Where E_A, E_B and $E_{A_xB_y}$,are the equilibrium total energies of A, B and alloy A_xB_y in a given underlying lattice (bcc, fcc or hcp). x and y are atomic concentrations of A and B. The equilibrium total energies of an alloy and its constituents are calculated using VASP. The lower the heat of formation of an alloy, the more stable it becomes.

Chapter 3

Structural, thermodynamic and elastic properties

3.1 Introduction

In this chapter we present the structural and electronic properties of Pt, Cr, Ru and their alloys obtained using the computational methods that are outlined in chapter 2. The calculated results are compared with the available previous theoretical and experimental results. The structural properties such as lattice parameters, atomic positions will be given and compared with the experimental results. We also present the heats of formation and the magnetic moments of the alloys.

3.2 Structural properties of metallic Pt, Cr and Ru

Ground-state properties of metals are well described by the DFT approach. The self-consistent DFT calculations were carried-out for the ground state structure of fcc Pt, bcc Cr and hcp Ru. The are two conditions to be con-

sidered for the accurate calculation for the DFT method; one is the energy cut-off convergence for the plane wave expansion of the wavefunction and the other is the number of k points used to sample k space in the plane-wave expansion. In CASTEP the Monkhorst-Pack scheme for k-sampling was used to select an optimal set of k points of the Brullouin zone such that the greatest possible accuracy is achieved given a particular number of k points used. In VASP we used the Monkhorst-Pack scheme, together with a Methfessel Paxton smearing of 0.2 eV to allow the partial occupancy near the Fermi level.

K-spacing of 0.103/Å and was used for cubic metals which sufficiently converged the energy to 1meV. In order to reduce the number of plane waves required, the chemically inactive core electrons were replaced with an untra-soft pseudo potential [70, 79]. The density mixing scheme based on the Pulay and Normal(blocked Davidson) algorithms were used for CASTEP and VASP respectively to find the electronic ground state [79, 80]. The effect of the plane-wave cut-off on the calculated total energy was considered, i.e. we carried out single point energy calculations where we increased cut-off energy and monitored the convergence of energy of approximately 1meV/atom. The converged energies are shown in Table 3.1.

From the single-point calculations we computed the kinetic energy cut-off of metallic Pt,Cr and Ru as 400eV, 500eV and 500 eV respectively. In order to determine the optimal energy cut-off for the plane-wave expansion the total energy was computed as a function of the cut-off as shown in Figure 3.1. The energy cut-off convergence depends almost on the atom species and

Table 3.1: Computed lattice parameters, cut-off and total energies for metallic Pt, Cr and Ru

Materials	$E_{cut-off}$ (eV)	E_T (kJ/mol)	a (Å)
Pt	400	-584.266	3.998
			3.924^{exp}[81]
Cr	500	-929.385	2.851
			2.88^{exp}[82]
Ru	500	-894.437	2.706
			2.71^{exp}[83]

is taken to be large enough for the present lattice structure and boundary conditions.

We further performed a number of calculations which lead us to the relevant choice of smearing width for this study. We varied k-points (4x4x4 to 20x20x20) and a smearing width (0.02 to 0.2 eV) and observed the change in energies. The results for Pt is shown in Figure 3.2, where we plotted three energies E, E_0 and F from CASTEP output files as a function of smearing width at different k-points. Where E is the final energy printed by CASTEP, E_0 is the energy at 0K i.e the corrected final energy of the system and F = E - TS is the final Helmholtz free energy.

3.3 Alloys

3.3.1 Introduction

In this section we explore the binary alloys formed by transition metals (Pt, Ru and Cr) with higher melting points. Six different composition of binary alloys are studied, namely PtCr, RuCr, Pt_3Cr, $PtCr_3$, Ru_3Cr and $RuCr_3$.

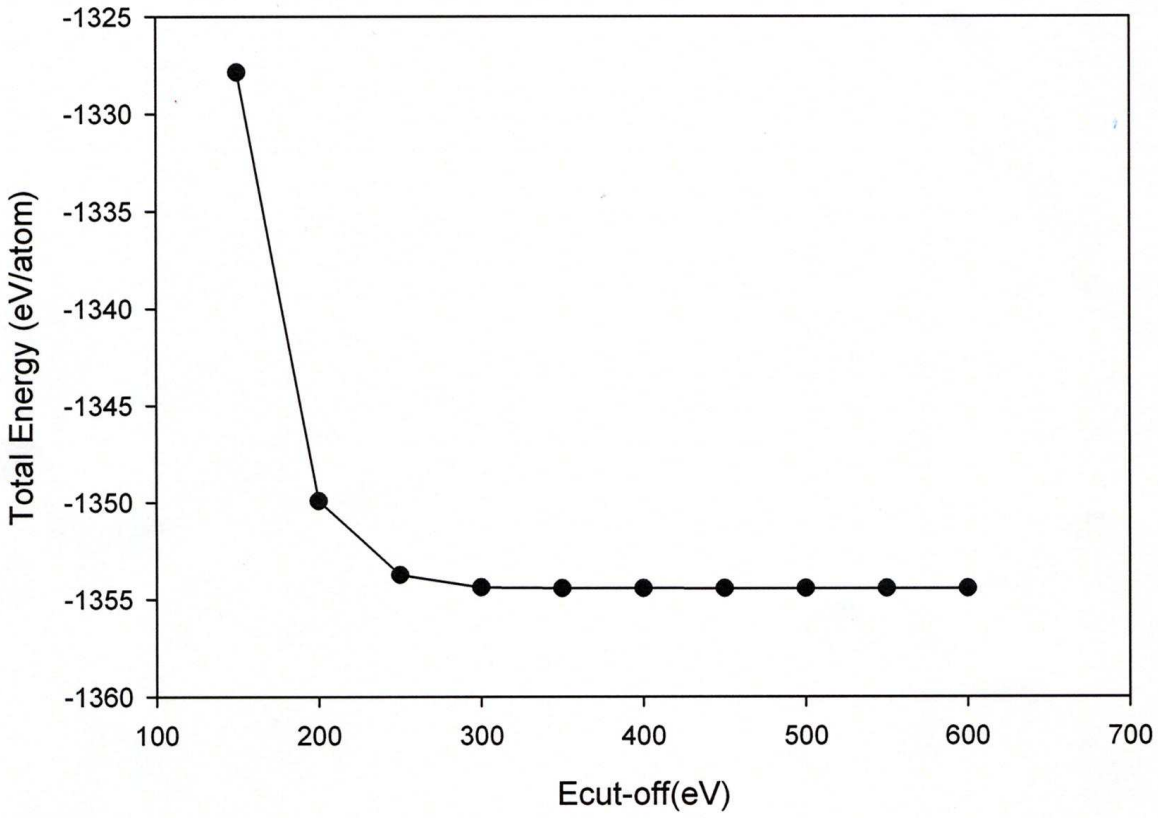

Figure 3.1: Total energy vs kinetic energy cut-off for Pt

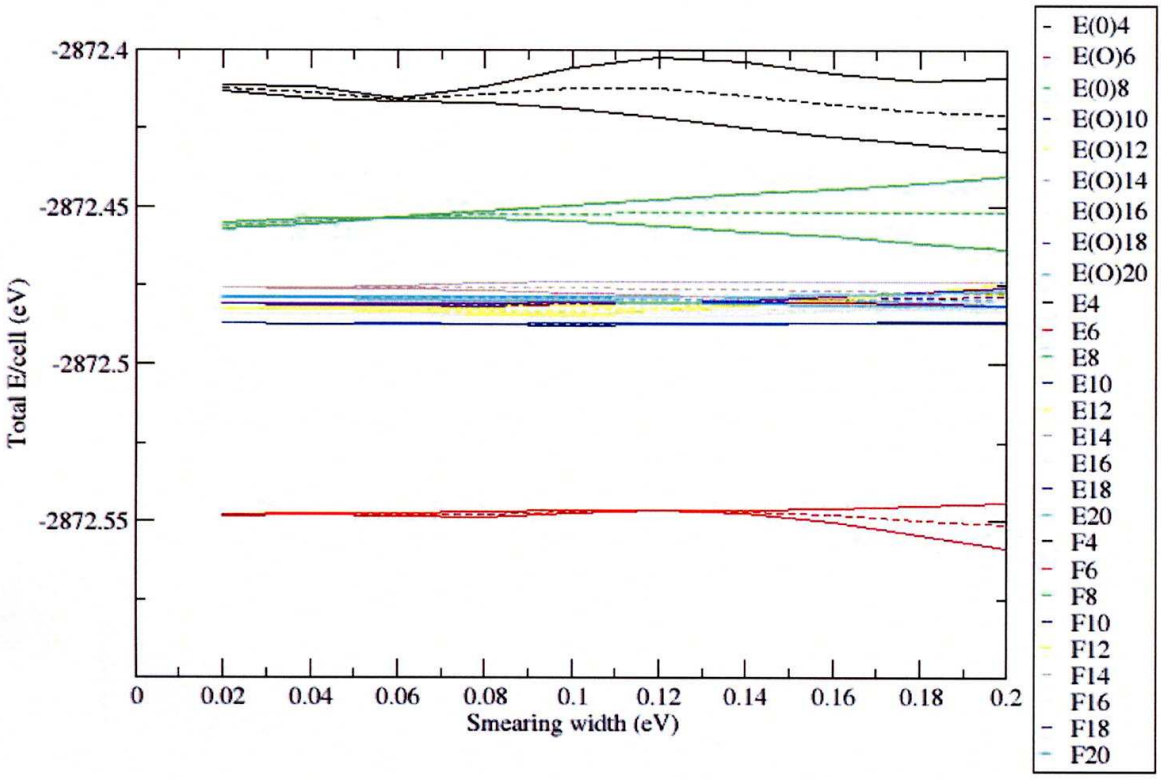

Figure 3.2: Pt smearing width vs E

Table 3.2: Calculated and experimental lattice constants and heats of formation (ΔH_f) of Pt_3Cr in the $L1_2$, A15, DO'_C, DO_C and tP16 phases

	Phase	Prototype notation	a (Å)	a $_{exp}$ (Å)	c/a (Å)	ΔH_f (eV/atom)
Pt_3Cr	$L1_2$	Cu_3Au	3.920	3.873 [84]		-0.2601
.	A15	Cr_3Si	4.963			0.1147
	DO_C	U_3Si	5.541		1.416	-0.2597
	DO'_C	Ir_3Si	5.547		1.416	-0.2597
	tP16	$GaPt_3$	5.545			-0.2593

For each A_3B composition we studied five different phases, $L1_2$, A15, tP16, DO_C and DO'_C.

3.3.2 Lattice constants, heats of formation and magnetic moment

The calculations were performed at experimental lattice constants in the framework of DFT by CASTEP and VASP codes. During the self-consistency cycles, the Brillouin zone integration was performed using 0.103/Å k-spacing. Table 3.2 summarizes the optimized lattice constants and magnetic moments for studied systems together with those of previous studies, theoretical and experimental. Other previous calculations employed different exchange correlation functionals.

Our computed lattice parameters are slightly larger than the experimental and theoretical results. It is owing to the GGA approximation, which always overestimates the results. The GGA results are in good agreement with calculations such as linear combination of atomic orbitals (LCAO), LMTO and FLAPW. We have calculated the equilibrium lattice constants and the heats

Table 3.3: Calculated and experimental magnetic moment (per unit cell) of Pt_3Cr in the $L1_2$, A15, DO_C, $DO_C^{'}$ and tP16 phases.

Phase	Approach	Magnetic moment (μB)
$L1_2$	This work GGA	2.619
	LAPW	2.601 [86]
	LMTO	2.623 [87]
	ASW	2.61 [88]
	Magnetometer	2.52 [89]
	Neutron	2.52 [90]
A15	This work	0.001
DO_C	This work	2.690
$DO_C^{'}$	This work	2.689
tP16	This work	2.726

of formation of the $L1_2$, A15, tP16, DO_C and $DO_C^{'}$ phases of Pt_3Cr. The calculations have predicted structures with negative heats of formation, $L1_2$, tP16, DO_C and $DO_C^{'}$ which are therefore expected to be stable. Their heats of formation are almost of the same magnitude and the relaxed structure show no rotation i.e. u = 0 (u = x - 0.25) where u is the atomic displacement. We observed that the cubic $L1_2$ Pt_3Cr is the most stable structure in agreement with the experiments. In contrast with Pt-Cr, the Pt_3Al takes the non-cubic $DO_C^{'}$ and tP16 (brittle) as its ground state as compared with the $L1_2$ (ductile) phase [85].

Table 3.3 presents the detailed comparison of the computed magnetic moments of all the studied phases of Pt_3Cr with the experimental results and some previous theoretical studies. The magnetic moment of a material consists of contributions from spin and orbit polarization. The orbit moment is nearly quenched in 3d and 4d elements, and spin polarization contributes

the majority of the magnetic moment. The spin-polarized calculations were performed for Pt_3Cr in the $L1_2$ phase. The total spin moment (μB) is the difference of the spin up and spin down charges, which is directly available from ab-initio calculations. μB is usually referred to as "magnetic moment".

There have been quite a few theoretical and experimental studies for the magnetic properties of Pt_3Cr, The results are shown in Table 4.3, including our calculated (GGA-PBE) total magnetic moment. Our results are in good agreement with the experimental results. There is a very good agreement between ASW, LMTO and our GGA results which gives magnetic moment of 2.61 μB, 2.623 μB and 2.601 μB respectively. These results lead us to conclusion that Pt_3Cr should be charecterized as a ferrimagnet in agreement with experiments [89, 90, 91, 92, 93, 94]. The previously determined magnetic moments (LMTO, ASW etc) were predominantly localized on the Cr site, with the moment of Pt site being very small and opposite in sign to the Cr moment. The d states of the 3d Cr atoms are located near the top of the Pt d band and form relatively 3d bands. As one proceeds from lighter to heavier 3d elements, the up-spin 3d bands is first filled , and then electrons start to occupy the down-spin 3d band with increasing atomic numebr of the 3d elements. Recent ab-initio calculations [95] reveal that spin polarization or magnetization is responsible for $L1_2$ ordering in Pt_3Cr.

The results of $PtCr_3$ in Table 3.4 indicate the negative heat of formation for the A15 phase whereas all the studied phases have positive heats of formation which are close to zero. It is apparent that the $PtCr_3$ A15 phase is the most stable structure. The A15 phase has the lowest energy and the

Table 3.4: Calculated lattice constants, heats of formation and magnetic moments (per unit cell) of $PtCr_3$ $L1_2$, A15, DO_C, $DO_C^{'}$ and tP16 phases.

Phase	Prototype notation	a (Å)	ΔH_f (eV/atom)	Magnetic moment (μB)
$L1_2$	Cu_3Au	3.708	0.0211	0.0000
A15	Cr_3Si	4.677	-0.0144	0.0539
DO_C	U_3Si	5.253	0.0237	0.0000
$DO_C^{'}$	Ir_3Si	5.252	0.0237	0.0000
tP16	$GaPt_3$	5.252	0.0235	0.0000

Table 3.5: Calculated lattice constants and heats of formation of Ru_3Cr and $RuCr_3$ in the $L1_2$, A15, DO_C, $DO_C^{'}$ and tP16 phases.

	Phase	Prototype notation	a (Å)	ΔH_f (eV/atom)
Ru_3Cr	$L1_2$	Cu_3Au	3.774	0.0948
	A15	Cr_3Si	4.788	0.3225
	DO_C	U_3Si	5.325	0.0859
	$DO_C^{'}$	Ir_3Si	5.325	0.0859
	tP16	$GaPt_3$	5.270	0.0859
$RuCr_3$	$L1_2$	Cu_3Au	3.678	0.2378
	A15	Cr_3Si	4.631	0.0796
	DO_C	U_3Si	5.197	0.2383
	$DO_C^{'}$	Ir_3Si	5.197	0.2383
	tP16	$GaPt_3$	5.197	0.2383

highest magnetic moment of 0.0539 μB. The lattice constants and the heats of formation of the DO_C, $DO_C^{'}$ and tP16 phases are quite close to each other. When making a comparison between Pt_3Cr and $PtCr_3$ results, we observed that the alloys with more Pt additions are stable than those with more Cr. This is due to the poor ductility of Cr at ambient temperature, a problem which it shares with molybdenum (Mo) and tungsten (W).

More studies were conducted on the RuCr system, which is complicated,

Table 3.6: Calculated lattice constants and heats of formation of PtCr and RuCr in the B2 and $L1_0$ phases.

	Phase	Prototype notation	a (Å)	c/a (Å)	ΔH_f (eV/atom)
PtCr	B2	CsCl	3.119		-0.0268
	$L1_0$	CuAu	3.782	1.017	-0.0671
RuCr	B2	CsCl	2.989		0.1874
	$L1_0$	CuAu	3.776	0.962	0.0675

hence its literature is scarce. The phase diagram of RuCr is not well understood, however the experimentalist are modifying the current phase diagram. It is reported that RuCr contains two intermetallics $Cr_2Ru(\sigma)$ and Cr_3Ru. We look at five phases of $RuCr_3$ and Ru_3Cr, and the results are reported in Table 3.5. The heats of formation of all studied compositions of Ru-Cr are positive and very close to zero, especially for $RuCr_3$ A15 phase and Ru_3Cr DO_C, $DO_C^{'}$ and tP16 phases. These results suggest that all the studied $RuCr_3$ phases are not stable. Hence it might be necessary to apply doping to the system and observe the effect on the heats of formation, particularly on $RuCr_3$ A15 phase where there is an evidence of its presence experimentally, and has a relatively lower heat of formation when compared to all studied phases shown in Table 3.5.

Lastly we predicted the heats of formation for AB composition of PtCr and RuCr alloys. The results are shown in Table 3.6. From the results it is apparent that PtCr $L1_0$ is the most stable structure as compared with the B2 phase. Whereas the RuCr systems are all unstable even though the heat of formation for $L1_0$ is very close to zero.

3.3.3 The effect of doping on $RuCr_3$ A15 structure

As indicated in previous chapters one of the aims of this project is to search for the materials that are stronger and corrosion resistant. RuCr alloys is one of the targeted alloys, however, thus far the performed calculations predict all studied phases of RuCr as unstable. Our next step is to examine the effect of doping on the unstable $RuCr_3$ A15 structure. The calculations on the doped system were performed with a 0.103/Å Monkhorst-Pack k-spacing. The Ni dopant was introduced to reduce the heats of heats of formation of the A15 $RuCr_3$ structure. We doped the structure with two Ni atoms at three different positions using the VASP and CASTEP codes.

Table 3.7 presents the effect of doping on the heats of formation and lattice constants of $RuCr_3$ A15 structure. It is noted from the VASP results that Ni dopant reduces the lattice constants at all positions, and increases the heats of formation. The lattice constants for CASTEP exhibits a different trend compared to VASP. The lattice constant at position 1 is increased, and later decreased at position 2 and three. Heats of formation from CASTEP and VASP code follow a similar trend, however the VASP heats of formation are significantly increased as compared to CASTEP results. The VASP heats of formation for the doped and undoped system are 0.0796 eV/atom and 0.1009 eV/atom, where for CASTEP we computed 0.0794 eV/atom and 0.0932 eV/atom for the doped and undoped system. It is clear that the introduction of Ni as a dopant increases the heats of formation, so the doped $RuCr_3$ A15 system remain unstable.

Table 3.7: The doping effect on $RuCr_3$ A15 phase

CODE	SYSTEM	a($\AA$)	ΔH_f (eV/atom)
VASP	undoped	4.631	0.0796
	doped pos(1)	4.616	0.1009
	doped pos(2)	4.578	0.1009
	doped pos(3)	4.478	0.1009
CASTEP	undoped	4.623	0.0794
	doped pos(1)	5.531	0.0832
	doped pos(2)	4.589	0.0932
	doped pos(3)	4.589	0.0932

3.3.4 Pressure effect $RuCr_3$ A15 structure

Here we report the heats of formation obtained in normal conditions (P = 0) and under pressure from 1 GPa to 5 GPa. The results obtained at P = 0 is 0.0796 eV/atom which indicates that the system is unstable. Calculations under pressure do not predict a change of stability with increasing pressure, the system remains unstable in agreement with the results on the effect of doping, where the heats of formation for A15 $RuCr_3$ were predicted as 0.0796 eV/atom and 0.1009 eV/atom for the doped and undoped system respectively.

3.3.5 Elastic constants

We investigate the elastic constants and moduli of Pt-Cr and Ru-Cr binary alloys within density functional theory in the framework of GGA. The planewave cut-off energy was 500 eV and the convergence of the calculations is 1 meV. The knowlegde of elastic constants is essential for many practical applications related to the mechanical properties of solids, for example,

Table 3.8: physical parameters and elastic constants C_{ij} in GPa of Pt_3Cr and $PtCr_3$ systems

System	C_{11}	C_{12}	C_{13}	C_{16}	C_{33}	C_{44}	C_{66}
$L1_2$ Pt_3Cr	330.3	181.2				113.0	
A15 Pt_3Cr	463.8	119.8				32.3	
Ll_2PtCr_3	350.7	208.7				173.3	
DO_C $PtCr_3$	445.5	102.83	220.0	2.460	325.8	205.0	-122.7
A15 $PtCr_3$	461.5	145.7				77.8	

thermoelastic stress, internal strain and fracture toughness [96]. Elastic constants determine the response of crystal to external forces. They play an important role in determining the strength of the material.

In Table 3.8 we list the elastic moduli for Pt_3Cr ($L1_2$ and A15 phases) and $PtCr_3$ ($L1_2$, DO_c and A15). It is found that C_{11} for Pt_3Cr increases from the $L1_2$ to A15 phase, whereas C_{12} and C_{44} decreases as we move from $L1_2$ to A15 phase. The same trend was observed in the C_{11}, C_{12} and C_{44} values of $PtCr_3$ from the $L1_2$ to A15 phase. We observed that the C_{44} is always smaller than the other elastic constants. Unfortunately there are no experimental data for checking our calculated elastic constants against.

From the calculated C_{ij} values, the bulk modulus (B), shear modulus (G) and Young's modulus (E) were estimated using the Voigt-Reuss-Hill approximation [97], the results are presented in Table 3.9. Bulk modulus represents the resistance to fracture, shear modulus represents the resistance to plastic deformation, while Young's modulus is the ratio between strain and stress, and is used to provide a measure of stiffness of the material, that is the larger the value of E the stiffer is the material.

Table 3.9: Bulk, shear and Young Modulus in GPa of Pt_3Cr and $PtCr_3$ calculated by using the Voigt-Reuss-Hill approximation [97]

System	Modulus	Voigt	Reuss	Hill
Pt_3Cr $L1_2$	Bulk	230.9	230.9	230.9
	Shear	97.6	93.7	95.6
	Young's	256.7	247.6	252.2
Pt_3Cr A15	Bulk	234.5	234.5	234.5
	Shear	88.2	47.9	68.0
	Young's	235.1	134.5	184.8
$PtCr_3$ $L1_2$	Bulk	256.0	256.0	256.0
	Shear	132.4	109.9	121.2
	Young's	338.8	288.5	313.7
$PtCr_3$ DO_C	Bulk	255.8	255.8	255.8
	Shear	102.4	190.9	146.6
	Young's	271.0	458.6	364.8
$PtCr_3$ A15	Bulk	251.0	251.0	251.0
	Shear	109.8	97.6	103.7
	Young's	287.5	259.1	273.3

Pugh [98] has proposed a simple relationship in which the ductile/brittle properties of metals could be related empirically to their elastic constants by the ratio (G/B) of shear modulus divided by bulk modulus. If the ratio $<$ 0.5 the material behaves in a ductile way. From Table 3.10 it is noted that ratio (G/B) based on Reuss moduli is less than 0.5 for studied Pt_3Cr phases and $PtCr_3$ $L1_2$ and A15 phases, indicatng that this structures are ductile in nature. However for $PtCr_3$ DO_c phase, the ratio is greater that 0.5 hence the material is expected to be brittle. The Ll_2 Pt_3Cr is ductile in agreement with the previous calculations of Chauke et.al [85], where the $L1_2$ Pt_3Al was predited to be ductile.

Pettifor [99] suggested that the angular character of atomic bonding in metals and compounds, which could be related to the brittle/ductile, could be described by the Cauchy pressure $C_{12} - C_{44}$. For metallic bonding Cauchy pressure is typically positive. On the other hand for directional bonding with angular character, the Cauchy pressure is negative, with larger negative pressure representing more directional characteristics. The positive values of the Cauchy pressure are noted in Table 3.10 and they follow the order of DO_c $PtCr_3$ $>$ A15 Pt_3Cr $>$ A15 $PtCr_3$ $>$ $L1_2$ Pt_3Cr $>$ $L1_2$ $PtCr_3$.

The heats of formation and independent lattice constants of PtCr and RuCr B2 and $L1_0$ phases are presented in Table 3.11. The elastic constants C_{11} and C_{44} of PtCr $L1_0$ are greater than those of the B2 phase. A different trend is observed for the C_{12} value of PtCr $L1_0$ which is less than B2 value.

Ledbetter [100] proposed that the bulk modulus B could be used as a measure of the average bond strength because it has a strong correlation with

Table 3.10: The calculated Reuss shear modulus G, Bulk modulus B, the ratio of (G/B) and the Cauchy pressure $C_{12} - C_{44}$ of Pt_3Cr and $PtCr_3$ phases

System	G	B	G/B	$C_{12} - C_{44}$
$L1_2$ Pt_3Cr	93.70	230.9	0.406	68.17
A15 Pt_3Cr	47.89	234.5	0.204	87.50
$L1_2$ $PtCr_3$	109.9	256.0	0.055	35.34
DO_c $PtCr_3$	190.9	255.8	0.746	225.5
A15 $PtCr_3$	97.6	251.0	0.389	67.9

Table 3.11: Heats of formation and elastic constants C_{ij} in GPa

System	ΔH_f (eV/atom)	C_{11}	C_{12}	C_{13}	C_{33}	, C_{44}	C_{66}
B2 PtCr	-0.027	122.7	204.0			118.0	
$L1_0$ PtCr	-0.067	378.5	187.7	159.1	420.8	178.3	213.0
B2 RuCr	0.187	243.2	218.2			132.0	
$L1_0$ RuCr	0.067	397.5	206.7	224.3	377.0	152.7	182.0

Table 3.12: Bulk, shear and Young Modulus in GPa

System	Modulus	Voigt	Reuss	Hill
PtCr B2	Bulk	176.9	176.9	176.9
	Shear	54.3	-210.5	-78.0
	Young's	148.3	-1046.4	-449.0
PtCr $L1_0$	Bulk	243.3	243.2	243.2
	Shear	158.7	146.3	152.5
	Young's	391.1	365.7	378.4
RuCr B2	Bulk	226.5	226.5	226.5
	Shear	84.2	27.4	55.8
	Young's	224.7	78.9	151.8
RuCr $L1_0$	Bulk	275.8	275.8	275.8
	Shear	131.9	118.8	125.3
	Young's	341.3	311.6	326.5

the cohesive energy or binding energy of atoms in crystal. It is interesting to note from Table 3.12 that the average Reuss bulk modulus of PtCr $L1_0$ = 243.2 GPa is larger than the bulk modulus of PtCr B2 = 176.9 GPa. This implies that the bond strength of PtCr $L1_0$ is greater than that of the B2 phase.

Hardness is related to the elastic and plastic properties of materials. Shear modulus is a significant qualitative predictor of hardness better than the bulk modulus. There is a linear relationship between hardness and shear modulus. As listed in Table 3.12, the bulk modulus 243.2 GPa and shear modulus 146.3 GPa for PtCr $L1_0$ are larger than the corresponding values of 176.9 GPa and -210.5 GPa. The negative value of the shear modulus of the B2 phase indicate that the B2 PtCr structure is elastically unstable. This observation is in good agreement with the previous stability prediction based on the heats of formation, which show $L1_0$ as the most stable structure. As a result the hardness of $L1_0$ is higher than that of the B2 phase.

Apart from the bulk and shear moduli, the elastic shear constant C_{44} is also an important parameter of predicting the hardness of a material. The calculated C_{44}, 178 GPa, of PtCr Ll_0 is large compared to that of B2 118 GPa, so its shear resistance to the shear stress should be significant. From the results in Table 3.12, $L1_0$ is expected to behave in a brittle way because of the Reuss ratio $(\frac{G}{B}) = 0.601$. On the other hand PtCr(B2), RuCr(B2) and RuCr($L1_0$) are ductile alloys with (G/B) of -1.199, 0.121 and 0.431 respectively. We further investigated the elastic properties of $RuCr_3$ A15 phase, and we have found the bulk modulus (B) = 277.5 GPa, shear modulus (G)

= 114.8 GPa and Young's modulus (E) = 300.2 GPa. The calculated elastic constants C_{11}, C_{12} and C_{44} are 448.3 GPa, 162.1 GPa and 101 GPa respectively. All positive eigenvalues of the elastic constant matrix show that the A15 phase of $RuCr_3$ is elastically stable, however, the structure is predicted as thermodynamically unstable with $\Delta H_f = 0.0796\ eV$ which is close to zero. The Cauchy pressure is positive for all the studied PtCr and RuCr structures indicating atomic bonding in the systems.

Chapter 4

Electronic and magnetic properties

4.1 Density of states

4.1.1 Introduction

The density of states (DOS) of a system describes the number of states at each level that are available to be occupied by electrons. A high DOS at a specific energy level means that there are many states available for occupation. A DOS of zero means that no states can be occupied at that energy level. From the DOS we can deduce the nature of materials and also predict the stability of the systems. In this chapter we present the results of the calculated DOS of metallic Pt, Cr, Ru and their alloys which will give more information of the studied systems.

4.1.2 Methodology

In calculations for metallic systems, the smearing width is introduced to eliminate discontinous changes in energy when an electron band crosses a

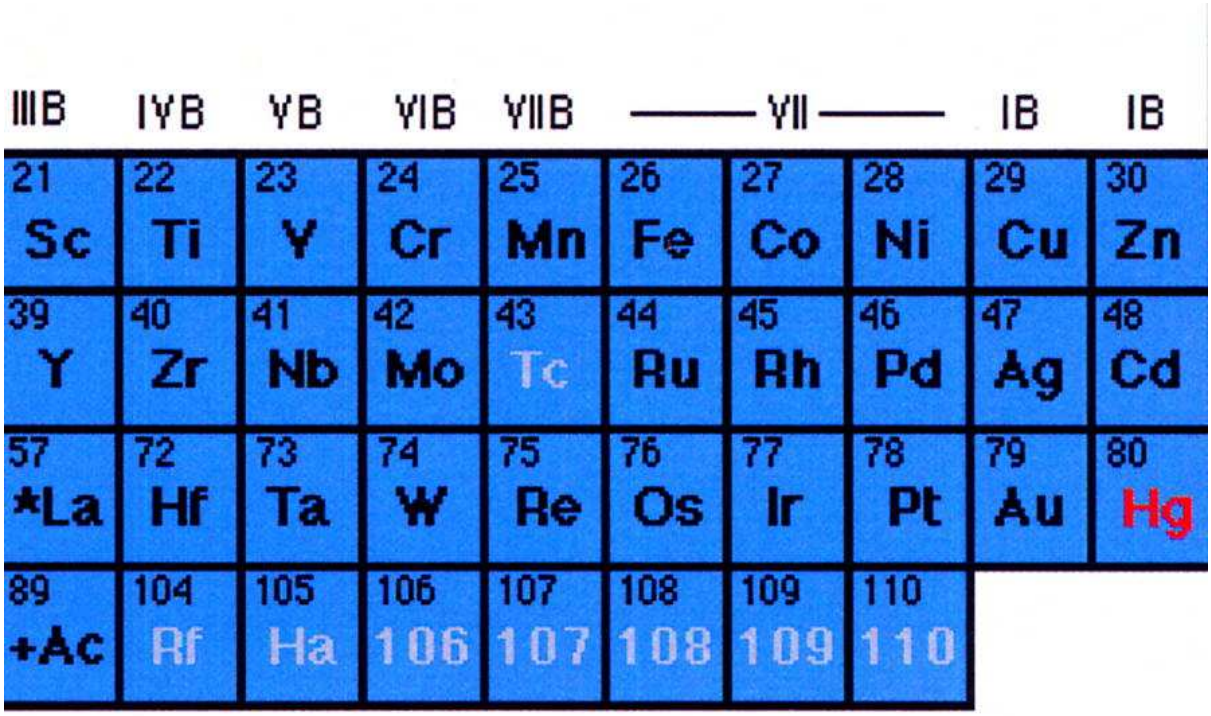

Figure 4.1: Periodic table of transition elements

Fermi-level during the self-consistent procedure. This smearing width was set to 0.1 eV to ensure the convergence of the self-consistence procedure. The ultra-soft pseudopotential was used to describe the electron-core interaction.

Pt, Cr and Ru are all transition metals belonging to the different groups of the periodic table as shown in Figure 4.1. Cr, Ru and Pt belong to 1^{st}, 2^{nd} and 3^{rd} rows respectively. Their electronic configurations are as follows Cr = [Ar]$4s^1 3d^5$, Ru = [Kr]$5s^1 4d^7$ and Pt [Xe]$4f^{14} 5d^9 6s^1$. In Cr, all the s and d subshells are half full. A full filled and half filled subshell lower energy, and gain some stability.

The calculated density of states of metallic Pt is shown in Figure 4.2. We

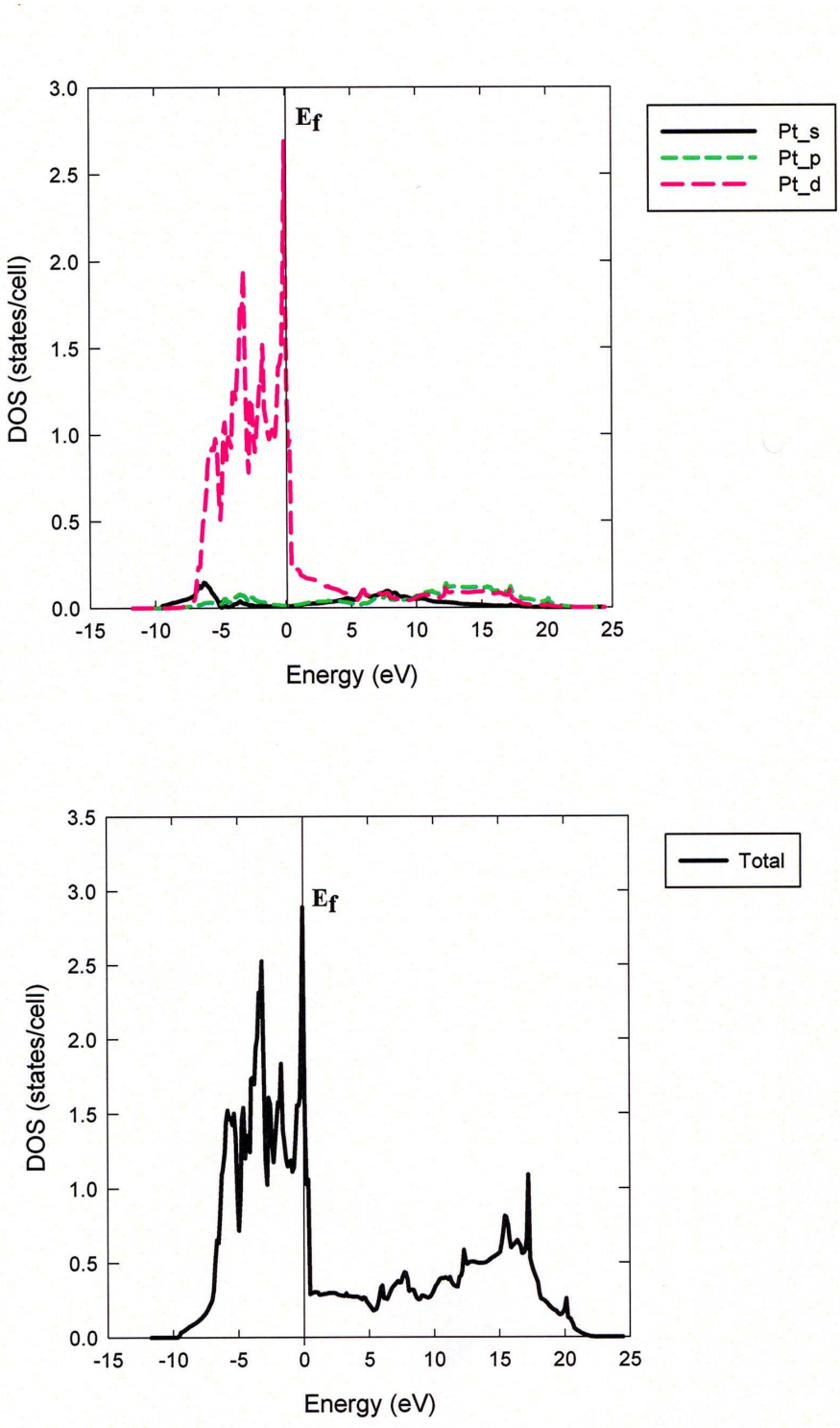

Figure 4.2: DOS of metallic Pt

can draw some conclusion from the DOS of Pt; firstly the DOS is continuous, there is no band gap between the valence and conduction band indicating that Pt is metallic. Secondly, contributions of the Pt s and p states are almost the same and the d-states contribute more to the DOS of Pt. The conduction band consists of the anti-bonding s, p and d states of Pt. The main contribution of the d-states can be seen in the valence band near the Fermi level. The Fermi level is located in the region of high DOS value, implying that the surface of Pt would be chemically inactive.

Figure 4.3 shows the calculated DOS of Ru. The majority and minority spins are split evenly though the Ru is normally a paramagnetic element. The up-spin and down-spin DOS are equal. The main contribution in both the valence and the conduction bands is from the d-states. The high peak of the valence-band DOS is located at ≈ 2.0 eV. The main peak of the anti-bonding d states is higher than the main peak of the bonding d-states. The energy difference between the main peak of valence band and that of conduction band is about 3.8 eV. The d-states of Ru at Fermi level are less compared to the d-states of Pt, this is expected because the 5d-states of Pt has higher energy that the Ru 4d states.

The spin-up DOS is the same as the spin-down DOS of metallic Cr, and these are shown in Figure 4.4. Our calculated DOS predicts Cr as a non-magnetic system which is not in agreement with recent work [101] that indicate Cr as an antiferromagnet system. The main peak of the valence band is located at 2.2 eV below the Fermi level, whereas the energy difference between the high peak in the valence band and conduction band is about 4.0

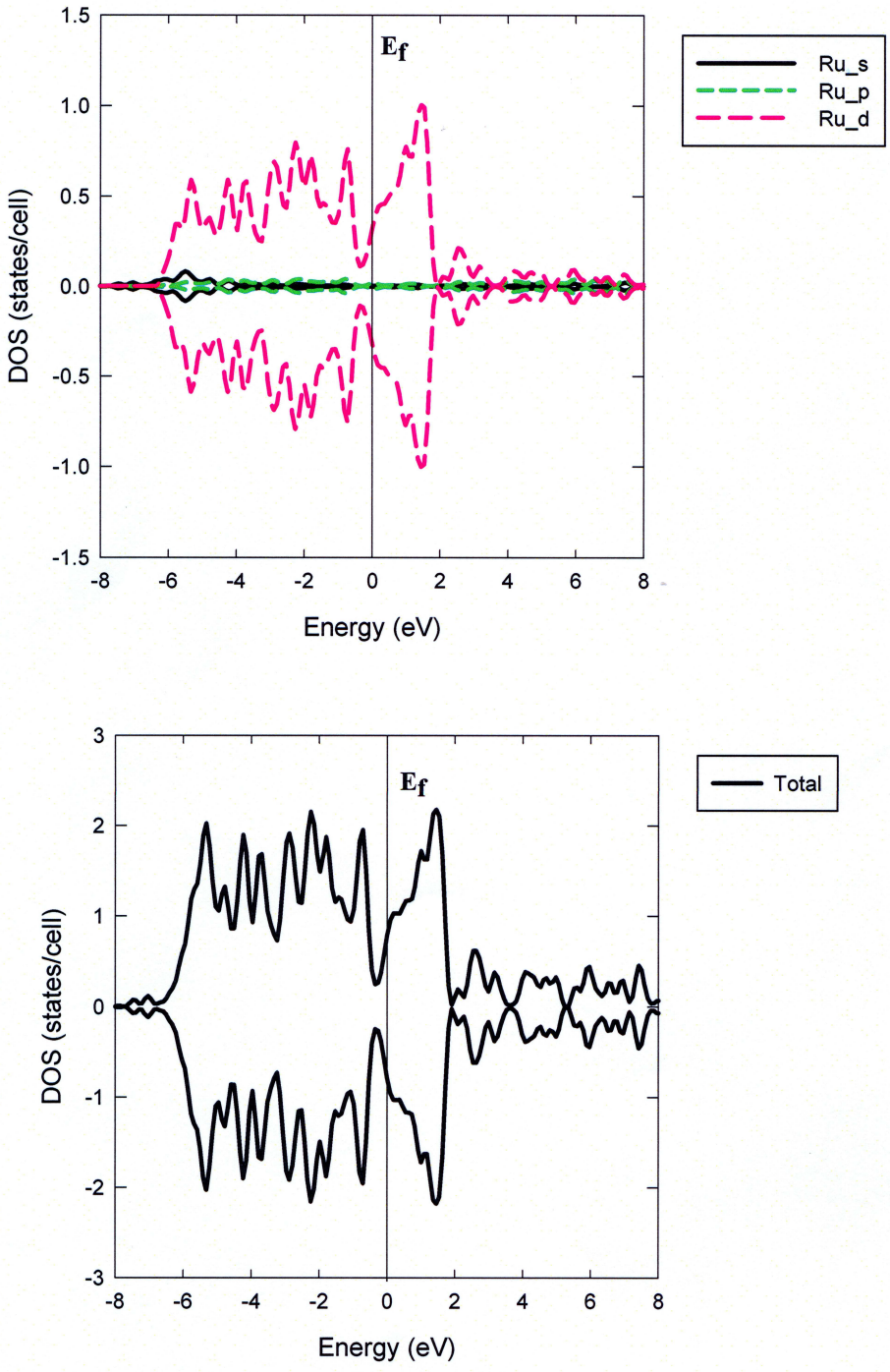

Figure 4.3: DOS of metallic Ru

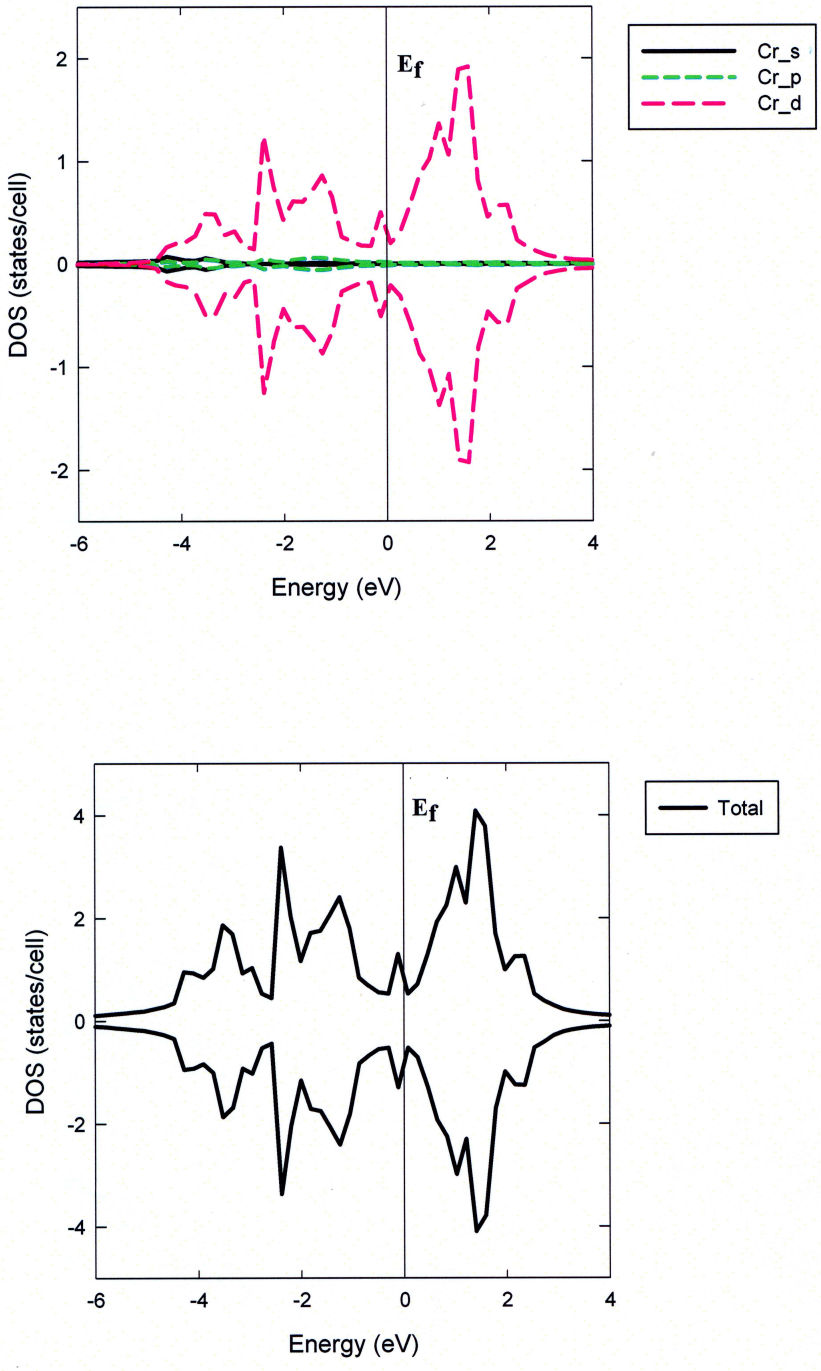

Figure 4.4: DOS of metallic Cr

eV. The high peak of the Cr 3d band is noted in the conduction band.

From the DOS of Pt_3Cr $L1_2$ phase in Figure 4.5 we note that spin-up DOS is not equal to the spin-down DOS for the total and partial DOS of Pt and Cr. More contribution to the DOS come from the d-states of both Cr and Pt. The main peaks are located at $\approx$ 1 eV and 3.5 eV for Cr and Pt respectively. In the case of Cr, the energy difference between the main peaks of the valence band and conduction band are 1.1 eV and 2.0 eV for spin-up and spin-down DOS respectively, whereas in Pt the energy difference of spin-up DOS and spin-down DOS are 3.55 eV and 4eV. The total DOS has the exact energy difference that is almost the same as in partial DOS of Pt.

In determining the stability of the system we concentrate our attention on the DOS in the vicinity of the Fermi level. For metallic Pt and Cr DOS in Figures 4.2 and 4.4, the position of the main peak DOS from the Fermi level is $\approx$ 0 and 2.2 eV, whereas for the alloy Pt_3Cr $L1_2$ structure the energy difference is about 3.5 eV. The energy difference between the main peak of valence band and that of conduction band are about 5.5 eV, 4.0 eV and 3.55 eV for metallic Pt, Cr and alloy Pt_3Cr respectively. There is a narrowing of the energy difference as we move from the metallic system to the alloy. The position of the high peak from the Fermi level shifts gradually to the lower energy side.

In Figure 4.6 we present the electronic density of states of $PtCr_3$ in the $L1_2$ structure. There is equal distribution of the spin-up and spin-down DOS. The Cr 3d band stretches from -2.2 eV to 2 eV while Pt 5d band stretches

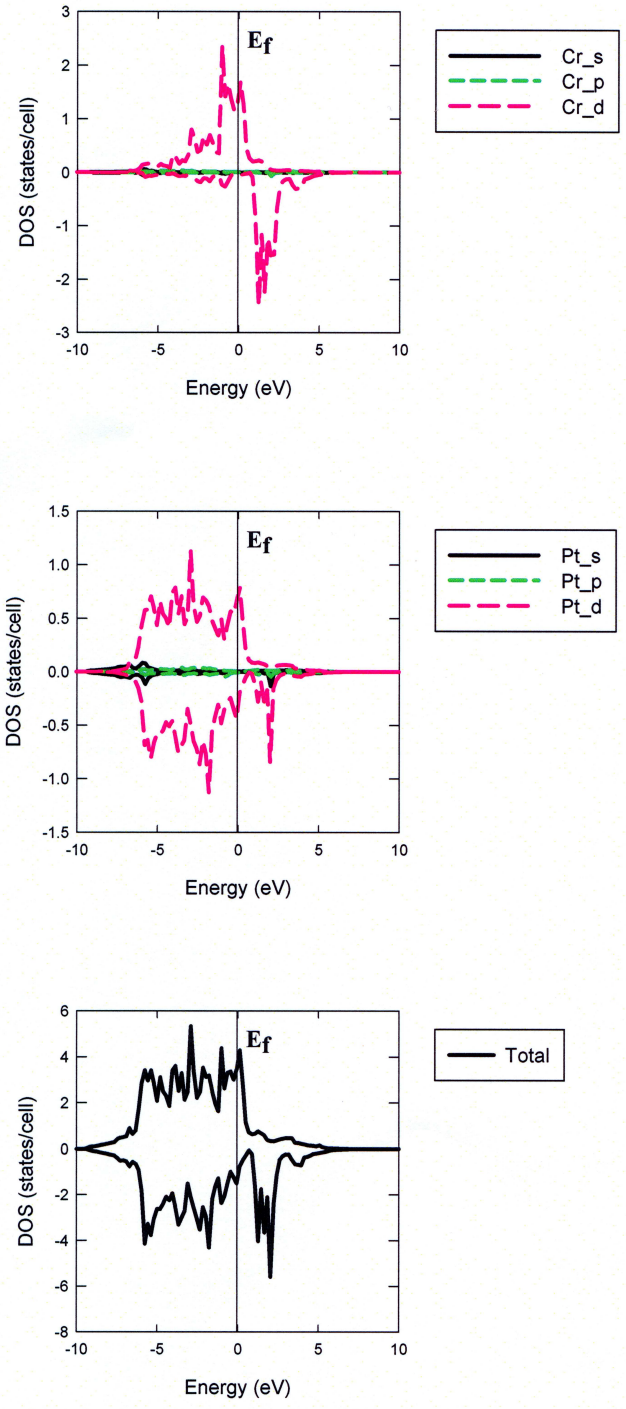

Figure 4.5: DOS of Pt_3Cr $L1_2$ structure

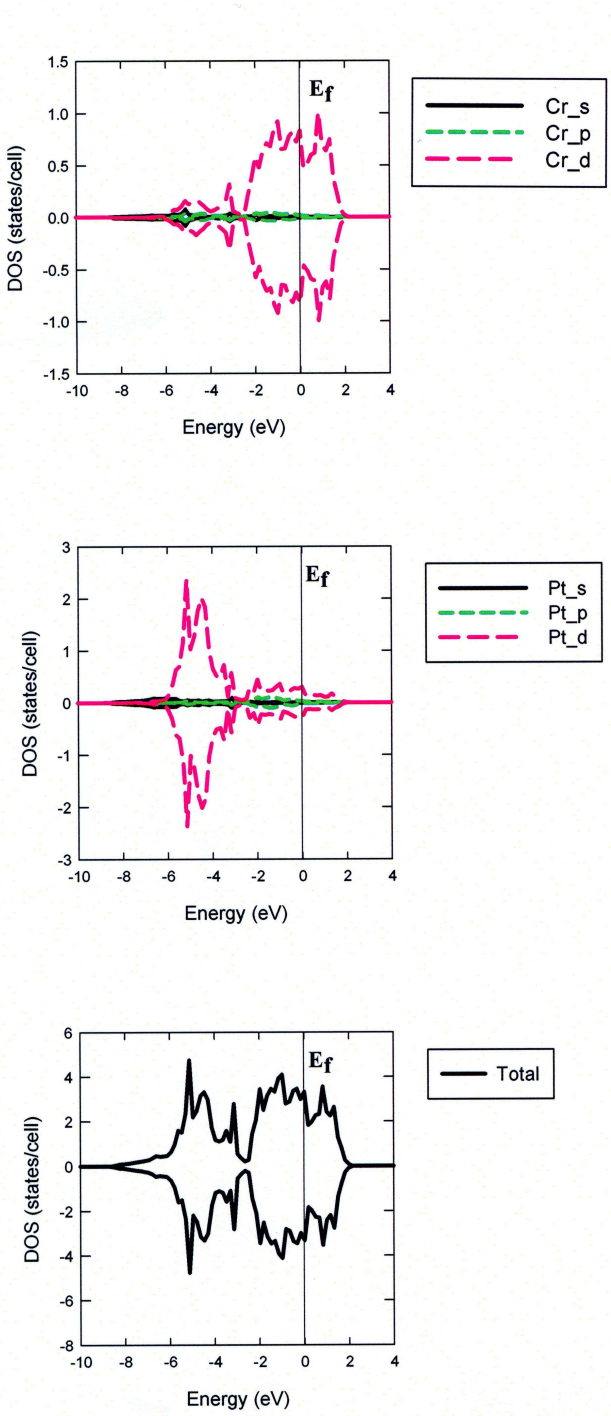

Figure 4.6: DOS of $PtCr_3$ $L1_2$ structure

from -6 eV to -3 eV. The 5d band in $PtCr_3$ $L1_2$ is narrower than in Pt_3Cr $L1_2$ structure and also in metallic Pt in Figure 4.2.

From the total DOS we note the energy difference of about 6.2 eV between the main peak in the valence band and conduction band, this value is greater than the energy difference of 3.55 eV obtained for the stable Pt_3Cr $L1_2$ structure. The broadening of the energy difference is observed by increasing the number of Cr atoms, i.e for Cr rich region.

The total and partial density of states of $PtCr_3$ A15 phase are shown in Figure 4.7. The projected spin-up and spin-down DOS are equal. Both the PDOS of Pt and Cr are dominated by the d states with less contribution from the s and p states. The s,p and d states of Pt are mainly in the conduction band. In the total DOS there is more contribution of Cr than Pt atoms. The energy difference between the main peak in valence band and conduction band is about 3.8 eV, and this value is less than the energy difference of about 6.2 eV obtained for $PtCr_3$ $L1_2$ phase. These results, together with those in Table 3.4 demonstrate that the $PtCr_3$ A15 phase is the stable structure.

Figure 4.8 shows the calculated DOS of $RuCr_3$ $L1_2$ structure, and the spin-up and spin-down DOS are equal. The behaviour is similar to the observed results of $PtCr_3$ $L1_2$ structure. The main DOS peak in the valence band is closer to the Fermi level in Cr than in Pt. The total DOS shows the energy difference of 0.5 eV from the main peak of the valence band to the Fermi level, and this value is closer to the Fermi level, hence $RuCr_3$ is reported as unstable structure.

In Figure 4.9 we show the total DOS of Ru_3Cr $L1_2$ and partial DOS of

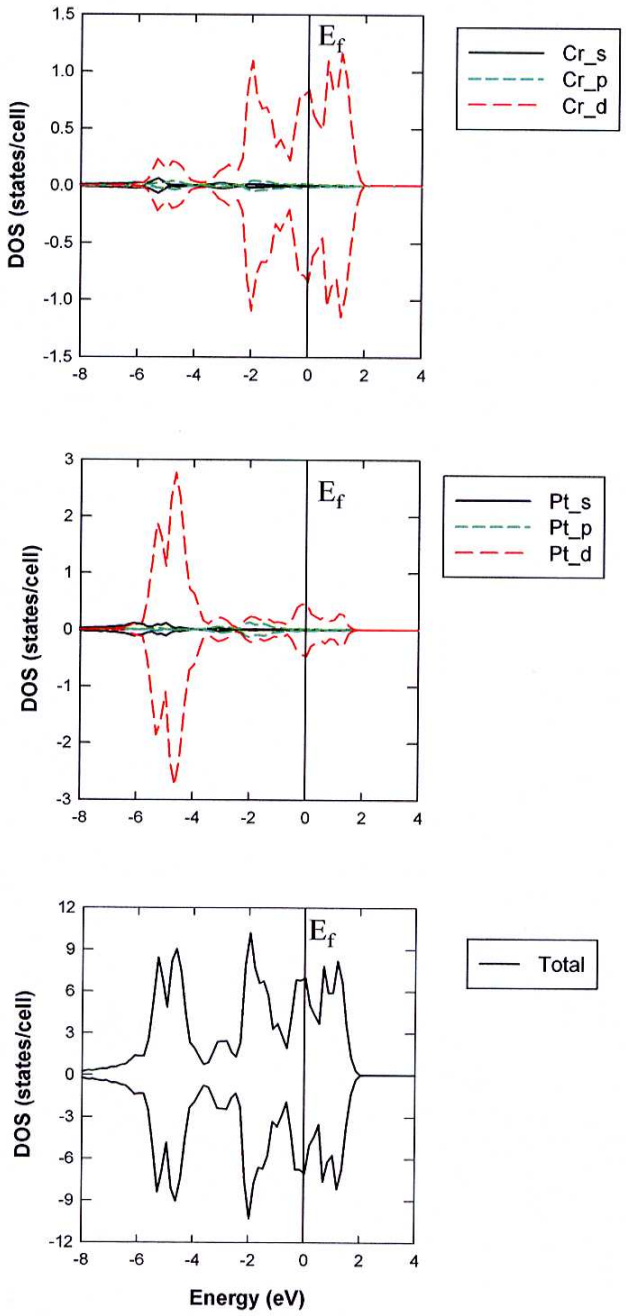

Figure 4.7: DOS of $PtCr_3$ A15 structure

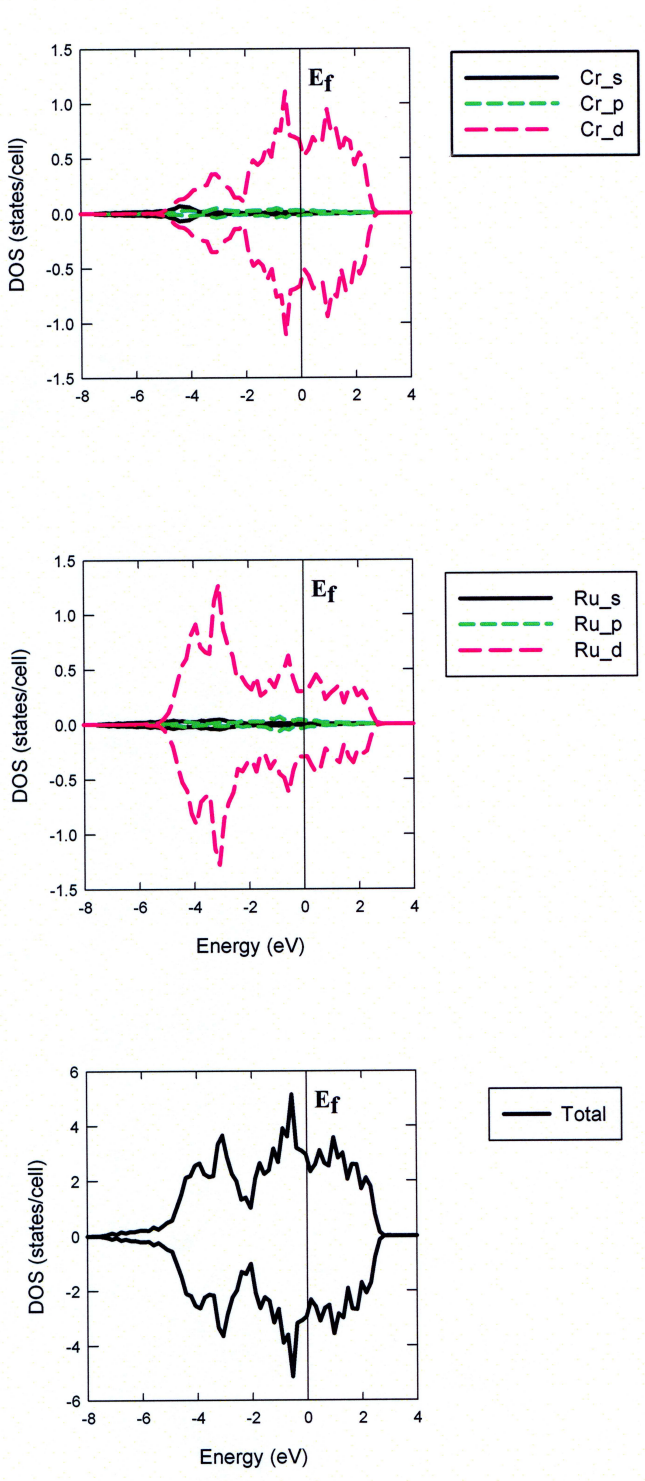

Figure 4.8: DOS of $RuCr_3$ $L1_2$ structure

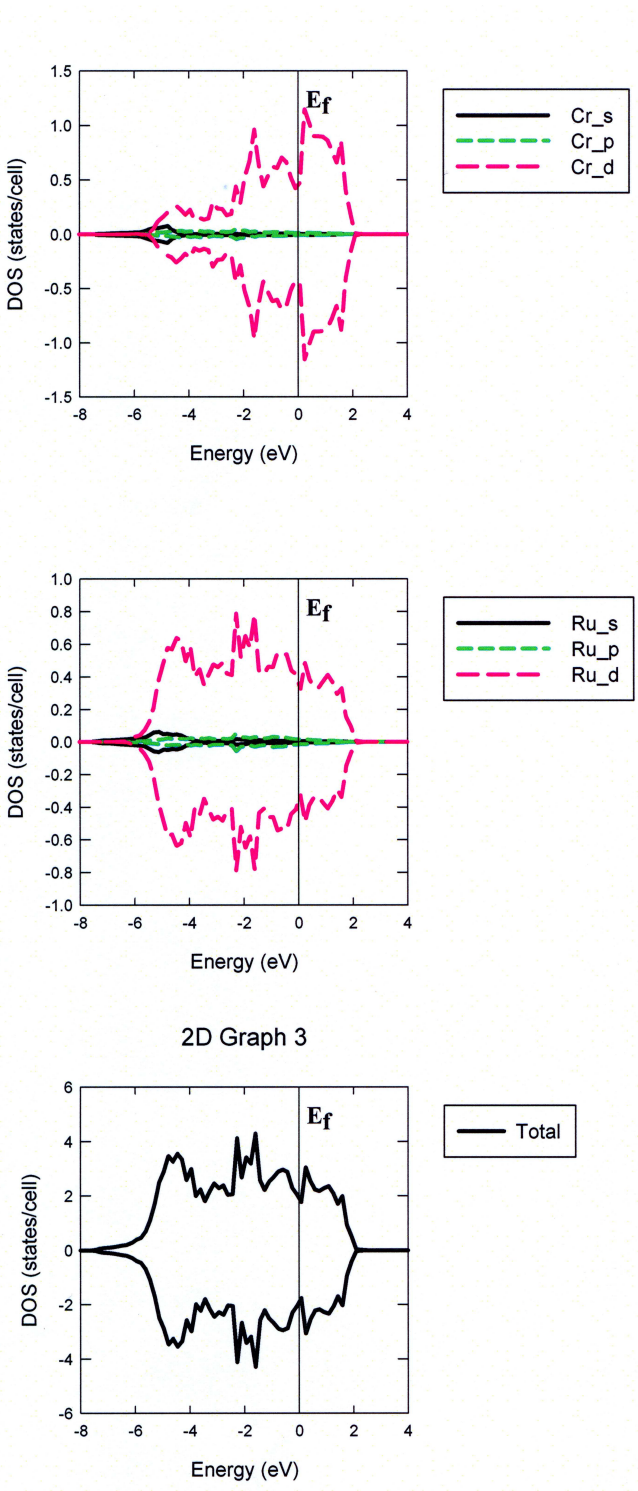

Figure 4.9: DOS of Ru_3Cr $L1_2$ structure

Ru and Cr. We observe a high peak in the conduction band whereas for Cr rich $RuCr_3$ the high peak of the PDOS of Cr was observed in the valence band. The DOS have a large dip structure at the Fermi level. Ru PDOS show less s,p and d states in the conduction band. The energy difference is larger for Ru than for Cr.

The total and partial DOS of $RuCr_3$ A15 phase are shown in Figure 4.10. The spin-up and spin-down DOS are equal. The partial DOS of Ru indicates more d states in the conduction band than in the valence band. There is a less contribution of the s and p states in both PDOS of Ru and Cr.

The DOS of PtCr B2 structure in Figure 4.11, depicts that the partial DOS of both Pt and Cr are dominated by the d-states. The contribution from the s and p states are negligible small. In the case of Cr, the up-spin DOS is mainly further from the Fermi-level while the down-spin DOS is mainly closer to the Fermi-level, hence we notice the unequal up-spin and down-spin DOS. The energy difference of the main peak of the Cr up-spin valence-band from the Fermi-level is about 1.0 eV. The partial DOS of Pt is dominated by the d states. The up-spin DOS is closer to the Fermi level as compared to the down-spin DOS.

In Figure 4.12 the 5d bands of Pt shifts to the lower energy as compared with metallic Pt, more d states are also accumulated. In Cr we observe the high PDOS in the conduction band. The spin-up and spin-down DOS are slightly different, the system can be classified as magnetic. When comparing the stability of PtCr $L1_0$ and PtCr B2 structure we considered the energy difference between the Fermi level and the main peak in the valence band.

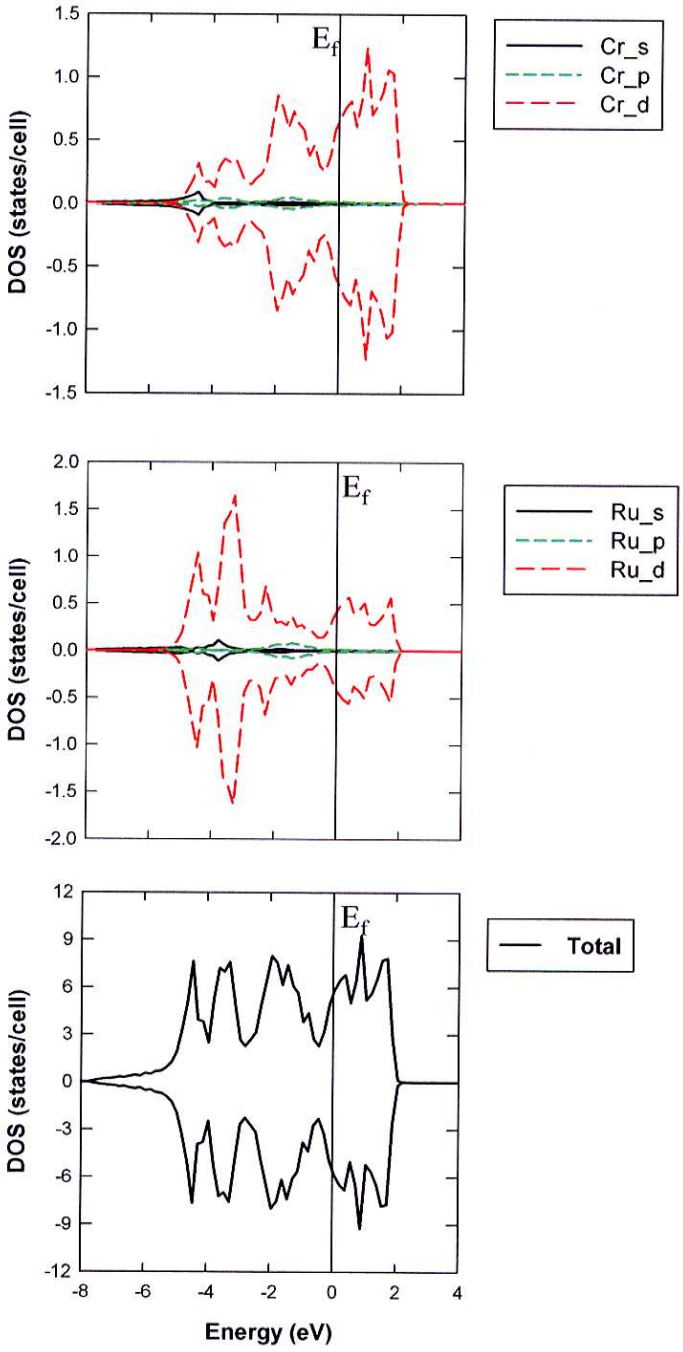

Figure 4.10: DOS of $RuCr_3$ A15 structure

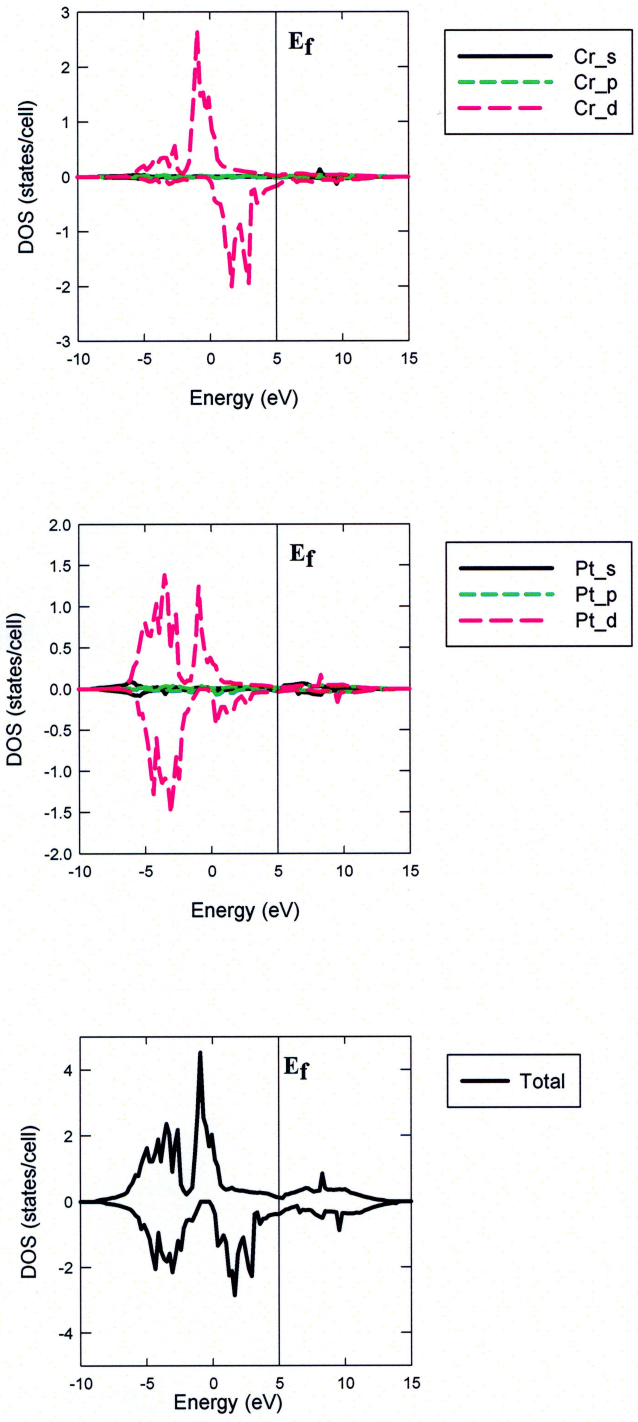

Figure 4.11: DOS of PtCr B2 structure

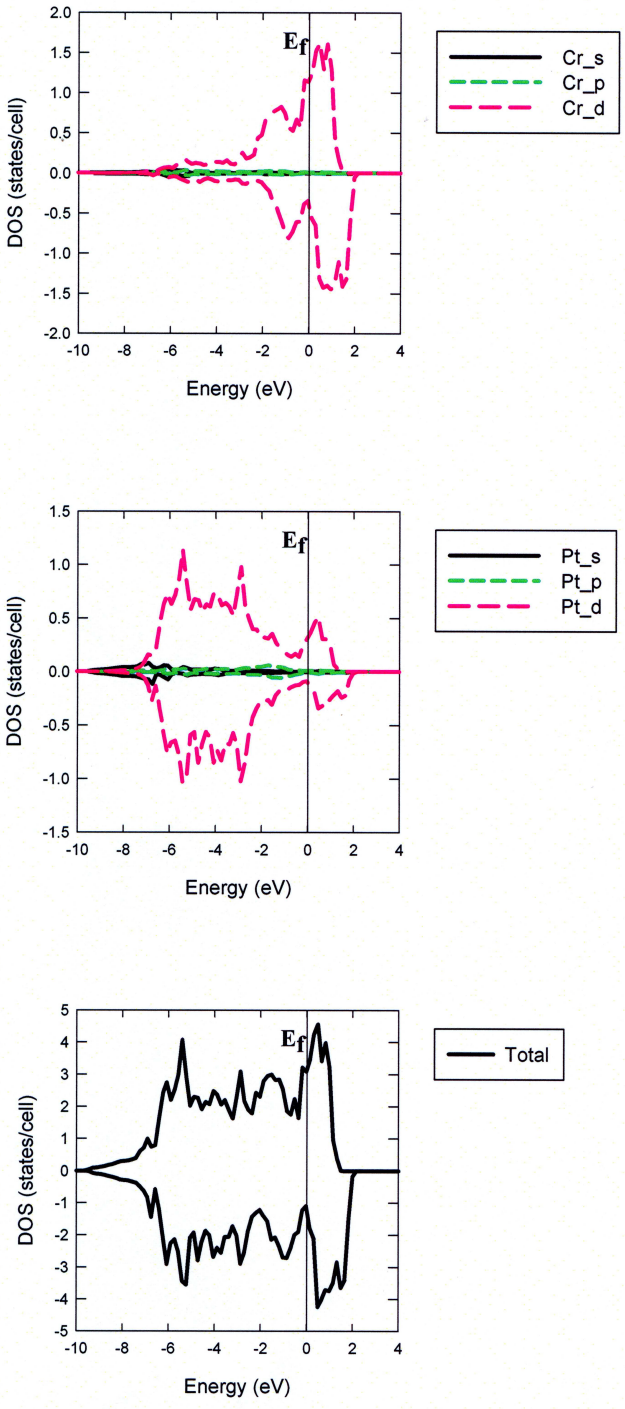

Figure 4.12: DOS of PtCr $L1_0$ structure

The calculated results were 1.0 eV and 5.6 eV for B2 and $L1_0$ structures respectively. These results prove that PtCr $L1_0$ is more stable than PtCr B2 structure.

The total of B2 RuCr and partial DOS of Cr in Figure 4.13 show the Fermi-level located at the shoulder of the strong DOS region, so the system is unstable. There are unequal spin-up and spin-down DOS. A unique behaviour is noted at the spin-down DOS in the conduction band, where a high peak is observed at this point only.

Figure 4.14 (DOS of RuCr $L1_0$) shows that the partial DOS of Cr has a high peak in the conduction band. The spin-up and spin down DOS are equal. Ru partial DOS has more d-states in the valence band than in conduction band, the d states contribution is significant compared to the s and p states. All the studied Ru-Cr show the high peak of Cr d-states in the conduction band, the only exception is the $RuCr_3$ structure which is reported to exist experimentally.

4.2 Magnetic properties of Cr

4.2.1 Introduction

The stable structure of the Pt-Cr alloys were observed, and thus far, all the studied Ru-Cr are predicted as unstable. The aim of this project is to identify the stable Ru-Cr systems, the other remarkable property that could help to find the stable structure of the Ru-Cr binary alloys is the magnetic moment of the system. That is the magnetic moment from the Ru and Cr sites. The Ru system was computed as a paramagnetic system in agreement with the

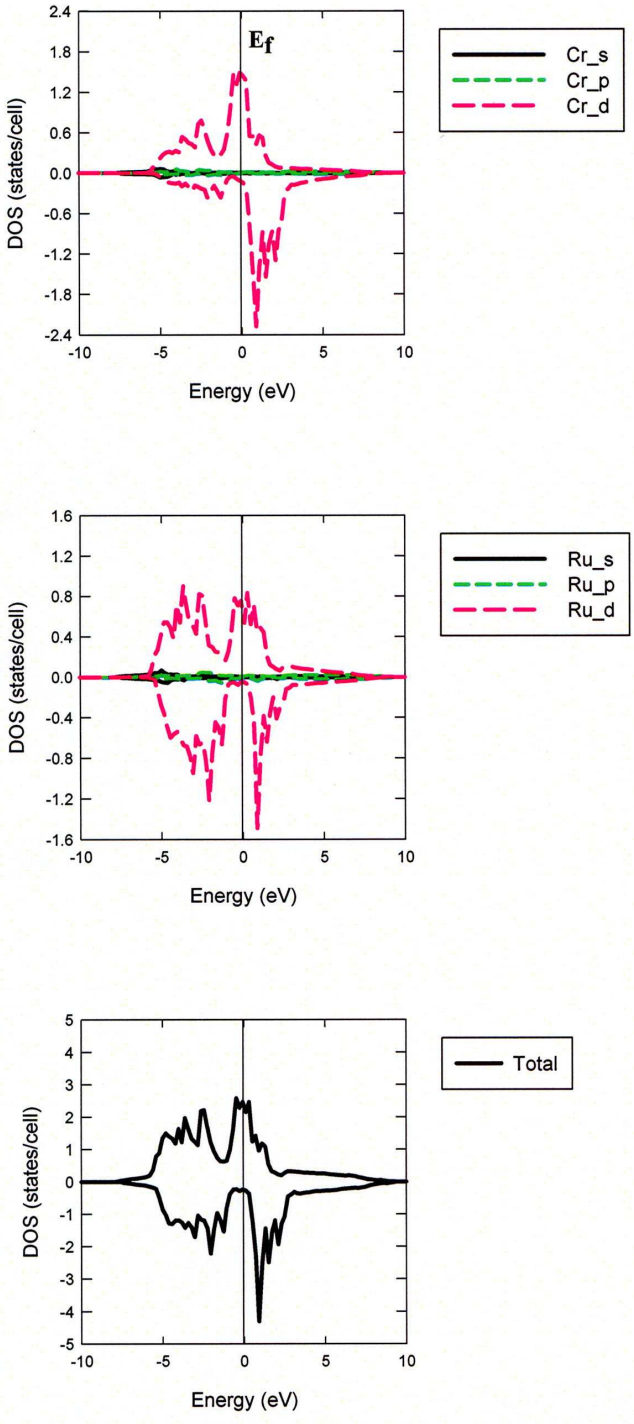

Figure 4.13: DOS of RuCr B2 structure

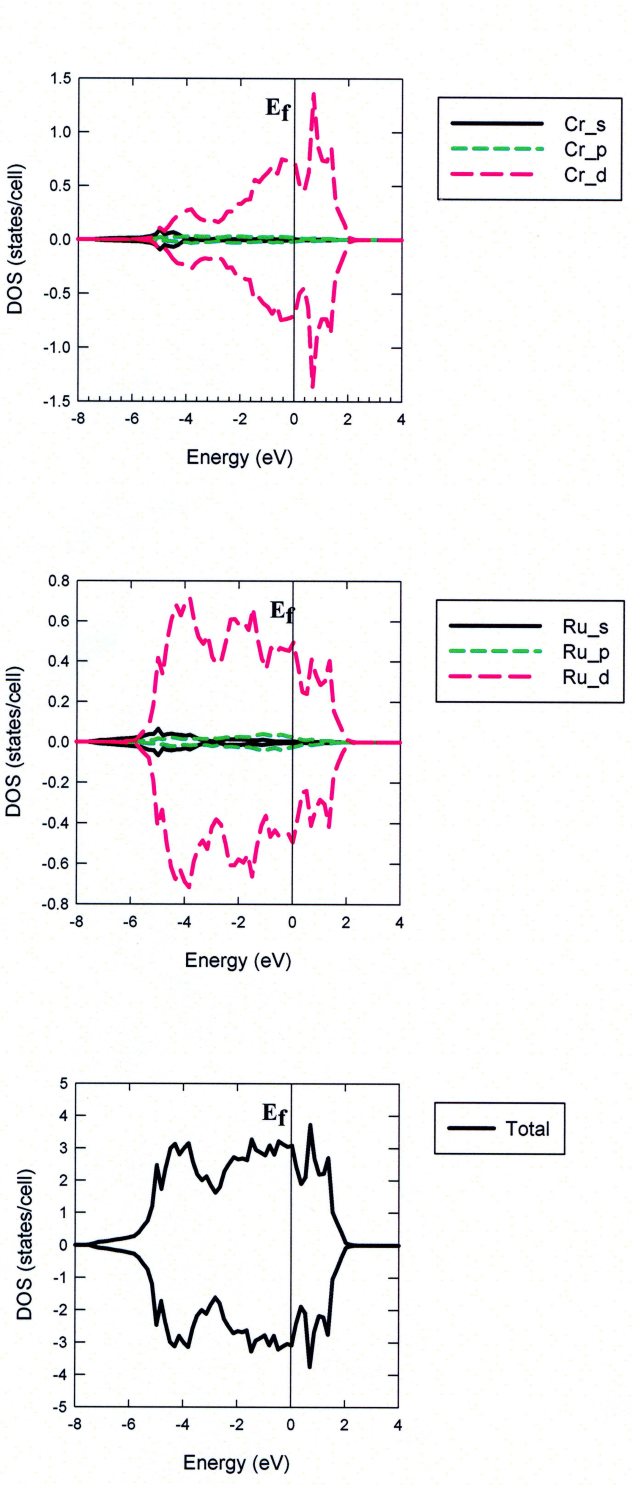

Figure 4.14: DOS of RuCr $L1_0$ structure

prevoius studies, while Cr was computed as a non-magnetic system but the recent work predicts Cr as antiferromagnetic. In this section we study the magnetic properties of metallic Cr.

4.2.2 Methodology

We performed plane-wave based, spin-polarized DFT calculations within VASP. The all electron (frozen core) Projector Augmented Wave (PAW) DFT method was employed. The GGA of Perdew, Burke and Ernzerhof (PBE) was used for the exchange-correlation functional [102]. We used the standard version of the PAW-PBE potential for Cr supplied with VASP. We used k-spacing of $0.103/\mathring{A}$ on the Cr bcc unit cell containing two atoms to obtain lattice constant and magnetic moment. Kinetic energy cut-off of 500 eV was employed. The atoms were relaxed to within a force tolerance of 0.02 eV/$\mathring{A}$ using a conjugate-gradient algorithm. In order to obtain accurate forces, the first Methfessel-Paxton method [77] was invoked for Fermi-surface smearing with a width of 0.1 eV.

4.2.3 Results and discussion

In order to clarify the role of magnetism of Cr, we performed the cell optimization for antiferromagnetic(AF) and compared it with the non-magnetic (NM) structure and calculated results are presented in chapter 3. Table 4.1 lists the computed lattice parameters for NM and AF chromium, together with the data from the previous theoretical studies and experiments.

The predicted equilibrium lattice constant for the AF bcc Cr is $2.870\mathring{A}$,

Table 4.1: The lattice constants (a) and magnetic moment(m) of the AF and NM Cr

Method		State	a($\AA$)	m μB	Reference
GGA	PBE-VASP	AF	2.870	1.07	This work
	PBE-VASP	NM	2.851	0	This work
	PAW	AF	2.855	1.09	ref[101]
		AF	2.849	1.19	ref[103]
	LAPW	NM	2.850	0	ref[104]
	FLAPW	AF	2.871	1.08	ref[105]
	Expt		2.879		ref[105]
LSDA	PAW	AF	2.778	0.67	ref[103]
	LAPW	NM	2.793	0	ref[106]
	ASW	AF	2.854	0.71	ref[107]

this value agrees well with all-electron DFT-FLAPW-GGA lattice constant of 2.871 $\AA$. Our NM lattice constant has a value of 2.851 $\AA$, which is in good agreement with the NM LAPW, AF PAW and LSDA ASW results which are given as 2.850 $\AA$, 2.855 $\AA$ and 2.854 $\AA$ respectively. We note that the AF lattice constant lies closer to the experimental value than the calculated NM lattice constant. The computed heats of formation of the AF and NM Cr are -0.06 kJ/mol and 1.25 kJ/mol respectively, so AF Cr is predicted to be more stable than NM. Our AF Cr has has a magnetic moment of 1.07μB, we see a very good agreement between our results and AF FLAPW magnetic moment of 1.08 μB, and also AF PAW value of 1.09 μB.

Chapter 5

Phonons and thermal expansion

5.1 Phonons

5.1.1 Introduction

The study of phonons is an important part of solid state physics, since phonons play a major role in many physical properties of the solids, including a material's thermal conductivity. In particular, the properties of long-wavelength phonons give rise to sound in solids. Phonons are a quantum mechanical version of a special type of vibrational motion, known as normal modes in classical mechanics, in which each part of a lattice oscillates with the same frequency. The normal modes are the elementary vibrations of the lattice.

The phonon spectrum of different phases of Pt_3Cr, $PtCr_3$, PtCr and $RuCr_3$ A15 phase were investigated by the VASP code that allow inter-atomic forces to be calculated. We used the PHONON code of Parlinski [108] interfaced to VASP, which allows phonons, thermodynamic properties such as

lattice specific heat, vibration energy and free energy to be calculated.

PHONON is a software for calculating the dispersion curves, and phonon density spectra of crystals from either a set of force constants, or from a set of Hellmann-Feyman forces [78] computed within an ab initio program which optimizes the structure of the crystalline supercell within constraints imposed by a crystallographic space group. We used the direct method [108, 109, 110] where the force constants are calculated from Hellman-Feyman forces.

In this chapter, we will compare the phonon stability of different phases of Pt_3Cr, $PtCr_3$ and PtCr binary alloy at 0 GPa. Furthermore, we will investigate the phonon spectra of $RuCr_3$ A15 phase. The total and partial phonon density of states for different phases of Pt_3Cr, $PtCr_3$, PtCr and $RuCr_3$ will be presented. Lastly we analyse the thermal expansion results of Pt_3Cr and $PtCr_3$ binary alloys.

5.1.2 Methodology

Density functional theory is applied to study the behaviour of the phonons in Pt_3Cr, $PtCr_3$, PtCr and $RuCr_3$ with a plane-wave pseudopotential method as implemented in the VASP code. The generalized gradient approximation (GGA) is used with the Perdew and Wang's [102] form of the exchange-correlation interactions. The unit cell structure entered should already have been optimized by VASP. System is represented by a supercell of 2x2x2 with periodic boundary conditions. The Hellmann-Feyman forces necessary to evaluate the force constants and the dynamical matrix were obtained from calculations performed by VASP within generalized gradient approximation

(parametrized by PBE scheme).

The projected augmented wave (PAW) pseudopotentials and the plane wave basis set expanded up to the cut-off energy of 500 eV were employed to treat the valence states. The first Brillouin zone were sampled wihin a 5x5x5 and 7x7x5 Monkhorst-Pack k-mesh scheme for (B2, $L1_2$, $L1_0$ and A15) and (tP16, DO_C and DO'_C) phases respectively. We have used the supercell diameter of 7 Å to obtain the reliable phonon dispersion relations.

Periodic boundary conditions were imposed. Selected atoms were displaced at 0.05 Å away from their equilibrium positions, and the corresponding interatomic forces were calculated and then force constants were obtained. Using these force constants, the phonon frequencies were obtained by straightforward diagonalization of the dynamical matrix. The phonon dispersion curves were calculated along several high symmetry directions in the BZ.

5.1.3 Phonon DOS and dispersion curves of Pt_3Cr phases at O GPa

In Figure 5.1. we present the calculated phonon DOS and phonon spectra for different phases of Pt_3Cr at zero pressure along the high symmetry directions of the Brillouin zone. In the 1D lattice, the atoms are restricted to move along the x direction, so all the phonons correspond to longitudinal waves, whereas in 3D, vibration is not restricted to the direction of propagation, it also occurs in the perpendicular plane; the 3D phonons also correspond to transverse waves. The dispersion relations exhibit two types of phonons,

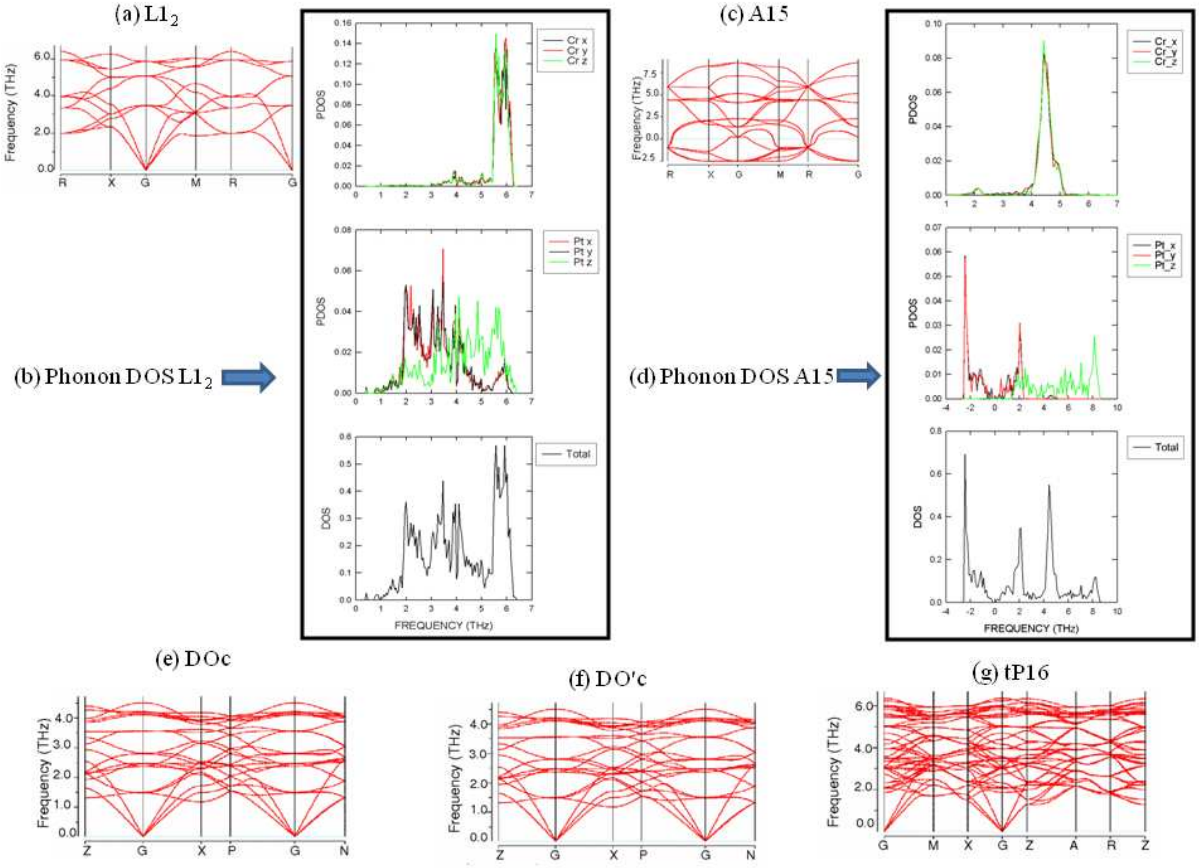

Figure 5.1: Phonon DOS and dispersion curves of Pt_3Cr phases at 0 pressure

the optical and acoustic modes corresponding to the upper and lower sets of curves in the diagram, respectively.

Figure 5.1 (a) shows the longitudinal and transverse acoustic and optical phonons which indicates a total of 12 phonon branches. Pt_3Cr $L1_2$ contains four atoms (N = 4) per unit cell, so there are 3 acoustical branches (1 longitudinal and 2 transverse) shown at the lower part of the phonon dispersion curve, and 3N - 3 = 9 optical branches (N-1 = 3 longitudinal and 2N - 2 = 6 transverse). The frequencies of optical phonons start at about 2 THz. In addition to the phonon dispersion curves of Pt_3Cr phases we have calculated the density of states. For the completeness of the lattice dynamics we show, in Figure 5.1 (b), the total and partial phonon density of states of Pt and Cr in the Pt_3Cr $L1_2$ phase. We observed exceptionally low density of states of Cr atoms below 5.2 THz, whereas for Pt atoms high DOS was detected below and above 5.2 THz.

The Pt and Cr atoms vibrate in modes of different frequencies. Pt atoms vibrate preferentially at lower frequencies; all DOS of states start at approximately 0.3 THz and vanish below 6.3 THz. The partial density of states of Cr has a very low intensity below 5.2 THz. This means that in this region the acoustic modes of Cr contribute very little to the phonon density of states. In the total DOS, modes below 5.2 THz mainly emanate from vibrations of Pt atoms. The vibrations of both Pt and Cr atoms contribute to the modes between 5.2 THz and 6.3 THz.

The calculated phonon dispersion for A15 Pt_3Cr are predicted in Figure 5.1 (c). We have found the soft modes at X, G and M-points of the Brillouin

zone. We have observed another soft mode at R point, but the soft mode frequency is about $i1$ THz which is higher than the frequencies of modes arising from the X, G and M points. The R mode is expected not to cause any effect.

For convenience, we use the negative y-axis to plot the imaginary branches of spectra. From Figure 5.1 (c), one can conclude that the A15 Pt_3Cr is unstable, owing to the appearance of imaginary phonons. This structure has a slightly higher maximal optic phonon frequency of 7.5 Hz. Comparing phonon dispersion for Pt_3Cr $L1_2$ and A15 phases in Figures 5.1 (a) and (c) respectively, it has turned out that the $L1_2$ phase is vibrationally stable, whereas the A15 phase is unstable.

Figure 5.1 (d) shows DOS of the A15 Pt_3Cr phase and we observe a low DOS of Cr atoms below 4.0 THz, and a high DOS between 4.0 THz and 5.0 THz. Cr DOS starts at 1.8 THz and ends at 5.2 THz. Negative frequencies appear in the PDOS of Pt atoms and this interesting feature is detected up to -2.4 THz. This different profile of frequency distribution indicates the origin of dynamic instability in the Pt_3Cr A15 phase. From the previous statements we conclude that the soft modes shown in the phonon dispersion curve of the A15 Pt_3Cr are attributed to the Pt atoms. From the total DOS of Pt_3Cr that appears in the ranges 0.3 THz to 6.3 THz and -2.4 THz to 8.3 THz for the $L1_2$ and A15 respectively, it is apparent that the $L1_2$ Pt_3Cr phase is the most stable in agreement with the results of the phonon dispersion curves.

In Figure 5.1 (e) the DO_C acoustic and optical phonons are consistent with the DO_c' results indicated in Figure 5.1 (f). The frequencies and the

Brillouin zone are clearly described. The dispersion curves do not show too complicated features; there are no imaginary phonons detected in these two studied phases. The frequencies of optical phonons start at about 1.5 THz. The frequencies of $L1_2$ optical phonons in Figure 5.1 (a) start at about 2 THz, which is higher than the frequency observed in DO_c and DO'_c.

The phonon dispersion curves of Pt_3Cr tP16 phase are predicted and shown in Figure 5.1 (g). There are more phonon branches in the tP16 phase than in all studied phases of Pt_3Cr. The phonon branches of tP16 Pt_3Cr starts at a frequency of ≈ 0 THz, and there are no imaginary phonons. It is apparent that the frequency of the acoustic branches of the $L1_2$ phase is relatively higher as compared with all the studied Pt_3Cr phases, hence the $L1_2$ is predicted as the most stable phase, in agreement with the previous results discussed in Chapter 4.

5.1.4 Phonon DOS and dispersion curves of the $PtCr_3$ phases at 0 GPa

Figure 5.2 shows the calculated phonon DOS and dispersion curves of $PtCr_3$ phases at 0 GPa. Figure 5.2 (a) shows that the phonon spectra of the $L1_2$ $PtCr_3$ has soft modes at points M and R of the Brillouin zone. There is a high density of unstable modes in the region of the M point. The corresponding phonon DOS of $PtCr_3$ $L1_2$ is shown in Figure 5.2 (b), where PDOS shows Cr atoms vibrating at lower frequencies (below 0 THz). Pt atoms vibrate at frequencies greater than 0 THz. It is evident that Cr atoms are responsible for the soft modes observed at points M and R in Figure 5.2 (a).

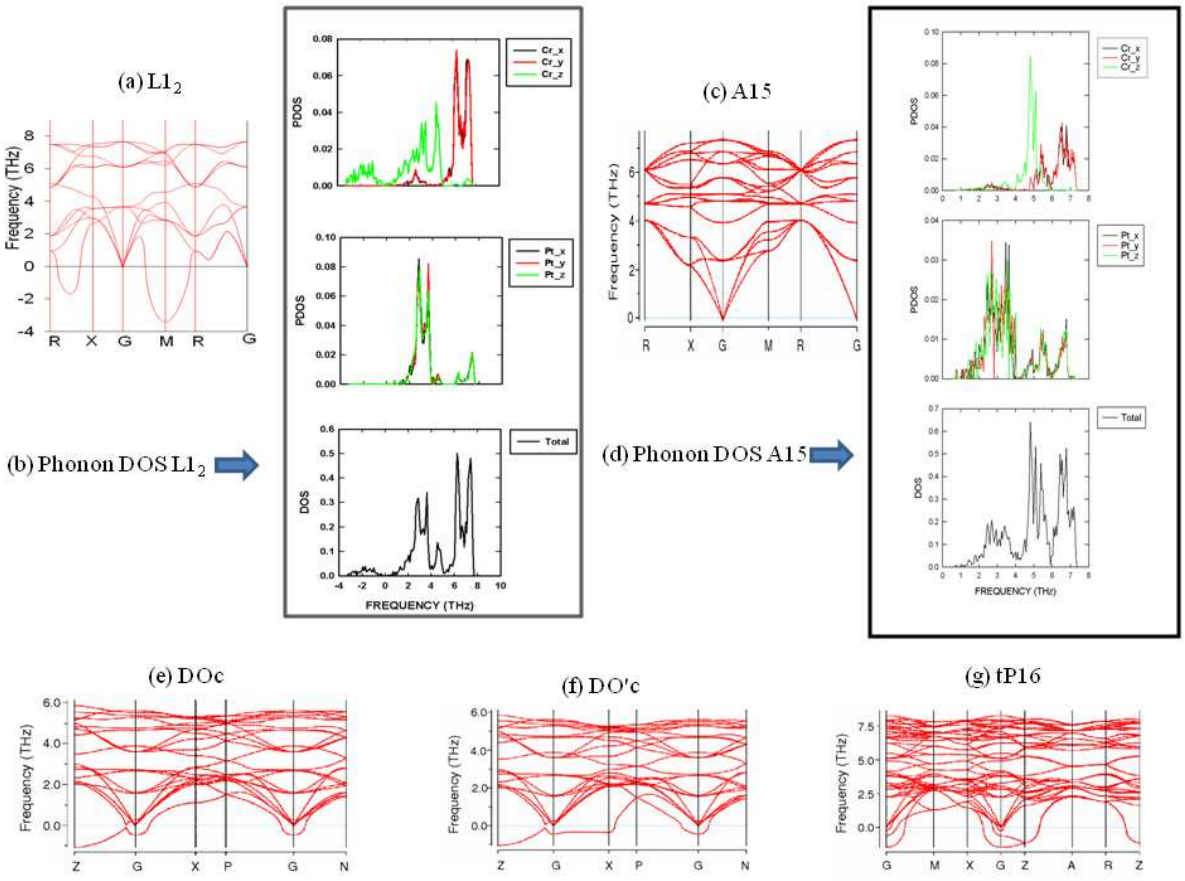

Figure 5.2: Phonon DOS and dispersion curve of $PtCr_3$ phases at 0 pressure

Both the phonon spectra and phonon DOS predicts $PtCr_3$ $L1_2$ to be unstable.

We also computed the phonon dispersion curve of the A15 $PtCr_3$ for comparison with the $L1_2$ $PtCr_3$ phase. Figure 5.2 (c) depicts the A15 $PtCr_3$ acoustic branches which start at a frequency of 4Hz, and there are no soft modes for the A15 structure. In comparison of the dispersion curves, it is apparent that the $PtCr_3$ A15 phase is stable while the $L1_2$ is unstable.

In Figure 5.2 (d) we show the total and PDOS of A15 $PtCr_3$ phase, as in the A15 Pt_3Cr we observe the low DOS of Cr below 4 THz. Pt DOS starts at 0.8 THz and ends at 7.3 THz. No negative frequencies are detected in the PDOS of the A15 phase as compared to the $L1_2$ phase in Figure 5.1 (b). For comparison, we also calculated the phonon DOS of $PtCr_3$ DO_C and tP16 phases, and the results indicated the existence of negative frequencies. From this results we can conclude that A15 phase is dynamically stable while other studied phases are unstable.

The phonon spectra of the DO_C and DO'_C are shown in Figures 5.2 (e) and (f) respectively, the results are generally similar but differ at X. For DO_C $PtCr_3$ we detected the soft modes at Z and G points of the Brillouin zone, whereas DO'_C soft modes were found at three points G,X and Z points of the Brillouin zone. The phonon spectra of tP16 $PtCr_3$ show the soft modes at G and Z points of the Brillouin zone. It is evident that the $L1_2$, DO_C, DO'_C, an tP16 phases are vibrationally unstable, whereas A15 structure is vibrationally stable.

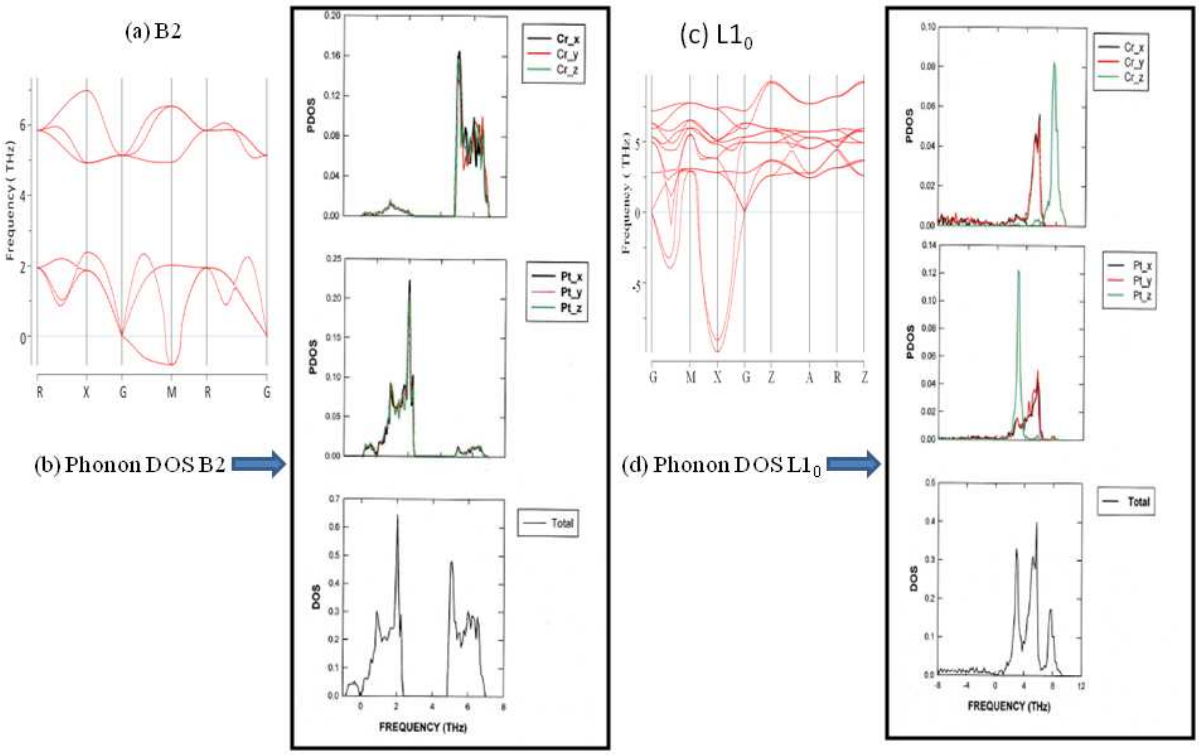

Figure 5.3: Phonon DOS and dispersion curve of PtCr B2 and $L1_0$ at 0 pressure

5.1.5 Phonon DOS and dispersion curves of the PtCr B2 and $L1_0$ phases at 0 GPa

In Figure 5.3 we present the phonon DOS and dispersion curves of PtCr B2 and $L1_0$ phases. The phonon dispersion of PtCr B2 phase is presented in Figure 5.3 (a), and the soft modes have been detected at G and M points of the Brillouin zone. These results demonstrate that PtCr B2 is dynamically

unstable.

The partial DOS of Pt and Cr in PtCr B2 phase in Figure 5.3 (b) depicts that Pt vibrates at lower frequencies while Cr vibrates at higher frequencies. The sum of Cr density of states Cr_x + Cr_y + Cr_z fits the total density of states above 5.0 THz. The part above the gap is mainly due to vibrations of Cr atoms, while the part below the gap is contributed by Pt atoms. PtCr B2 is an interesting lattice in which Pt atoms form a frame for acoustic modes, and the Cr atoms vibrate within the optical modes.

The results of PtCr $L1_0$ in Figure 5.3 (c) show that motions within acoustic dispersion curves are almost entirely due to the Cr atoms. For PtCr $L1_0$ phase, the unstable phonon modes appear in a smaller part of the Brillouin zone. Significant softening occurs in the lower transverse acoustic branch, and soft modes are attributed to Pt atoms.

These results demonstrate that PtCr $L1_0$ is also dynamically unstable, the difference is that the soft mode frequencies of $L1_0$ phase are more pronounced than those of the B2 phase. The frequency of a given lattice vibration depends on the stiffness of the lattice (elastic moduli). The calculated C_{44}s of $L1_0$ and B2 with values of 178.3 GPa and 118.0 GPa respectively confirms the relationship between the phonon frequency and elastic constants. The relation between the frequency of phonon modes and the elastic constant C_{44} is found to be reasonably valid for PtCr phases.

Figure 5.3 (d) shows the total and partial DOS of PtCr $L1_0$ phase, and it can be deduced that vibrations below 4 THz emanate from Pt atoms, and the vibrations above 4 THz are mainly associated with Cr atoms.

5.1.6 Phonon DOS and dispersion curves of the $RuCr_3$ A15 phase at 0 GPa

Figure 5.4 presents the phonon DOS and dispersion curve of $RuCr_3$ A15 phase. In Figure 5.4 (a) there are no soft modes detected at any point of the Brillouin zone, indicating that $RuCr_3$ A15 phase is dynamically stable. However, the results in chapter 3 predicted $RuCr_3$ A15 phase as thermodynamically unstable though the positive heat of formation, 0.0796 eV, is close to zero. Both findings give an interesting question about the stability of $RuCr_3$ A15 phase. The phonon dispersion results can be linked with the experimental work which indicated that $RuCr_3$ A15 phase is stable at higher temperature. From our results and experimental findings, we assume that $RuCr_3$ A15 phase can be observed as thermodynamically stable if more tests can be done on the system.

We have calculated the phonon DOS and partial phonon DOS for $RuCr_3$ A15 phase as shown in Figure 5.4 (b). The curves show that motion within acoustic dispersion curves are predominantly due to Ru. The motion within optical dispersion curves originate from both Ru and Cr.

5.2 Thermal expansion

5.2.1 Introduction

There has been a growing interest in the thermal expansion of solids. Thermal expansion gives information about the temperature dependence of the lattice vibrational frequencies [111, 112]. Free energy calculations were perfomed in the framework of the frozen core all-electron projector augmented wave

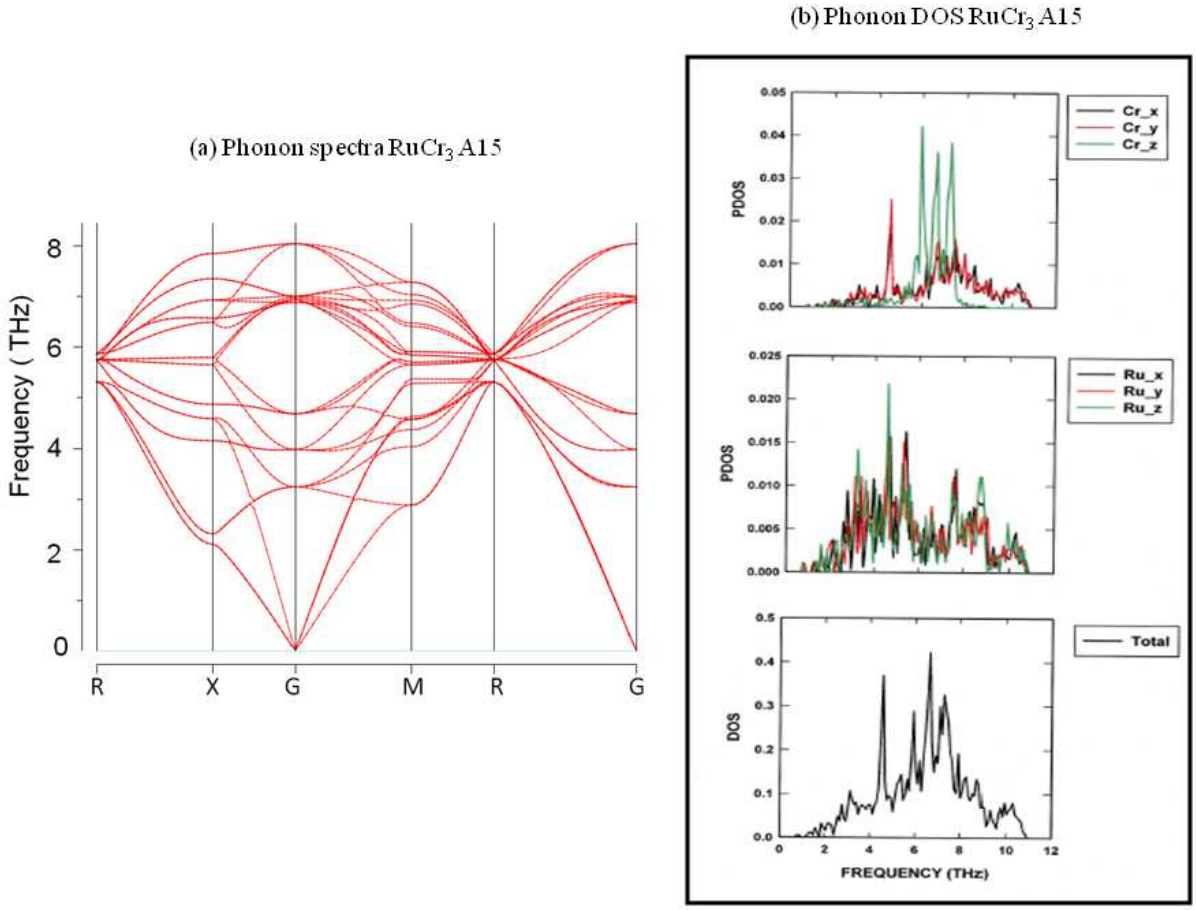

Figure 5.4: Phonon DOS and dispersion curve of the A15 $RuCr_3$ phase at 0 pressure

(PAW) [48] . To evaluate the free energy as a function of the temperature, the phonon frequencies must be first calculated for each lattice constant. Free energy can be used to study thermal properties and thermodynamical parameters of the crystals.

The phonon dispersion calculations were performed at a number of electronic temperatures up to 500 K. The free energy was calculated as the sum of the electronic and vibrational contributions. For ordered solids, the free energy at finite temperature has contributions from both the lattice vibrations and the thermal excitations of electrons [113]. Our aim is to investigate the temperature dependence of the lattice vibrational frequencies. We calculated the total free energy at different temperatures and for each temperature we fitted the polynomial.

5.2.2 Results and Discussion

We determine the lattice constants and the thermal expansion of Pt_3Cr $L1_2$ phase in the temperature range 0 - 500 K. The lattice constant (a) of 3.920 Å (and experimental value is 3.873 Å) was obtained for the Pt_3Cr $L1_2$ phase. In Figure 5.5, we plot the dependence of the free energy on the lattice constant in the temperature range 0 - 500 K. The change of the minimum position of the free energy curve directly determines the thermal expansion of the Pt_3Cr $L1_2$ phase.

In Figure 5.5, we note that the minimum of each curve shifts to larger lattice constants when the temperature increases. The points of minimum free energy are connected by a vertical solid line. The minimum lattice

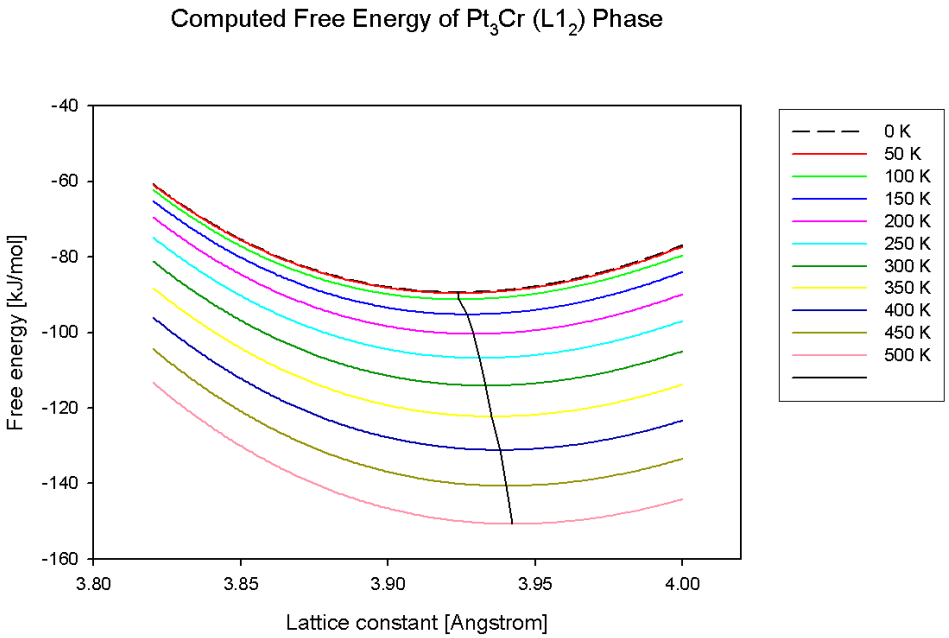

Figure 5.5: Lattice constant dependence of the free energy ($L1_2$ Pt_3Cr) for several temperatures. Vertical solid line connects points of the minimum of free energy

Table 5.1: Lattice constants a (from polynomial fit) at various temperatures for Pt_3Cr $L1_2$ phase

T (K)	a ($\AA$)
0	3.923
50	3.924
100	3.924
150	3.927
200	3.929
250	3.931
300	3.933
350	3.935
400	3.938
450	3.940
500	3.942

constant was evaluated accurately using the polynomial fit. Lattice constants obtained for each temperature are listed in Table 5.1, and they range from 3.933 Å at room temperature to 3.942 Å at 500 K. The thermal expansion of the Pt_3Cr $L1_2$ phase was determined at different temperatures using the following equation

$$\frac{\Delta l}{l} = \frac{a_T - a_{300}}{a_{300}} \tag{5.1}$$

where a_T is the lattice constant at a given temperature and a_{300} at room temperature. The thermal expansion as a function of temperature is plotted in Figure 5.6, and it increases linearly with temperature.

We have also calculated the thermal parameter α as a function of T, which is defined as

$$\alpha(T) = \frac{1}{a}\frac{\delta a}{\delta T} \tag{5.2}$$

The values of $\alpha(T)$ are presented in Table 5.2, and it is inversely propor-

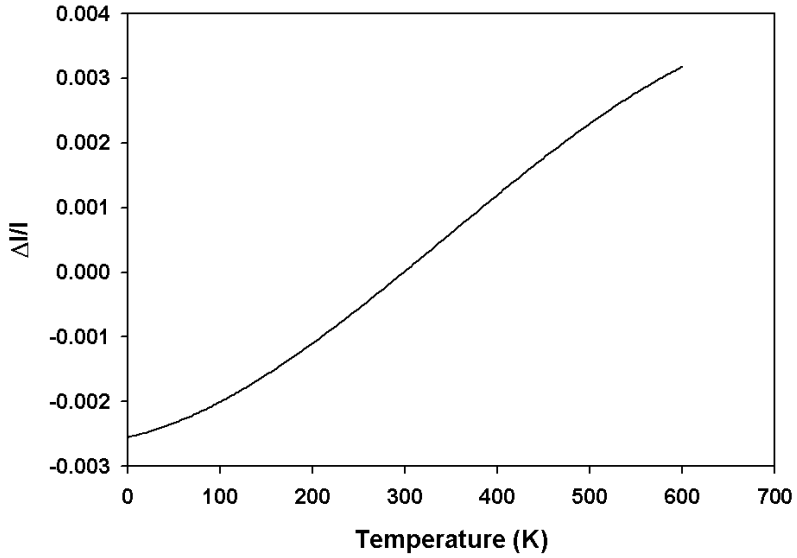

Figure 5.6: Thermal lattice expansion as a function of temperature for Pt_3Cr $L1_2$ phase

Table 5.2: Temperature dependance of thermal expansion $\alpha(T)$ for Pt_3Cr $L1_2$ phase

T (K)	$\alpha(T)$ $(10^{-6})K^{-1}$
100	15.29
150	10.18
200	10.18
250	10.17
300	10.17
400	10.15
450	10.15

tional to temperature.

We have also determined the free energy vs lattice constant for the Pt_3Cr A15 phase and the curve is presented in Figure 5.7. The lattice constant reduces from 4.989 Å to 4.987 Å. In the case of the Pt_3Cr A15 phase, the minimum of each curve shifts to a lower lattice constant as temperature increases, this behaviour can be attributed to the soft modes in Figure 5.1 (c). In general we observe an opposite trend in A15 and $L1_2$ curves, where the minimum shifts to higher lattice constants.

The thermal expansion is plotted as a function of temperature in Figure 5.8 for Pt_3Cr A15 phase. The thermal expansion increases linearly with an increasing temperature.

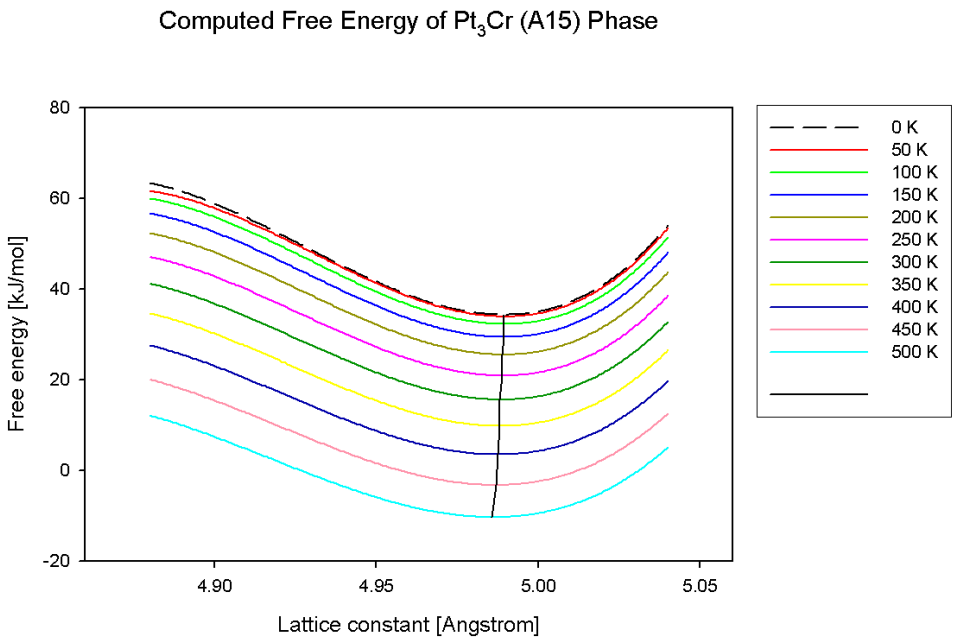

Figure 5.7: Pt_3Cr A15 lattice constant dependence of free energy for several temperatures. Vertical solid line connects points of the minimum of free energy

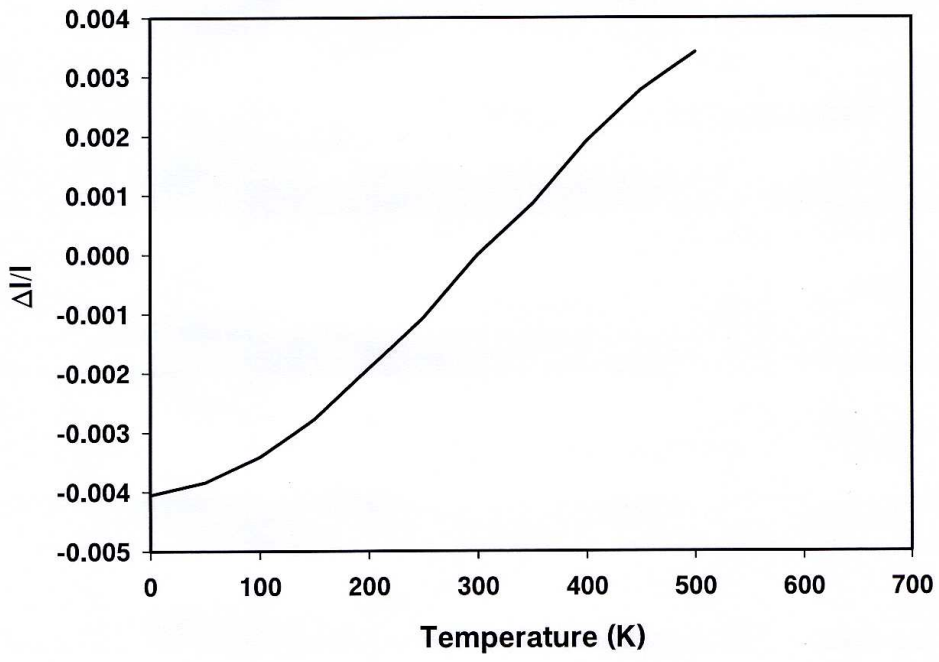

Figure 5.8: Thermal lattice expansion as a function of temperature for Pt_3Cr A15 phase

Chapter 6

Conclusions and recommendations

6.1 Conclusions

Structural investigations of Pt, Cr, Ru and their alloys have been performed by using first principles planewave pseudopotential GGA-PBE method. Sufficient tests were conducted on the convergence of k-points, kinetic energy cut-off and smearing to ensure accurate DFT results. The equilibrium lattice constants are determined for the pure metals Pt, Cr and Ru, and they are in good agreement with experiments. We have calculated the lattice constants, heats of formation and magnetic moments of Pt-Cr and Ru-Cr binary alloys. The lattice constants and magnetic moments compare well with theoretical and experimental values.

We studied 27 structures consisting of 3 pure metals: Pt, Cr, Ru and 24 binary alloys of Pt-Cr and Ru-Cr. The phase stability study of PtCr and RuCr binary alloys was based on the heats of formation, DOS, phonon spectra and phonon DOS. Five different phases of Pt_3Cr were studied, namely

$L1_2$, A15, DO_C, DO'_C and tP16. The heats of formation of all studied Pt_3Cr phases except the A15 were almost of the same magnitude, but $L1_2$ was predicted as the more stable structure.

The magnetic moment of $L1_2$ Pt_3Cr was studied and computed as 2.619 μ, which compares well with the previous theoretical (ASW and LMTO) and experimental work. Pt_3Cr $L1_2$ was characterized as ferromagnetic where a major part of magnetization density is around Cr with a much smaller magnetization around Pt.

We have calculated elastic constants of all the studied phases of Pt_3Cr. The elastic constant C_{44} of all such systems is smaller than C_{11} and C_{12}. The bulk, shear and Young's moduli were calculated using the Voigt-Reuss-Hill approximation. The ratio of shear to bulk modulus (G/B) has been used to predict the ductile/brittle behaviour of materials. Most of the studied phases, including the stable Pt_3Cr $L1_2$ are ductile. The Cauchy pressure remained positive for all studied systems, a strong indication of atomic bonding in the systems. The bulk, shear, Young's moduli and elastic constant C_{44} of Pt_3Cr $L1_2$ phase are significantly higher than those of A15 phase. $L1_2$ Pt_3Cr is hard as compared to the A15 phase.

The DOS of the pure metals, Pt, Cr, Ru and associated alloys were calculated. In all DOS diagrams, no clear energy gap separates the valence and conduction band, thus all the studied systems in this work are metallic. The partial DOS of all Pt, Cr and Ru in both pure metals and alloys indicated the d-states dominating the s and p states in both the valence and conduction bands. The contribution of the s and p states is almost the same. The high

peaks of the metallic Pt, Ru and Cr are located at $\approx$ 0 eV, 2.0 eV and 2.2 eV respectively.

In the Pt_3Cr $L1_2$ structure, the main peaks of Cr and Pt were located at about 1 eV and 3.5 eV. The stability is associated with low DOS at the Fermi level (E_f). The energy difference between the main peaks of the valence and conduction band was considered, and also the energy difference between the main peak of the valence and the Fermi level which indicated the stability of the system. There is a narrowing of energy difference between the valence and conduction band as we move from the pure metal to alloys, i.e. the reported energy differences for Pt, Cr and Pt_3Cr $L1_2$ structures are 5.5 eV, 4.0 eV and 3.55 eV respectively.

The 5d Pt high valence peak in Pt_3Cr $L1_2$ is shifted away from the E_f by as much as 3.55 eV as compared with 5d peak in pure Pt. We observed the unequal spin-up and spin-down DOS which highlighed the magnetism of the structures, where Pt_3Cr was predicted as ferromagnetic. The large total DOS in Pt_3Cr $L1_2$ near the E_f lead to spin polarization and formation of magnetic moment which in turn is a stabilizing factor. Pt_3Cr $L1_2$ was found to be energetically more favoured because the DOS at the Fermi level is relatively small as compared to other structures. A larger energy stabilization due to spin polarization relates to the large DOS at the E_f and with a larger localized magnetic moment on the Cr atom.

The stability of different phases of Pt_3Cr was further investigated using the phonon dispersion relations and phonon density of states. This analysis assures us that the soft modes at the high symmetry points lead to the unsta-

ble structures.. The calculated phonon dispersion relations, which contain soft modes and correspond to the unstable phases, have as a rule slightly higher maximal optic phonon frequencies.

We have investigated the phonon stability at 0 GPa for five different phases of Pt_3Cr using the PHONON code within VASP. The acoustic and optical modes were clearly represented. The frequency and the Brilloun zone are clearly described. There are no soft modes detected in Pt_3Cr ($L1_2$, DO_C,DO'_C and tP16). In the calculation of A15 Pt_3Cr we have noted soft modes at X, G, M and R points of the Brillouin zone. The A15 phase is dynamically unstable. Phonon study predicted the Pt_3Cr $L1_2$ as the most vibrationally stable structure compared to other studied phases.

We presented the phonon DOS where we observed the atoms vibrating in modes of different frequencies. The vibrations in DOS of Pt_3Cr $L1_2$ are mainly due to Pt atoms. Negative frequencies appear in PDOS of Pt atoms in Pt_3Cr A15 phase, which indicates the dynamic instability of the system. We then conclude that the soft modes in phonon spectra of A15 Pt_3Cr are attributed to Pt atoms. All performed calculations for heats of formation, DOS, elastic constants, phonon spectra and phonon DOS depict Pt_3Cr $L1_2$ as the most thermodynamically and dynamically stable phase; these results show an excellent level of agreement between on such stability.

Similar studies were conducted on $PtCr_3$ phases; and the heats of formation of all such studied phases were positive except the A15 phase which is stable and the latter's existence has been observed experimentally [19]. We observed that C_{44} was always smaller that the other elastic constants for all

the studied phases of $PtCr_3$. The total DOS in $PtCr_3$ A15 phase indicated more contribution of Cr than Pt atoms, the energy difference between the main peak of valence band and conduction band was about 3.8 eV, which is 2.4 eV less than the value of about 6.2 eV for $PtCr_3$ $L1_2$ phase. $PtCr_3$ A15 phase was predicted as the stable structure.

The magnitude of PDOS of Pt and its shape near the Fermi-level are strikingly different for the $L1_2$ phase of Pt_3Cr and $PtCr_3$. The Pt 5d band in $L1_2$ $PtCr_3$ is narrower than in Pt_3Cr. The phonon spectra and phonon DOS of $PtCr_3$ phases predicted A15 as dynamically stable structure, whereas $L1_2$, DO_C, DO'_C and tP16 are dynamically unstable.

We further performed studies on two phases of PtCr, $L1_0$ and B2 where the heats of formation predicted PtCr $L1_0$ as the most stable structure. The elastic properties of PtCr were also investigated. From the bulk moduli we noted that the strength of PtCr $L1_0$ is greater than that of B2 phase. The shear modulus shows that $L1_0$ is harder than B2. All positive values of the elastic constants and moduli show that the $L1_0$ phase of PtCr is elastically more stable than the B2 phase which has the negative shear modulus of -210.47 GPa.

The DOS stability of PtCr B2 and $L1_0$ structure was compared by considering the energy difference between the Fermi-level and the main peak of the d-states in the valence band, which were found to be 1.0 eV and 5.6 eV for B2 and $L1_0$ respectively. Hence PtCr $L1_0$ structure is more stable than B2. The magnitude of the DOS at Fermi-level is indicative of the stability of the calculated structure.

The soft modes were detected at G and M points of the Brillouin zone in PtCr B2 phase. The results of PtCr $L1_0$ show that motions within acoustic dispersion curves are almost entirely due to the Cr atoms. A strong softening appeared in the lower transverse acoustic branch of the PtCr $L1_0$ phase. PtCr B2 and $L1_0$ were found to be dynamically unstable, the difference is that the soft mode frequencies of $L1_0$ phase are higher than those of the B2 phase.

We studied the phonon DOS of PtCr B2 and $L1_0$ phase 0 GPa. The total DOS in PtCr $L1_o$ phase indicate that vibrations below 4 THz are due to Pt atoms, and the vibrations above 4 THz are mainly due to Cr atoms. The partial DOS of Pt and Cr in PtCr B2 phase indicate that Pt vibrates at lower frequencies while Cr vibrates at higher frequencies.

The stabilities of five different phases of $RuCr_3$ and Ru_3Cr were also investigated. We also perfomed studies on RuCr $L1_0$ and B2 phases. The heats of formation predicted all the studied Ru-Cr binary alloys as unstable, although their values are closer to zero. The effect of pressure and doping was investigated on $RuCr_3$ A15 structure where there is an evidence of its existence experimentally,. We discovered that application of both quantities increase the heats of formation and render $RuCr_3$ A15 to be more unstable. Ru-Cr system is very difficult to study.

$RuCr_3$ $L1_2$ structure behaves differently from $PtCr_3$ $L1_2$, since $RuCr_3$ has equal spin-up and spin-down DOS whereas $PtCr_3$ has unequal spin-up and spin-down DOS. The total DOS of Ru_3Cr $L1_2$ have a large dip structure at the E_f which indicates that the structure is unstable. The PDOS of Ru in Ru_3Cr $L1_2$ has a low s, p and d states in the conduction band. The PDOS

of Ru in $RuCr_3$ A15 phase indicates more d states in the conduction band than in the valence band.

In the phonon dispersion curves of $RuCr_3$ A15 phase there were no soft modes detected at any point of the Brillouin zone, indicating that $RuCr_3$ A15 phase is dynamically stable even though this system had marginally positive (just above zero) heats of formation. These findings raised an interesing research question about the stability of $RuCr_3$ A15 phase. We have calculated the total and partial phonon DOS for $RuCr_3$ A15 phase and the curves indicated that motions within acoustic dispersion curves were almost due to Ru. The motion within optical dispersion curves are vibrations due to both Ru and Cr. The existence of a stable $RuCr_3$ A15 phase has been observed experimentally [37], and this is confirmed by our calculations.

Studies on pure Cr, at first Cr was predicted to be non-magnetic. The computed lattice constant is in good agreement with previous theoretical studies. This finding was changed in our spin polarized calculations with the GGA-PBE, where Cr was reported as anti-ferromagnetic, there is an excellent agreement between our theoretical studies and experiments. The heats of formation predicted AF as the most stable structure than NM. The magnetic moment of 1.07 μB was obtained for AF, which is in good agreement with FLAPW calculations.

Lastly we studied the thermal expansion of Pt_3Cr $L1_2$ and A15 phases in the temperature range of 0 - 500 K. From the plot of the dependence of free energy on the lattice constants, it is observed that a minimum of each curve shifts to larger lattice constants in Pt_3Cr $L1_2$ phase as we increase the

temperature, whereas in the A15 phase the minimum shifts to lower lattice constants.

In summary, we have demonstated, from computational modelling studies, the stability of Pt-Cr and Ru-Cr alloys. The stability was firstly investigated based on the heats of formation and the results predicted Pt_3Cr $L1_2$, $PtCr_3$ A15 and PtCr $L1_0$ as the most stable structures. These results were further confirmed by electronic DOS. Additional investigation on stability based on phonon DOS and phonon spectra also reveals Pt_3Cr $L1_2$, $PtCr_3$ A15 and PtCr $L1_0$ as stable structures. In conclusion, it is recommended that such predicted stable structures be considered for high temperature applications in aggresive environments. Intensive stability study must be conducted on $RuCr_3$ A15 phase which was predicted as dynamically stable but thermodynamically unstable.

6.2 Recommendations

We suggest that new ab-initio calculations be conducted especially on metal alloys formed by preferably other transition metals in order to find materials that are stronger and corrosion resistant for the use in gas turbine industries. Since all the studied Ru-Cr systems are thermodynamically unstable it is recommended that further calculations be done beyond room temperature i.e at higher temperatures as these would be useful in clarifying the issue of stability in Ru-Cr systems. Finding a dopant that can tune or improve the stability of $RuCr_3$ is a challenging task, the useful direction for future work is to search and identify the possible dopants, i.e. a number of metals that could

be considered to reduce the heats of formation of $RuCr_3$ A15 phase. It is also recommended that further calculations on Ru-Cr systems be performed using the anti-ferromagnetic Cr to investigate the effect of magnetic moment on the heats of formation.

Bibliography

[1] B.M. Warnes and D.C. Punola, Surf. Coat. Technol., **95**, 1 (1997).

[2] A.H. Sully, Metallurgy of the Rarer Metals-1. Chromium 1^{st} ed, Butterworths Scientific Publications, London, (1954).

[3] C.T. Sims, J. Met., **15**, 127 (1963).

[4] W.D. Klopp, J. Met., **21**, 23 (1969).

[5] G.B. Fairbank, C. Humpreys , A. Kelly and C.N. Jones, Intermetallics, **8**, 1091 (2000).

[6] P.J. Hill, Y. Yamabe-Mitari and I.M. Wolff, Scripta Mater., **44**, 43 (2001).

[7] P.J. Hill, L.A. Cornish, P. Ellis and M.J. Witcomb, J. of Alloys and Compounds, **322**, 166 (2001).

[8] T. Tohyama, Y. Ohta and M. Shimuzi, J. Phys. Condens. Matter, **1**, 1789 (1989).

[9] A. K. Sinha, Trans. AIME, **245**, 911 (1969).

[10] W. Lin, J-h. Xu and A.J. Freeman, Phys. Rev. B, **45**, 10863 (1992).

[11] K.M. Jackson, M.P. Nzula, S. Nxumalo and C.I. Lang, Mater. Res. Soc. Symp. Proc; 842 Warrendale PA (2005).

[12] R.M. Roshko and W. Gwyn, Phys. Rev. B, **9**, 4945 (1974).

[13] F.R. De Boer, R. Boom and A.R. Meidema, Physica, **113B**, 18 (1982).

[14] J.G. Booth, Phys. Status Solidi, **7**, K157 (1964).

[15] M. Venkatraman and J.P. Neumann, Bull Alloy Phase Diagram, **11**, 16 (1990).

[16] T.B. Massalski (Ed.-in-chief), Binary Alloy Phase Diagrams, 2^{nd} edition, Ohio, USA, Amer. Soc. Metals (1990).

[17] L. Muller, Ann. Phys. (Leipzig), **7**, 9 (1930).

[18] R.M. Waterstrat, Metall. Trans., **4**, 1585 (1973).

[19] K. Oikawa, G.W. Qin, T. Ikeshoja, O. Kitakami, Y. Shimada, K. Ishida and J. Fukamichi, J. Magn. and Magn. Mat., **236**, 220 (2001).

[20] E. Raub and W. Mahler., Z. Metallkd., **46**, 210 (1955).

[21] E. Friedrich and A. Kussman, Phys. Z., **36**, 185 (1935).

[22] E. Gebhardt and Koster, Z. Metallkd., **32**, 262 (1940).

[23] S.J. Pickart and R. Nathans, J. Appl. Phys., **34**, 1203 (1963).

[24] M.J. Besnus and A.J.P. Meyer, Phys. Status Solidi (b), **58**, 533 (1973).

[25] T. Goto, J. Phys. Soc. Jpn., **43**, 1848 (1977).

[26] J. Baglin, F. d'Heurle, W. Hammer and S. Zirinsky, 7^{th} Int. Vacuum Congress and 3^{rd}Int. Conf. Solid Surfaces, **3**, 2127 (1977).

[27] J. Baglin, J. Dempsey, F. d Heurle, W. Hammer and S. Zirinsky, Proc. Electrochem. Soc., **78-2**, 185 (1978).

[28] J. Baglin, F. d Heurle, W. Hammer and S. Zirinsky, Proc. Electrochem. Soc., **125**, 1854 (1978).

[29] A.K. Butylenko and V.V. Nevdacha, Dop. Akad. Nauk. Ukr. RSR A., Fiz.-Mat.Tekh., **42**, 66 (1980).

[30] A. Kussman, K. Muller and E. Raub, Z. Metallkd, **59**, 859 (1968).

[31] A. Oles and A. Bombik, Phys. Status Solidi(b), **92**, K81 (1979).

[32] H.J. Nagasawa., Phys. Soc. Jpn., **28**, 1171 (1970).

[33] W.M. Star, E. De Vroede and C. Van Baarle, Physica, **59**, 128 (1972).

[34] E.M. Savitskii, V.F. Terekhova, and N.A. Birun, Russ. J. Inorg. Chem., **6**, 1002 (1962).

[35] F. A. Shunk: Constitution of Binary Alloys, 2nd ed., McGraw-Hill, New York, NY, 278 (1969).

[36] R.M. Waterstart, J. Less-Common Met., **80**, 33 (1981).

[37] Y. F. Gu, H. Harada, Y. Ro and T. Kobayashi, Met. and Mat. Trans., **36A**, 578 (2005).

[38] T.B. Massalski: Binary Alloy Phase Diagrams, 2nd ed., ASM, Materials Park, OH, 27 (1992).

[39] P.J. Hill, L.A. Cornish, P. Ellis and M.J. Witcomb, J. Alloys and Compounds **322**, 166 (2001).

[40] L.A. Cornish, R. Süss, A. Watson and S.N. Prins, Platinum Metals Rev., **51**, 104 (2007).

[41] A. Watson, R. Süss and L.A. Cornish, Platinum Metals Rev., **51**, 189 (2007).

[42] I.M. Wolff and P.J. Hill, Platinum Metals Rev., **44**, 158 (2000).

[43] L.A. Cornish, R. Süss, A. Watson and S.N. Prins, 'Building a Database for the Prediction of Phases in Pt-based Superalloys', in "Second International Platinum Conference 'Platinum Surges Ahead" , Sun City, South Africa, 8th - 12th October , 2006, Symposium series S45, The Southern African Institute of Mining and Metarllurgy, Johannesburg, South Africa, (2006), pp. 91 - 102.

[44] J. Preusnner, M. Wenderoth, S.N. Prins, R. Völkl and U. Glatzel, 'Platinum Alloy Development - the Pt-Al-Cr-Ni system', in "Second International Platinum Conference 'Platinum Surges Ahead", Sun City, South Africa, 8th - 12th October, 2006, Symposium Series S45, The

Southern African Institute of Mining and Metarllurgy, Johannesburg, South Africa, 2006, pp. 103-106.

[45] CASTEP Users Guide, San Diego: Accelrys Inc., 2001.

[46] G. Kresse and J. Furthmuller, Phys. Rev. B, **54**, 11 169 (1996).

[47] D. Vanderbilt, Phys. Rev. B, **41**, R7892 (1990).

[48] P.E. Blochl, Phys. Rev. B, **50**, 17953 (1994).

[49] P.Hohenberg and W.Kohn, Phys. Rev, **136**, B864 (1964).

[50] W. Kohn and L.J. Sham, Phys. Rev., **140**, A1133 (1965).

[51] J. Harris and R.O. Jones, J. Phys., **F4**, 1170 (1974).

[52] O. Gunnarsson and B.I. Lindqvist, Phys. Rev. B, **3**, 4174 (1976).

[53] D.C. Langreth and J.P. Perdew, Phys. Rev. B, **15**, 2884 (1977).

[54] B.W. Dadson, Phys. Rev., **35**, 880 (1987).

[55] K.-M. Ho and K.P. Bohnen, Phys. Rev. Lett., **59**, 1833 (1987).

[56] E. Wimmer, Nato series: Electronic structure methods, Biosym/Molecular Simulation.

[57] P. Fulde, Electron Correlations in Molecules and Solids, Springer (1995).

[58] A. D. Becke, Phys. Rev. A, **38**, 3098 (1998).

[59] E. Wimmer, Prediction of Materials Properties (1998).

[60] J. P. Perdew and Wang Yue, Phys. Rev. B, **33**, 8800 (1986).

[61] T.C. Leung, T.C. Chan and B.N. Harmon, Phys. Rev. B, **44**, 2923 (1991).

[62] T. Asada and K. Terakura., Phys. Rev. B, **47**, 15992 (1993).

[63] M. Eder, E.G. Moroni and J. Hafner, Surf. Sci. Lett., **243**, 244 (1999).

[64] M. Eder, E.G. Moroni and J. Hafner, Phys. Rev. B. in press.

[65] J.C. Phillips, Phys. Rev., **112**, 685 (1958).

[66] M.L. Cohen and V. Heine, Solid State Physics, **24**, 37 (1970).

[67] M.T. Yin and M.L. Cohen, Phys. Rev. B, **25**, 7403 (1982a).

[68] M. C. Payne, M.P. Teter and D.C. Allan, T.A. Arias and J.D. Joannopoulos, Rev. Mod. Phys., **64**, 1045 (1992).

[69] L. Kleinmann and D.M. Bylander, Phy. Rev. Lett., **48**, 1425 (1982).

[70] D. Vanderbilt, Phys. Rev. B, **41**, 7892 (1990).

[71] V. Milman, B. Winkler, J.A. White, C.J. Pickard, M.C. Payne, E.V. Akhmatskaya and R.H. Nobes, Int. J. Quant. Chem., **77**, 895 (2000).

[72] M.D. Segall, P.L.D. Lindan, M.J. Probert, C.J. Pickard, P.J. Hasnip, S.J. Clark and M.C. Payne, J. Phys. Cond. Matt., **14**, 2717 (2002).

[73] A.E. Mattsson, P.A. Schultz, M.P. Desjarlais, T.R. Mattsson and K. Leung, Modelling Simul. Mater. Sci. Eng., **13**, R1 (2005).

[74] H.J. Monkhorst and J.D. Park, Phys. Rev. B, **13**, 5188 (1976).

[75] D.J. Chadi and M.L. Cohen, Phys. Rev. B, **8**, 5747 (1973).

[76] J.D. Joannopoulos and M.L. Cohen, J. Phys. C, **6**, 1572 (1973).

[77] M. Methfessel and A.T. Paxton, Phys. Rev. B, **40**, 3616 (1989).

[78] R.P. Feynman, Phys. Rev., **56**, 340 (1939).

[79] G. Kresse and J. Hafner, J. Phys.: Condens. Matter, **6**, 8245 (1994).

[80] CASTEP Users Guide (Molecular Simulations Inc.) San Diego, CA (1998).

[81] P. Villars and L.D. Calvin, Pearson's Handbook of Crystallographic Data for Intermetallic Phases, 1985, 1-3.

[82] S. Hong and C.L. Fu, Intermetalics, **7**, 6 (1999).

[83] M.J. Mehl and D.A. Papaconstantopoulos, Phys. Rev. B, **54**, 4523 (1996).

[84] Y. Kwon, T.H. Rho, S. Lee and S.C. Hong, J. Appl. Phys., **93**, 7152 (2003).

[85] H.R. Chauke, University of Limpopo, Thesis (2005).

[86] Z.W. Lu, B.M. Klein and H.T. Chau, Phys. Rev. B, **58**, 9255 (1998).

[87] A. Szajek, Acta Phys. Pol. A **82**, 967 (1992).

[88] P.M. Oppeneer, V.N. Antonov, T. Kraft, H. Eschrig, A.N. Yaresko and A. Ya Perlov, J. Phys.: Condens. Matter, **8**, 5769 (1996).

[89] D.E.G. Williams and A. Jezierski, J. Magn. Magn. Mater., **59**, 41 (1986).

[90] S.K. Burke, B.D. Rainford, D.E.G. Williams, P.J. Brown and D.A. Hukin, J. Magn. Magn. Mater., **15**, 505 (1980).

[91] S.J. Pickart and R. Nathans, J. Appl. Phys., **34**, 1203 (1963).

[92] R.B. Patel, A.J. Liddiard and M.D. Crapper, J. Phys.: Condens. Matter, **6**, 9973 (1994).

[93] Maruyama et al, J. Magn. Magn. Mater., **140**, 43 (1995).

[94] M. Shirai, H. Maeshima and N. Suzuki, J. Magn. Magn. Mater., **140**, 105 (1995).

[95] Z.W. Lu, B.M. Klein and A. Zunger, Phys. Rev. Lett., **75**, 1320 (1995).

[96] L. Louail, D. Maouche, A. Roumili and F. Ali Sahraoui, Material. Lett., **58**, 2975 (2004).

[97] R. Hill, Proc. Phys. Soc. Lond., **65**, 349 (1952).

[98] S. F. Pugh, Philos. Mag., **45**, 823 (1954).

[99] D. G. Pettifor, Mater. Sci. Technol., **8**, 345 (1992).

[100] D. G. Clerc and H. M. Ledbetter, J. Phys. Chem. Solids, **59**, 1071 (1998).

[101] D.F. Johnson, D.E. Jiand and E.A. Carter, Surf. Sci., **601**, 700 (2007).

[102] J.P. Perdew, K. Burke, M. Ernzerhof, Phys. Rev. Lett., **77**, 3865 (1996).

[103] R. Hafner, D. Spisak, R. Lorenz and J. Hafner, Phys. Rev. B, **65**, 184432 (2002).

[104] V.L. Moruzzi and P.M. Marcus, Phys. Rev. B, **42**, 8361 (1990).

[105] S. Cottenier, B. De Vries, J. Meersschaut and M. Rots, J. Phys.: Condens. Matter, **14**, 3275 (2002).

[106] D. Singh and J. Ashkenaz, Phys. Rev. B, **42**, 11570 (1992).

[107] J. Kubler, Theory of Itinerant Magnetism (Oxford University Press, Oxford), 212 (2000).

[108] K Parlinski, Z.Q. Li and Y. Kawazoe, Phys. Rev. Lett., **78**, 4063 (1997).

[109] K. Parlinski, *Neutrons and numerical methods N_2M* , edited by M.R. Johnson, G.J. Kearley, H.G. Bi*ü*ttner, Am. Inst. Phys. Conf. Proc. **479**, 121 (1999).

[110] K. Parlinski, software PHONON (1999).

[111] A Schauer, *Can. J. Phys.*, **42**, 1857 (1964).

[112] A Schauer, *Can. J. Phys.*, **43**, 523 (1965).

[113] A. A. Quong and A. Y. Liu, Phys. Rev. B, **56**, 7767 (1997).